Solid-state NMR as a tool for investigating paramagnetic Ni containing heterogeneous catalysts

Dissertation
zur Erlangung des akademischen Grades
doctor rerum naturalium (Dr. rer. nat.)
der Mathematisch-Naturwissenschaftlichen Fakultät
der Universität Rostock

vorgelegt von
Mirjam Schröder
geboren in München
Rostock, 2025

https://doi.org/10.18453/rosdok_id00005455

Die vorliegende Arbeit wurde im Zeitraum von Juli 2021 bis Dezember 2024 an der Universität Rostock unter der Betreuung von Prof. Dr.-Ing. Björn Corzilius und am Leibniz-Institut für Katalyse e.V. unter der Betreuung von Prof. Dr. Angelika Brückner angefertigt.

EXAMINERS:
Prof. Dr.-Ing. Björn Corzilius, University of Rostock
Prof. Dr. Angelika Brückner, Leibniz Institute for Catalysis, Rostock
Dr. Luís Mafra, CICECO – Aveiro Institute of Materials, Aveiro, Portugal

DATE OF SUBMISSION January 17, 2025
DATE OF DEFENSE July 1st, 2025

Success is not the key to happiness.
Happiness is the key to success.
If you love what you are doing,
you will be successful.

— Albert Schweitzer

To my family

ABSTRACT

Dimerization of butenes is a well-known and widely used process to valorize C_4 raffinate to C_8 hydrocarbons, which are blended into gasoline fuels or used as intermediates for plasticizer production. Ni-impregnated amorphous silica alumina (ASA) materials – metal-doped derivatives of Mobil Composition of Matter No. 41 (MCM-41) – serve as heterogeneous catalysts for this reaction since they contain necessary Brønsted acid sites (BASs) of different strengths. The selectivity of this reaction towards linear products correlates with the surface acid sites and is crucial for its industrial application. BASs have two primary functions, stabilization of Ni single sites [1] and activation of butenes. cannot correlate acid sites with their respective strengths.

To this end, solid-state NMR (ssNMR) was applied to Ga and Al doped MCM-41. By using the probe molecule trimethylphosphine oxide (TMPO), we demonstrate strong BASs to be present, and their presence to correlate with high reaction selectivity. These sites are essential for Ni active site formation.

In detail, ^{31}P ssNMR was performed on TMPO-impregnated support materials. Ga doping results in stronger BAS as compared to Al doping. Furthermore, a strong Lewis acid site (LAS) and a second, weaker BAS are also identified in all supports. $(TMPO)_2H^+$ dimer formation could be ruled out by using both solvent-based and solvent-free impregnation methods. This is in stark contrast to zeolites, where dimer formation hampers unequivocal spectral assignment of acid sites. The lower amount of acid sites in Ga-MCM-41 reduces the contribution of the carbenium-ion mechanism during catalysis, while the increased BAS strength potentially enhances the Lewis acid strength of the adsorbed Ni, thus enhancing attachment of butenes prior to the reaction.

In conclusion, this research offers novel insights into the role of acid sites in butene dimerization, highlighting the importance of strong BASs for selectivity in this industrially significant process. Additionally, in mesoporous materials in contrast to zeolites, a simple TMPO impregnation method allows for a more straight-forward characterization of acid sites in these materials using ssNMR.

ZUSAMMENFASSUNG

Die Buten-Dimerisierung ist ein weitverbreitetes Verfahren zur Aufwertung von C_4-Raffinat zu C_8-Kohlenwasserstoffen, die Kraftstoffen beigemischt oder für die Weichmacherherstellung verwendet werden. Ni-imprägnierte amorphe Silika-Alumina-Materialien (ASA) – metalldotierte Derivate von MCM-41 (Mobil Composition of Matter No. 41) – dienen hier als heterogene Katalysatoren, da sie die notwendigen Brønstedsäurezentren (BAS) in unterschiedlichen Stärken enthalten. Die Selektivität dieser Reaktion für lineare Produkte hängt mit den Oberflächen-Säurezentren zusammen und ist entscheidend für ihre industrielle Anwendung. BAS haben zwei Hauptaufgaben: Die Stabilisierung der einzelnen Ni-Zentren und die Aktivierung von Butenen. Jedoch ist wenig über die Rolle von Lewissäurezentren (LAS) und die optimale Stärke und Konzentration beider Arten von Säurezentren bekannt. Auch der Einfluss von Säurezentren in direkter Nachbarschaft von Ni auf den Reaktionsmechanismus ist unbekannt. Bisher eingesetzte Charakterisierungstechniken können den Typ eines Säurezentrums nicht mit seiner Stärke korrelieren. Deshalb wurde Festkörper-Kernmagnetresonanz (ssNMR) verwendet und Ga- und Al-dotierte MCM-41 Materialien untersucht. Mit der Verwendung des Sondenmoleküls TMPO konnte die Anwesenheit von starken BASs gezeigt werden, womit eine hohe Selektivität korreliert. Diese Zentren sind besonders wichtig für die Bildung der aktiven Ni-Zentren.

Konkret wurde der ^{31}P Kern des Sondenmoleküls auf TMPO-imprägnierten Trägermaterialien mittels ssNMR beobachtet. Die Modifikation mit Ga-Atomen führt zu stärkeren BAS im Vergleich zur Modifikation mit Al. Darüber hinaus wurden in allen Trägermaterialien ein starkes LAS und ein zweites, schwächeres BAS identifiziert. Die Bildung von $(TMPO)_2H^+$-Dimeren konnte sowohl bei der Verwendung von lösungsmittelbasierten als auch lösungsmittelfreien Imprägnierungsmethoden ausgeschlossen werden. Dies steht in starkem Gegensatz zu Zeolithen, bei denen die Dimerbildung eine eindeutige spektrale Zuordnung der Säurezentren erschwert. Die geringere Menge an sauren Zentren in Ga-MCM-41 verringert den Anteil des Carbenium-Ionen-Mechanismus in der Katalyse, während die erhöhte BAS-Stärke potenziell die Lewis-Säurestärke des adsorbierten Ni erhöht und damit die Bindung von Butenen vor der Reaktion verbessert.

Zusammengenommen liefert diese Arbeit neue Einblicke in die Rolle der sauren Zentren bei der Dimerisierung von Buten und hebt die Bedeutung einer hohen BAS-Stärke für die Selektivität in diesem industriell bedeutsamen Prozess hervor. Im Gegensatz zu Zeolithen ermöglicht ein einfaches TMPO-Imprägnierungsverfahren bei mesoporösen Materialien eine direktere Charakterisierung der Säurezentren mittels ssNMR.

PUBLICATIONS

Peer-reviewed publications

During the work on this PhD thesis, the following publications were published beyond the scope of this thesis.

[1] **M. Schröder**, T. Biskup, cwepr – A Python package for analysing cw-EPR data focussing on reproducibility and simple usage. *Journal of Magnetic Resonance* **2022**, *335*, 107140.

[2] S. Li, **M. Schröder**, A. Prudlik, X. Shi, A. Spannenberg, J.Rabeah, R. Francke, B. Corzilius, F. Reiß, T. Beweries. A General Concept for the Electronic and Steric Modification of 1-Metallacyclobuta-2,3-dienes: A Case Study of Group 4 Metallocene Complexes. *Chemistry – A European Journal* **2024**, *30*, e202400708.

[3] S. Li, **M. Schröder**, X. Shi, A. Spannenberg, J. Fischer, B. Corzilius, F. Reiß, T. Beweries. Reactions of Titanium- and Zirconium-Based 1-Metallacyclobuta-2,3-diene Complexes with Diazenes: N=N Bond Cleavage versus N−C Bond Formation and Dearomatization. *Organometallics* **2024**, *43*, 3153.

[4] H. Beer, J.-E. Siewert, **M. Schröder**, M. Fischer, B. Corzilius, C. Hering-Junghans Phosphaarsenes – Combining Phospha- and Arsa-Wittig-Reagents. *ChemPlusChem* **2024**, *89*, e202400120.

[5] T. Biedenbänder, A. Rodgers, **M. Schröder**, L. Vugmeyster, B. Corzilius, Investigation of biomolecular dynamics by sensitivity-enhanced $^{1}H-^{2}H$ CPMAS NMR using matrix-free dynamic nuclear polarization. *Journal of Magnetic Resonance Open* **2024**, *21*, 100161.

[6] T. Otroshchenko, A. Fedorov, Q. Zhang, D. Linke, J. Handzlik, **M. Schröder**, B. Corzilius, E. V. Kondratenko, Time-resolved and theoretical analysis of Mo-carbenes transformations in metathesis of ethylene with 2-butene. *Chemical Science* **2025**, *16*, 3141.

[7] M. J. Ernst, A. Petrov, **M. Schröder**, B. Corzilius, C. Müller, *Cyclo*-P_5^- Revisited: The Surprisingly Stable Uncoordinated Pentaphospholide Anion. *Angewandte Chemie International Edition* **2025**, *64*, e202505853.

Software Publications

[1] **M. Schröder**, NMRAspecds, *Zenodo*, **2024**. DOI: 10.5281/zenodo.13293054

[2] **M. Schröder**, T. Biskup, LabInform ELN: A lightweight and flexible electronic laboratory notebook for academic research based on the open-source software DokuWiki. *ChemRxiv*, **2023** DOI: 10.26434/chemrxiv-2023-2tvct

Conference talks and contributions

[1] **M. Schröder**: NMR methods for catalyst structure determination – A multinuclear approach, *Seminar on Physical Chemistry, University of Rostock*, Rostock, Germany, **06/2022** (Talk)

[2] **M. Schröder**, T. H. Vuong, J. Rabeah, A. Brückner, B. Corzilius, Characterization of Acid Sites on Supported Ni Catalysts, *Euromar Conference*, Utrecht, Netherlands, **07/2022** (Poster)

[3] **M. Schröder**, T. H. Vuong, J. Rabeah, A. Brückner, B. Corzilius, Developing Methods for the Acidity Measurements on Supported Ni Catalysts, *61th Annual Rocky Mountain Conference on Magnetic Resonance*, Copper Mountain, Colorado, USA, **08/2022** (Poster)

[4] **M. Schröder**, Developing NMR Methods for the Acidity Measurements on Supported Ni Catalysts, *LLM-Workshop*, University of Rostock, Germany, **08/2022** (Poster)

[5] **M. Schröder**, T. H. Vuong, J. Rabeah, B. Corzilius, A. Brückner, Developing NMR Methods for the Acidity Measurements on Supported Ni Catalysts, *43th FGMR Annual Discussion Meeting*, Karlsruhe, Germany, **09/2022** (Poster)

[6] **M. Schröder**, T. H. Vuong, J. Rabeah, B. Corzilius, A. Brückner, Structure and function of single-site catalysts – A multinuclear approach, *LLM Graduate Workshop*, Rostock, Germany, **01/2023** (Talk)

[7] **M. Schröder**: The Role of Mesoporous Materials in Modern Catalysis, *Seminar and Workshop "Perspectives of Physical and Theoretical Chemistry"*, Bad Malente, Germany, **02/2023** (Talk)

[8] **M. Schröder**, T. H. Vuong, J. Rabeah, J. Knossalla, R. Franke, B. Corzilius, A. Brückner, How solid state NMR can unravel the role of acid site strength in supported Ni catalysts, *56. Jahrestreffen Deutscher Katalytiker*, Weimar, Germany, **03/2023** (Poster)

[9] **M. Schröder**, T. H. Vuong, J. Rabeah, A. Brückner, B. Corzilius, Whispers of Catalysis: A Spectroscopic Journey into Supported Ni/SiAl catalysts, *Mini Symposium*, Würzburg, Germany, **09/2023** (Talk)

[10] **M. Schröder**, T. H. Vuong, J. Rabeah, A. Brückner, B. Corzilius, Solid state NMR and FTIR spectroscopy for analyzing acidic sites in supported Ni/SiAl catalysts by probe molecules, *Alpine Conference on Magnetic Resonance in Solids*, Chamonix-Mont-Blanc, France, **09/2023** (Roundtable Discussion)

[11] **M. Schröder**, T. H. Vuong, J. Rabeah, A. Brückner, B. Corzilius, Chasing the Single Nickel Site on Silica-Alumina Catalysts, *Seminar and Workshop "Perspectives of Physical and Theoretical Chemistry"*, Bad Malente, Germany, **03/2024** (Talk)

[12] **M. Schröder**, T. H. Vuong, J. Rabeah, B. Corzilius, A. Brückner, Chasing the Single Nickel Site on Silica-Alumina Catalysts, *AK-Treffen*, Bad Kissingen, Germany, **03/2024** (Talk)

[13] **M. Schröder**, T. H. Vuong, J. Rabeah, A. Brückner, B. Corzilius, Solid-State NMR as a Toolbox Towards a Full Mechanistic Understanding of Catalytic Butene Dimerization, *Euromar Conference*, Bilbao, Spain, **06/2024** (Poster)

[14] **M. Schröder**, T. H. Vuong, J. Rabeah, B. Corzilius, A. Brückner, Probing the Surface Sites of a Mesoporous Dimerization Catalyst with ssNMR and FTIR, *Uni@Leibniz Workshop*, Rostock, Germany, **07/2024** (Talk)

[15] **M. Schröder**, T. H. Vuong, I. Marin-Montesinos J. Rabeah, L. Mafra, B. Corzilius, A. Brückner, Solid-State NMR as a Toolbox Towards a Full Mechanistic Understanding of Catalytic Butene Dimerization, *45th FGMR Annual Discussion Meeting*, Rostock, Germany, **09/2024** (Contributed Talk)

CONTENTS

LIST OF FIGURES

LIST OF TABLES

LISTINGS

ABBREVIATIONS

AIMD	*ab initio* molecular dynamics
Al	aluminium
Ar	argon
ASA	amorphous silica alumina
ATR	attenuated total reflectance
BAS	Brønsted acid site
BET	Brunauer, Emmett and Teller model to calculate the average pore size from gas physisorption measurements
BJH	Barrett, Joyner and Halenda model to calculate the overall surface area from gas physisorption measurements
BMS	bulk magnetic susceptibility
cf.	*lat.* confere, *eng.* compare
CP	cross polarization
Cp	cyclopentadiene
CPMG	Carr-Purcell-Meiboom-Gill
CSA	chemical shift anisotropy
CTAB	cetyltrimethylammonium bromide
CH_2Cl_2	dichloromethane
DNP	dynamic nuclear polarization
DQ	double quantum
DFT	density functional theory
DRIFTS	diffuse reflectance infrared Fourier transform spectroscopy
DP	direct polarization
EFAL	extra framework aluminium
EPR	electron paramagnetic resonance

EXAFS	extended X-ray absorption fine structure
e.g.	*lat.* exempli gratia, *eng.* for example
FID	free induction decay
FT	Fourier transform
FTIR	Fourier transform infrared spectroscopy
FSM-16	Folded Sheet Silica 16
Ga	gallium
GC	gas chromatography
HETCOR	heteronuclear correlation
HFI	hyperfine interaction
HMQC	heteronuclear multiple quantum correlation
i.e.	*lat.* id est, *eng.* that is
IR	infrared
LAS	Lewis acid site
MAS	magic angle spinning
MCM-41	Mobil Composition of Matter No. 41
MFI	zeolite framework type (from ZS**M**-5 (**fi**ve))
MOR	mordenite
MQMAS	multiple quantum MAS
NH_3	ammonia
NH_4^+	ammonium ion
Ni	nickel
NMR	nuclear magnetic resonance
PBS	pseudobridging silanol
PRE	paramagnetic relaxation enhancement
Pyr-IR	IR spectroscopy of adsorbed pyridine
REDOR	rotational echo double resonance
RESPDOR	resonance-echo saturation-pulse double-resonance
RF	radio frequency

rt	room temperature
SEM	scanning electron microscopy
SNR	signal-to-noise ratio
SQ	single quantum
ssNMR	solid-state NMR
TEM	transmission electron microscopy
TEPO	triethylphosphine oxide
TMP	trimethylphosphine
TMPO	trimethylphosphine oxide
TOPO	trioctylphosphine oxide
TPD	temperature-programmed desorption
TPPO	triphenylphosphine oxide
TRAPDOR	transfer of populations *via* double resonance
TMS	tetramethylsilane
T_1	spin-lattice relaxation time constant
T_2	spin-spin relaxation time constant
USY	ultra-stabilized zeolite Y
XPS	X-ray photoelectron spectroscopy
XRD	X-ray diffraction
ZQ	zero quantum
ZSM-5	Zeolite Socony Mobil-5

1 MOTIVATION AND OBJECTIVES

Dimerization of butenes is a well-known and widely used process to valorize C_4 raffinate to C_8 hydrocarbons which are blended to gasoline fuels [2] or used as intermediates for plasticizer production. Different catalysts supported on silica-alumina have historically been used with a high amount (20 wt%) of NiO in industrial processes, while a lower amount of nickel (0.6 wt%) supported on amorphous silica-alumina or zeolites as state of the art in research [3] showed similar performance as the commercial ones. The acidity of silica-alumina supports crucially affects the activity and selectivity of butene dimerization processes. Here, the less branched C_8 products *n*-octene and methylheptenes are the desired products. Nickel supported mesoporous catalysts have been used industrially for several decades. Despite detailed investigations [1, 3, 4], the mechanism of this reaction is not fully understood yet. Of particular interest are the Lewis acid sites (LASs) and Brønsted acid sites (BASs) on the surface. BASs have two functions: stabilization of Ni single sites [1] and activation of butenes [3], yet little is known about the role of LASs and the optimum strength and concentration of both types of acid sites.

A variety of studies have been applied to different catalytic systems to explain the mechanism of butene characterization, by our group [1, 3–5] and by others. [2, 6–14] In this thesis, the Mobil Composition of Matter No. 41 (MCM-41) class of support materials was investigated with solid-state NMR (ssNMR) complementing a bouquet of other methods.

To study the acidic sites, different amounts of BASs and LASs were created by introducing Ga^{3+} or Al^{3+} (in general T^{3+}) into the lattice of MCM-41 with Si/T ratios of 10 or 20 each. They are further denoted e.g. as Al-M10 for the MCM-41 derivative of Al with a Si to Al ratio of 10. IR spectroscopy of adsorbed pyridine (Pyr-IR) reveals substantial differences in the number of acid sites: while Ga-MCM-41 materials exhibit fewer BAS compared to Al-MCM-41, they contain a higher number of LASs. However, an exact mapping of a type of an acid site to its strength is not possible by Pyr-IR and NH_3-temperature-programmed desorption (TPD) that was conducted as well. During catalytic test reactions, both activity and selectivity towards the desired products, were assessed. Among the samples, Ga-M10 demonstrated peak performance, showing a maximum in both activity and an increasingly favorable selectivity.

Besides the role of the acid sites discussed above, the position of the paramagnetic Ni sites, which are the reaction centers, is of particular

importance for the reaction. Due to the strong interaction with the unpaired electrons, protons in the immediate vicinity are expected to have a strong deviation from their usual chemical shift. Methods of paramagnetic ^{1}H-NMR were applied to obtain information about the position of BASs and their immediate surroundings.

The aim and purpose of this thesis was to establish and develop ssNMR methods to investigate these intrinsic properties. First, the literature was consulted to extract methods suitable for the given materials and feasible with the available spectrometer setup. Second, methods were implemented and iteratively improved which involved encountering and addressing various challenges and errors before achieving proficiency.

In summary, this work intends to provide a deeper understanding of the interplay between acid sites and nickel species in butene dimerization catalysis by employing advanced ssNMR techniques. By refining these methods and applying them to tailored mesoporous catalysts, this study aims to explain the mechanistic roles of both BASs and LASs, in the interplay with the paramagnetic Ni centers. These insights will contribute to the optimization of catalyst design and performance for industrial applications.

This study is embedded in the generally broader context of spectroscopy in heterogeneous catalysis. A multitude of different species are present in heterogeneous catalytic reactions, some of which are decisive in the reaction but of very short lifetime. Key catalytic species also occur on the surface of the catalyst, at the interface with the reactants. As a result, the species of interest are often present in very low concentrations, which makes the analysis much more difficult. Therefore, methods are used that are well-suited for observing the surface. However, many of these methods require a vacuum environment (X-ray photoelectron spectroscopy (XPS), transmission electron microscopy (TEM), scanning electron microscopy (SEM)), making observations under reaction conditions impossible. However, the methods that work under reaction conditions (infrared (IR) spectroscopy, Mössbauer spectroscopy, extended X-ray absorption fine structure (EXAFS) and X-ray diffraction (XRD)) are not equally sensitive to surface species. [15] Many of those methods are also local methods that study a small region of the material and are therefore not necessarily representative for the whole material.

It is important for a proper and meaningful characterization to be as close as possible to the catalytically relevant conditions. At the same time, spectroscopic methods are "by no means simple, and quick and easy experiments barely exist for catalyst characterization", as Niemantsverdriet [15] describes it in the introduction of his book. Therefore, experts in catalysis research and spectroscopists need to join forces in order to obtain meaningful results.

Part I

STATE OF THE ART

2

SILICA-ALUMINA MATERIALS FOR CATALYSIS

"Boiling stones" were long known as minerals and pigments (ultramarine) and were first described as such in 1756 by the Swedish mineralogist Axel Fredrick von Cronstedt. He observed that upon heating of the mineral stilbite, water vapor emerged. Therefore, he named the material *zeolite* from Greek ζεω– to boil and λιθος– stone. [16] The water was previously absorbed within the pores of the "stone" together with ions of various types. [17] The material consists of tetrahedral primary repeating units, containing silicon and aluminium at the centers and oxygen at the corners. Those units are interconnected *via* the corners to form larger structures like channels and pores of varying size. The negative charges introduced by Al^{3+} ions are compensated by alkali and alkaline earth counterions such as K, Na or Ca. Inspired by nature, the family of synthetic zeolites contains a much larger variety of tetragonal ions as well as counterions. Tuning the pore size and channel hierarchy as well as the surface properties leads to an enormous range of possible applications. In everyday life, zeolites are present in dishwashers and laundry detergents as ion exchangers, while in petrochemical industry, zeolites alongside mesoporous materials such as MCM-41 are in widespread use for cracking and isomerization due to their acidic surface properties. However, the pores and channels of zeolites are of microporous size (up to 2 nm) [18–21] and therefore limit the applicability to smaller molecules. Attempts to synthesize zeolites with more than twelve ring members were successful, [22] however, due to poor stability and reactivity, they are not successful in application. [18] Thus, materials providing large pore sizes and a high stability were utterly needed. Mesoporous materials with pore sizes of 2 to 50 nm [19] and with the same versatility and stability have been sought since the late 1960s – around 25 years after developing synthetic zeolites [18] – and the first synthesis was filed for a patent in 1969. [23] After the publication of a mesoporous material in the early 1990s by Yanagisawa et al. [24] which was not much acknowledged, the Mobil Oil Company presented a new type of mesoporous material – the MCM family. Three material types were identified, lamellar (MCM-50), hexagonal (MCM-41) [25–28] and cubic (MCM-48) [29] mesophases. A study in 1997 examined the properties of the material of the patented synthesis from 1969 and confirmed the material to be MCM-41. [30]

The MCM-41 materials were of immediate interest to the catalysis community because they bridged the gap between the microporous zeolites and other porous materials with macropores (Ø>50 nm [31]).

The main limitation of zeolites is the diffusion limitation in the small pores which is the bottleneck of the catalytic reaction. Larger reactant molecules can easily pass through the larger pores of MCM-41, allowing for higher reaction rates. However, because mesoporous materials are less stable than zeolites at high temperatures that occur during the regeneration of cracking catalysts, they are more commonly used for oligomerization, hydroisomerization and hydrocracking at less severe reaction conditions.

2.1 GENERAL PROPERTIES OF MCM-41 TYPE MESOPOROUS MATERIALS

The hexagonal MCM-41 material features a high surface area between 700 to 1300 m^2 [26, 27, 32] and offers good stability under thermal (up to 800 to 900 °C [33]), hydrolytic, and hydrothermal conditions, although zeolites exhibit superior stability in these aspects. The pores are wide and tunable in a range between 15 and 100 Å [34, 35], which allows for the penetration of large molecules into the channels. Their size distribution and the surface area of the material can be detected by physisorption methods using N_2 or Ar as sorbants and after modeling the data with the BARRETT, JOYNER and HALENDA (BJH) [36] method or BRUNAUER, EMMETT and TELLER (BET) [37] method, respectively. [38] The pore size is dependent on the templating surfactants that form the micelles. The silica and alumina precursors were adsorbed initially on these. [39, 40] The walls around the pores have a width of 6 to 10 Å. [33] After calcination – meaning the removal of the organic template by heat – those mesoporous materials are made of SiO_4 or AlO_4 tetrahedra. These are interconnected via corner-sharing of one O-atom but do not follow a regular pattern; instead they are rather amorphous. The structure of the elongated rod-like micelles is preserved in the long range order. The pores can be observed by XRD at low angles below $\theta < 10°$ [41] while the rest of the structure cannot be characterized by XRD.

During synthesis with cetyltrimethylammonium bromide (CTAB), initial micelles with a diameter of about 2.5 nm are formed, which are the later pores. In the synthesized material, NH_4^+ ions are the counterions of the negatively charged four-coordinated Al ions. During calcination, the ammonium ions are thermally decomposed and removed, and the negative charge is then compensated by protons. Further ion exchange is possible to tune properties of the material. For industrial use, the materials are mixed with binders and then shaped or molded into larger structures providing mechanical integrity to withstand the demands of large-scale reaction conditions. [42]

2.2 ISOMORPHOUS SUBSTITUTION OF SILICON

While the first MCM-41-like materials only contained oxygen-bridged Si, the patents of MCM-41 also comprised compositions with up to four different elements in the structure. [27] Soon, there were more investigations on purposefully exchanging Si by Al [34, 43, 44], Ga [45], Fe [46], V [47], Ti [48, 49], Nb [50], Mn [51] and Cr [52] to obtain and investigate acidic sites that provide a new playground to drive catalytic reactions. The derivatives were synthesized by the addition of a salt of the supplementary element in the designated quantity to the synthesis mixture of the hydrothermal synthesis. [33, 41, 53, 54] The degree of isomorphous substitution of framework silicon by trivalent atoms decreases in the order Al $\gg$ Ga $>$ Fe. The ratio of strong to medium-strong acid sites falls in the same order. [46] By investigating their acidic strength with the adsorption of NH_3 and microcalorimetry, the strength of the BASs was found to be decreasing in the order Al > Ga > Fe. [46, 55] This order is also present in isomorphous substituted zeolites. [56]

The structure is changed by the larger radii of the substitution ions T^{3+} aluminium ($r_{Al^{3+}} = 0.39$ Å) and gallium ($r_{Ga^{3+}} = 0.47$ Å) in comparison to silicon ($r_{Si^{4+}} = 0.26$ Å). [57] In accordance with the Löwenstein rule [58], it is not possible to form $Al^{IV}-O-Al^{IV}$ connections due to the unfavorable radius ratio between oxygen and aluminium. The anion bridge between two Al ions in their lowest coordination state four (denoted as Al^{IV}) is unstable, and a structure with a higher coordination number at one of the Al centers is favored. Consequently, the highest amount of Al in structures of aluminium and silicon tetrahedra is 50 %. Results of IR spectroscopy and XRD reveal the absence of long range order of TO_4 tetrahedra within the amorphous walls. [33] In any case, the maximum size of the primary mesopores was 2.5 nm [38, 53] to 4 nm [54] for MCM-41 type samples. Al-MCM-41 produced by co-condensation has approximately the same specific surface area as aluminium-free MCM-41. Depending on the publication, the pore volume is constant [59] or decreases [60] with increasing Al content. As another T^{3+} element, boron ($r_{B^{3+}} = 0.11$ Å, [57]) can be incorporated in the structure of silica-alumina materials. Its diameter is smaller than the one of Si. In contrast to zeolites, the unit cell size increases with increasing content of boron while for increasing Al content, only a weak correlation was found. [54] However, upon calcination, B leached out of the lattice and the diameter of the pores decreased. A hexagonal structure, which is characteristic of the mesoporous material MCM-41, was obtained until a Si/Al or Si/B ratio of ten. The structure closest to siliceous MCM-41 is achieved at a low T^{3+} content. [54] Nevertheless, the pore ordering decreased with increasing amount of heteroatoms that were incorporated in the walls. [59]

2.3 ACID SITES ON MESOPOROUS MATERIALS

Acidity may be the most important property in zeotype materials. Often, the reactive centers in cracking and synthetic reactions are based on acid sites. [61] The following sentences will define acid sites and explain their general properties. Afterwards, the structures of acid sites on amorphous silica alumina (ASA) will be described in detail.

Both types of acidic sites, namely BASs and LASs, are present on the surface of each zeotype material containing T^{3+} in addition to Si. The types differ in their behavior towards electrons and protons (H^+). BASs [62] can donate a proton (back reaction of Equation 2.1) and are schematically drawn in blue in Figure 2.1. The strength of a BAS is defined as the ability to donate a proton to a neutral base according to the HAMMETT function H_0 in Equation 2.2.

$$H^+ + B \rightleftharpoons BH^+ \tag{2.1}$$

$$H_0 = -\log a_{H^+} \frac{f_B}{f_{BH^+}} \tag{2.2}$$

a_{H^+} is the activity coefficient of the proton while f_B and f_{BH^+} are the activity coefficients of an uncharged base and its conjugate acid. [63]

Lewis sites are electron acceptors. [64] Their Hammett function (Eq. 2.4) is defined differently, taking into account the different mechanism with a_A now being the activity coefficient of the electron acceptor. B is again the neutral and electron rich base. [63]

$$A + B \rightleftharpoons AB \tag{2.3}$$

$$H_0 = -\log a_A \frac{f_B}{f_{AB}} \tag{2.4}$$

Generally, LASs are deficient in electrons/electron density and are electron acceptors. In ASA, they are located at the T centers in the structure, where the T is threefold coordinated. [65] In a "normal" or humid atmosphere, they are often covered by adsorbants like H_2O. [66] Just upon dehydration, the actual LEWIS site is created by the exposed Al atom. Thus, depending on the condition the material is handled and investigated, and especially the hydration level, the number of LASs varies significantly. Structurally, 4- and 5-coordinated Al within the framework act as LASs as well as 6-coordinated Al in extra framework aluminium (EFAL). [67] The direct bond of a probe molecule with Al in zeolite Y was shown spectroscopically by KAO AND GREY [68]. During the process of dehydration at 400 °C, dealumination occurs as well, forming EFAL with octahedral Al. This process creates LEWIS sites that are structurally similar to Al_2O_3. [67, 68] The acid strength of BASs is often and structurally linked to LEWIS sites as will be explained below.

The strength of BASs depends on the ability of the environment to stabilize the corresponding base. This is mostly done by delocalizing electrons over as many oxygen atoms as possible. [65]

There are two structural extreme forms of BASs in silica-alumina materials that are presented in Figure 2.1, **a** and **e**. The forms in between have slightly different bond situations that are all described in literature. An overview will be given in the next paragraph.

The two forms of BASs at both ends of this chain are (i) a silanol group in proximity to a (Lewis acid) Al center which causes the acid site by its inductive effect [69] (cf. Figure 2.1, **a**) and (ii) a structurally incorporated Al replacing a Si atom creating a negative charge which is compensated by a proton. [70, 71] (cf. Figure 2.1, **e**) In between those edge cases, all intermediate forms are described and most are also characterized. Evidence for weak acid sites in MCM-41 was found by diffuse reflectance infrared FOURIER transform spectroscopy (DRIFTS), since Al has an inductive effect to a SiOH group next to it as shown in Figure 2.1, **a**. [69] In the next picture, the SiOH group tilts towards an Al centered LAS and is attracted by it such that after deprotonation, the corresponding base is stabilized. [70, 71] (cf. Figure 2.1, **b**) From the tilted groups, a flexible coordination between the Al and the silanol can be formed. This can be either Al pseudobridging with the SiOH group forming a pseudobridging silanol (PBS) (cf. Figure 2.1, **c**) [71, 72] or a coordination, which is relatively flexible (cf. Figure 2.1, **d**). In the end of that series, an acid site can also be a bridging hydroxyl group between two Si atoms. (cf. Figure 2.1, **f**) The sites in this series differ slightly in atom distances and therefore, in their bond type.

In amorphous materials, the acidic strength is lower than in zeolites. [72, 73] This is related to the longer SiOH···Al bond in amorphous materials (2.94 to 4.43 Å) compared to zeolites (1.88 to 2.0 Å). [74] The reason for the shorter bond length of zeolites is their crystalline nature comprised with a higher degree of structural ordering. The amorphous material therefore has longer bonds and weaker BAS, [71] hence, resembling more the situation in Figure 2.1 **a** than Figure 2.1 **e**.

One objective criterion to relate the strength of a bond is the deprotonation energy i.e. the energy needed to separate the conjugated base from the proton. [75] The H/D exchange of benzene is rather difficult ($pK_a = 43$), therefore, it acts as a criterion for the presence of very strong or even superacid sites.

Various studies using mostly ssNMR [70, 72] and quantum chemical calculations [78] state that PBSs are the majority species and there is only a small amount of zeolitic bridging OH groups. Eventually, in an extensive ssNMR study PERRAS ET AL. [79] did not observe bridging silanols above the limit of detection. The BASs may have been present but undetectable in this analysis. In a next study with deuterated ASA back-exchanged by C_6H_6 with protons, the low amount of bridging acid sites became observable. [70] The strength can be further increased if a high amount of Al leads to two Al centers next to the same SiOH group, which are comparable to the acidic strength in zeolites (see Figure 2.1, **g**). Those sites are not contradicting the LÖWENSTEIN rule

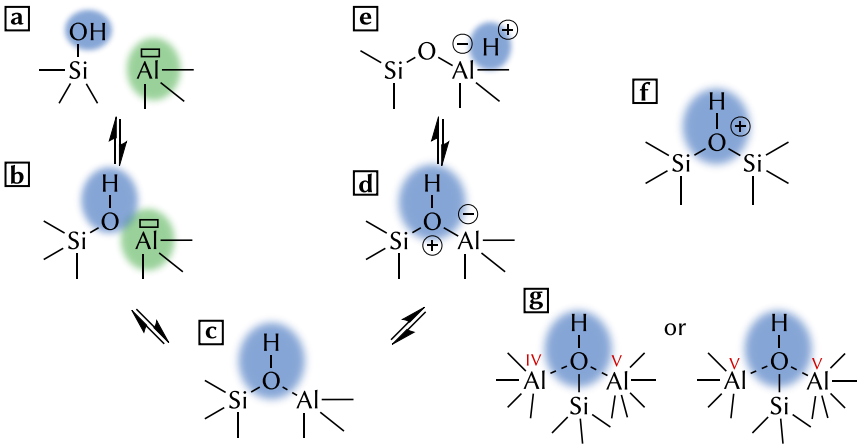

Figure 2.1: Schematic representation of possible structures of LAS (green) and BAS (blue) in silica-alumina materials. **a** and **e** are the edge cases, a silanol next to a LAS and a bridged oxygen, forming a four-coordinated Al that is charge-compensated by a proton. **b** is the silanol tilted towards the Al. In **c**, a pseudobridging silanol (PBS) is formed, which in **d** is coordinated in a zwitterionic form. **f** represents a bridged silanol between two Si. In **g**, an acid silanol close to two Al centers possesses an increased strength. Modified from refs. [65, 71, 76, 77].

since at least one site is Al^V with which a direct neighborhood is allowed. [71] Only a minority of acid sites is mainly responsible for the catalytic activity, and even challenging reactions can be activated by ASAs in the same way as by zeolites. [70, 77]

There is an ongoing discussion on the existence of superacidity in zeolitic catalysts. [80, 81] Superacid sites possess an acid strength that exceeds the strength of 100 % H_2SO_4 [82, 83] with a $H_0 \leq -12$. [84] In zeolites, the threshold for superacidity was set to a trimethylphosphine oxide (TMPO) signal of 86 ppm which corresponds to a Si–H distance of 2.5 Å. [85–87] Since the H/D exchange of benzene was possible in the above mentioned study of Salvia et al. [70], those zeolitic acid sites seem to be superacids.

Through combined Fourier transform infrared spectroscopy (FTIR) and density functional theory (DFT) studies, the influence of the bond angle T–O–T for the strength of BASs was proposed: The higher the angle, the stronger the bond which translates into a weaker acid site strength. [77] However, others see no correlation between the angle and the deprotonation energy. [75] The vibrational energy of the OH bonds is another factor probably indicating the BAS strength as investigated in several studies. However, it cannot be used as such, [75, 88] only vibrational energies during interaction with a hydrogen bonded probe molecule can be used as indication for the acid strength. [65, 77, 88] Additionally, BASs can form upon water-molecule adsorption on Al atoms, even when they are tetracoordinated. [77] Three factors

enhance the likelihood of water attachment. Electronegative ligands enhance the electrophilicity of the Si atom. Al–O–Si bonds play such a role in silica-alumina materials. A high nucleophilicity of the ligand also eases the formation of pentacoordinated Si. Additionally, geometric constraints induced by Al-doping enforce the formation of pentacoordinated Si.

In summary, this section has established the fundamental nature of acid sites in silica-alumina materials distinguishing between BRØNSTED and LEWIS acid sites and their interplay to form superacid sites. While zeolites and amorphous materials show differences in their bond lengths around acid sites, both can exhibit significant acid strength. The presence and distribution of these sites plays a crucial role in determining the material's catalytic behavior. Understanding these structural characteristics and acid-site types provides the foundation for the next section, which will examine the various analytical techniques and characterization methods used to evaluate the acid sites. Those methods are essential for precisely determining the type, strength, and accessibility of the acid sites discussed above.

2.4 CHARACTERIZATION METHODS FOR ACID SITES BESIDES NMR

The characterization of the acid site properties is of utmost importance to pinpoint reactive sites and the subsequent enhancement of material properties. A range of techniques is available for the characterization of acid sites on the surface of mesoporous materials and zeolites. A very simple approach is the titration of the sample of interest with a HAMMETT indicator to observe the color change spectroscopically. [63, 89] While the strength can be determined by a series of appropriate indicators, no information on the type of acid site can be drawn from that method. [63] To gain the ratio between the structure forming elements (Si and T^{3+}), the application of elemental analysis is the first step to approach the number of acid sites in the material. Generally, the number of acid sites increases with the amount of T^{3+}. The number of LASs keeps increasing, while the number of BASs reaches its maximum at Si/Al = 5. [90]

The (X-ray) diffraction-based methods that were used to characterize zeolites and the local structure around BASs cannot be applied to amorphous materials since those lack a long-range order. Only the structure of the pores can be observed by XRD through BRAGG reflections at $2\theta < 10$. [41] IR spectroscopy is very often used to probe surface acid sites, either directly or by means of probe molecules. [91–93]

Techniques such as attenuated total reflectance (ATR) and diffuse reflectance infrared FOURIER transform spectroscopy (DRIFTS), which do not require strict sample preparation, are of particular interest

for direct detection, since the preparation of KBr wafers for transmissive IR spectroscopy can induce K^+ exchange on the BAS, leading to a shifted band. An exchange of framework cations by aluminium causes a shift of most of the bands towards higher wavenumbers and informs about the degree of extra-framework cations as well. BASs and terminal silanols possess specific vibrational bands that depend strongly on the surrounding lattice characteristics. [93] However, not all OH groups can be detected as Si(OH)Al bridges escape IR detection although they must be present as evidenced by nuclear magnetic resonance (NMR). [94] In principle, a weak acid site possesses a strong bond which belongs to a band with high energy (high wavenumber). However, the strength of an acid site can only be assessed when the material is closely compared to an analogous material analyzed at the same conditions. [93] For example, it is possible to track the formation of BASs from LASs, which are formed when water is added. [94]

The probe molecule CO probes the "polarizing power of the cation or, in other terms, [...] its Lewis acidity". [91] Upon attachment to hydroxyl species, especially at low temperature, a $-OH-CO$ band formation was observed and related to variations in hydroxyl acid strength due to interactions between different species within and without the framework. [93] The application of CO for LAS measurements solely is further confirmed by Leydier et al. [95] by combining IR and DFT. The only correlation was found between the electrostatic field and the shift of the characteristic CO stretching vibrational frequency $\tilde{\nu}_{CO}$.

Pyridine also chemisorbs on the surface of solids and was therefore already used to determine the amount of acidity before using it as an IR probe molecule. IR spectroscopy allows for the determination of acid sites since pyridine is a relatively strong base ($pK_B \sim 5$, but weaker than ammonia with $pK_B \sim 9$) that is intended to not deprotonate the weak acid sites. [91, 96, 97] It attaches to both types of acid sites differently: $PyrH^+$ forms on BASs and the ring-nitrogen attaches to a LAS resulting in characteristic adsorption signals. It is also possible to detect the strength of the acid sites via the shift of the vibrational band. [93]

TPD is used very often to determine the the amount and strengths of surface acid sites. The material is saturated with appropriate molecules within a calorimeter. After removal of the physisorbed molecules, a temperature program is started during which chemisorbed probe molecules desorb at a temperature belonging to their dissociation energy. The respective amount (measured as concentration in the gas phase) is related to the amount of one type or strength of acid site. Ammonia (NH_3) is widely used because it is cheap and easy to handle. [98] The desorption mostly has two peaks, one at low temperature (*l*-peak) and one at high temperature (*h*-peak). The *l*-peak does not represent the desorption from weak sites but is rather a consequence

of the saturation of the material with NH_3. During the saturation process, the formed ammonium ion (NH_4^+) ions bridge to additional NH_3 molecules via hydrogen bonding. This weak bond then causes the *l*-peak which, in addition, is also dependent on the experimental conditions, i.e. the evacuation time after the saturation. The longer the evacuation, the smaller the *l*-peak. The *h*-peak then represents the acid sites of different strengths. The method, however, is not able to extract structural information about the acid sites and cannot differentiate between LASs and BASs. Coupling TPD with other methods allows to extract more information about the acid sites. [93, 98, 99]

2.5 PROPERTIES OF SUPPORT MATERIALS UTILIZED IN THIS STUDY

Al-MCM-41 materials are often described and used for various catalytic reactions like different cracking reactions [50, 60, 100–102], dehydrogenation [59], hydrodeoxygenation [103] and oligomerization reactions [6, 104, 105]. However, the properties of the material itself do not present uniform trends across all cited studies. They strongly depend on the conditions of synthesis and associated post-treatment. Therefore, contradicting trends are extracted from literature and are presented here, limiting the selection to materials that were synthesized hydrothermally with both elements Si and Al in the synthesis solution. Supports prepared by grafting methods (e.g. of Al to siliceous MCM-41) are not considered here.

The Al source used for synthesis can very much alter the embedding and coordination of Al within the framework. After synthesis with sodium aluminate, calcination causes the interchange of some tetrahedral sites to octahedral EFAL sites which are desired in the cracking reaction. [55, 60] With $Al(OiPr)_3$, the structure was more stable towards the calcination procedure and no octahedral Al species were formed. [106] Other sources are, e.g., $AlCl_3$ [103], $Al_2(SO_4)_3$[50] and $Al(OH)_3$. [105] The amount of acid sites is not fixed for the type of material and not even for one synthesis batch. It can be adjusted by the dosage of water or by dehydration to the benefit or to the detriment of the BASs. LASs are converted to BASs by partial hydrolysis. [94] Luo et al. [73] present their material with Si/Al ratios between 16 and 80 which was prepared in an alkaline templating hydrothermal synthesis pathway. Despite being handled in a water-free atmosphere, their material (most likely the one with Si/Al = 16) showed no LAS or them being below the detection limit. BASs and silanols are present, the BASs in a much lower concentration than the silanols. The authors describe the BASs as "zeolitelike", indicating the presence of bridged Si(OH)Al groups.

With increasing Al content, the following observations were made:

1. The overall number of acid centers increases with more aluminium. [59, 103, 107]

2. The number of acid centers per Al atom decreases.

3. The acid strength may either increase, [59, 107] or decrease. [60] A decrease in acid strength is explained by the decrease in Sanderson's overall electronegativity, which, on average, increases the bond strength to protons which have a low electronegativity. [107, 108] In contrast, with regard to the structure of a BAS, the probability increases to have two Al atoms close to the acid proton. This stabilizes the corresponding base and therefore leads to a stronger BAS. Additionally, the surface concentration of Al increases the acid strength [59] through interactions between LASs and SiOH groups. [71]

4. Generally, both the surface area and the pore volume decrease. [60, 103, 106]

In the contrasting case of reducing the amount of Al by dealumination, a simultaneous loss of bridging OH groups and Al was proposed. [109]

In terms of characterization by NMR, the amorphous structure of the material is formed during the calcination step. The work of Viale et al. [94] and Kosslick et al. [55] show that in comparison to the uncalcined material, the Al signal of Al-MCM-41 gets significantly broadened because the Al sites are less defined in the amorphous structure. This is a little less observable in ^{29}Si spectra. Signals that represent tetrahedral Si atoms bound to one Al (Q^4(1Al)) or one OH group (Q^3) overlap (*vide infra*, Section 4.2.4). Si(OH)-Al bridging silanol sites cannot be directly observed by IR spectroscopy, neither in Al-MCM-41 nor in crystalline silica alumina materials (zeolites). However, the existence of those sites is evidenced by detection with probe molecules. Those sites escape direct detection due to their interaction through hydrogen bonding with other surface species. The transition of BASs to LASs by hydration can be followed by IR spectroscopy. [94]

Ga-MCM-41 supports are not as abundant in literature as their Al counterparts and less frequently used as catalysts. Nevertheless, there are examples of Ga-exchanged silica for the catalytic conversion of light alkanes, [110, 111] dry reforming of methane, [112] and other alkylations, isomerization and disproportionations. [33]

Initially, Ga atoms were successfully incorporated into the MCM-41 lattice during the hydrothermal synthesis utilizing $Ga(NO_3)_3$. [45, 110, 113] During the calcination process, however, Ga is also expelled from the structure to some extent, indicating that the amount of Ga that can be incorporated into the structure is limited. [110, 114] It was found, that the Löwenstein rule also holds for gallosilicates. [115] No contraction of the pores was observed during calcination in the samples with a low content of Ga (Si/Ga = 30). [110] The surface area is a bit smaller than in siliceous and Al-MCM-41 materials but this

might also vary with the gallium source and the synthesis procedure in general. [110] In a series with increasing Ga content (also synthesized with $Ga(NO_3)_3$), the surface area decreases in the same way as in Al-MCM-41. [111]

Heterogeneous BASs of different strengths were observed in a Ga-MCM-41 with Si/Ga = 16 by Pyr-IR. Weak sites form hydrogen-bonded adducts with pyridine, while strong sites are able to protonate it. Structurally, BASs of various strengths result from framework Si(OH)Ga hydroxy groups, LASs from coordinatively unsaturated Ga^{3+} ions (extra framework species). [113, 114] Likewise, extra-framework gallia species in Zeolite Socony Mobil-5 (ZSM-5) are assigned to be catalytically active as well. [114]

A more exotic way to add gallium to a MCM-41 support is to apply Ga metal to the material. [45, 116] Ga is then found as liquid metal between the particles and not within the mesopores of the material. However, there are bonds forming between surface SiOH and the metallic Ga incorporating it into the structure. [116]

A mixture of Ga and Al in MCM-41 reveals that more Al than Ga is expelled during calcination, though this is expected to be less stable as the ratio of the atomic diameters, and therefore, the size of the tetrahedra increases in the order Si < Al < Ga. [45]

3

MECHANISM OF BUTENE DIMERIZATION

An extensive review on Ni based di- and oligomerization of olefines is published by Olivier-Bourbigou et al. [117]. The history of olefin metathesis is summarized in the 2005 Nobel lecture of Chauvin [118]. A more general view on mechanistic investigations of BAS catalyzed reactions is offered by Chizallet et al. [119].

3.1 HISTORY

Without catalyst, ethylene polymerization can be performed at extreme pressures of 1000 to 2000 atm and temperatures of 200 °C with traces of oxygen as activating species. [120] First catalysts that were able to decrease the reaction temperature and pressure were introduced in 1942. [121] Activated metal oxides from the iron group (Fe, Co, Ni), whether supported or not, produced a mixture of products ranging from di- and trimers to highly viscous or solid polymers. The product distribution depended on the reactant. In their ethylene polymerization study with $AlEt_3$, Ziegler et al. [120] unexpectedly found butene formation instead of expected oligomer growth. They found that traces of nickel in the autoclave stopped the chain elongation reaction at the Al centers. The effect, simply called "nickel-effect", started the success story of Ni based catalysts for olefin dimerization. Lewis sites apparently activate Ni^0 to form cationic Ni species which are very active in catalysis. Variation of ligands allowed for fine tuning the selectivity of the dimerization processes. In the late 1970s, the homogeneous Dimersol process for the dimerization of propene was the first to be industrially relevant. The heterogeneous OCTOL process is used industrially for butene dimerization to obtain linear and low-branched dimers on Ni-ASA catalysts. [122, 123] Since then, Ni-based catalysts have been used industrially in homo- and heterogeneous catalysis especially for the di- and oligomerization of ethylene, propylene and butenes which are available from cracking processes. Products are e.g. plasticizers, insecticides or octane boosters for gasoline. [117]

The primary objective of heterogeneous butene dimerization is octene production [117]. Key challenges remain in controlling selectivity: achieving linear products, positioning the double bond, and managing the distribution of higher olefin types. Understanding and directing the mechanism to the desired products is therefore a key point in research.

3.2 MECHANISMS

There are mainly two types of mechanisms that are involved in the dimerization of butene: 1) the carbenium ion mechanism and 2) the coordinative Ni catalyzed mechanism. Both shall be explained shortly.

CARBENIUM ION MECHANISM This mechanism is based on acid sites and mainly drives the production of highly branched products and oligomers. The substrate for this mechanism contains highly acidic BRØNSTED [124, 125] and/or LEWIS [13] sites that stabilize the carbenium ion intermediate following the MARKOWNIKOV rule. [126] Since the secondary carbenium ion is more stable, branched dimers are formed after the nucleophilic attack of a second alkene molecule. Furthermore, (branched) dimers with a double bond are able to form even more stable cations which are likely to continue the reaction to higher olefins. [127]

COORDINATIVE NI-CATALYZED MECHANISM Both, Ni^{+} and Ni^{2+} have been proposed as active sites. [4, 10, 117] This mechanism offers higher selectivity than the carbenium ion mechanism. To enable the mechanism, catalysts with lower acidity are needed to prevent reactions on acid sites and instead promote reactions on Ni sites.

The mechanism is a monometallic insertion mechanism as investigated by COSSEE and ARLMANN after whom the mechanism is named. [128–130] $TiCl_4$ and $AlEt_3$ are forming a Ti-Alkyl species by transmetallation. An alkene is added and forms a π-complex between the double bond and the metal. [131] The π-complex's stability critically determines the relative contribution of this mechanism versus the carbenium ion mechanism. [13] A second alkene also attaches to the metal with a π-bond. After forming a four-membered cyclic transition state, the alkene is inserted in the metal-methylene-carbon bond and elongates the chain. [127, 131]

3.3 CURRENT STATE OF THE ART

Butenes already dimerize on acid sites below 100 °C, with a selectivity of 96 % towards the branched dimethylhexene products. [132] Therefore, the role and selectivity of different acid sites was investigated since the 1980s by observing the product isomers, finding, that very strong BASs are able to produce linear oligomers. [133] By using an increasing amount of Ni, the selectivity to linear octenes was dramatically increased indicating that selectivity is related to the coordinative mechanism. However, acid sites are necessary in the Ni impregnation step to adsorb and bind Ni on the surface and create active sites. Interactions between nickel sites and nearby aluminium or acid sites were included into the outline of a redox mechanism (cf. Figure 3.1)

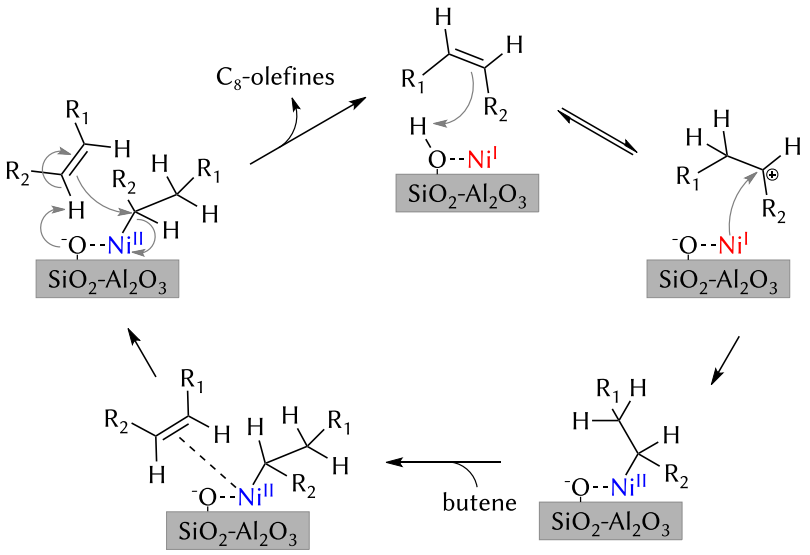

Figure 3.1: Outlined mechanism of the butene dimerization with a Ni^{+} – Ni^{2+} redox cycle and the formation of a carbenium ion in the first step. Adapted from ref. [1].

following the results of characterization and catalytic tests. [1, 4, 6] Neither a purely Lewis acidic [3] nor a non acidic support (SiO_2) [1] allows for a catalytic reaction. Apparently, two Si-O-Al sites (BAS) in close proximity stabilize Ni^{2+} but for a high selectivity, no surface BASs should act as reactive center. This is possible in a proton-free zeolite like zeolite A (LTA) which is ion exchanged by up to 6 % Ni^{2+} at reaction temperature of 160 °C and a pressure of 50 bar. [10] The selectivity is high due to the high ratio of the coordinative mechanism. Inversely, the amount of remaining surface BAS could be determined by detecting the isomer ratio of the two different dimethylhexenes of the 1-butene feeded reaction. [9] The activity is dependent on the Ni dispersion on the surface which increases with an increasing Si/Al ratio. [104] The active centers should be separated from each other to avoid cluster formation. [10] On the other hand, reactive Ni^{+} centers can form during the reaction from inactive Ni^{0} clusters. [4] This also explains the high amount of NiO that is used industrially. During the reaction, enough active sites are available, driving the activity.

As result of theoretical [134] and experimental [132] studies, cationic Ni-hydrides $[Ni-H]^{+}$ (Cossee-Arlman sites) are considered as active sites. However, they represent a minority species, which makes them difficult to identify through experimental means. [134] In this line, Ni sites in close proximity to BASs drive activity and selectivity as is shown in the mechanism in Figure 3.1. [3] The precise interplay between the acid sites and Ni is not yet fully elaborated. The characterization of the types of acid sites is therefore a key goal of this work.

Another point of view focuses on LASs. It was hypothesized that the electron deficient Al close to a Ni center withdraws electron density from Ni which enhances the LAS character of the Ni itself. [105] This, in turn, increases the probability of bond formation between an alkene and the Ni site, and following selective dimerization. Thus, also LASs might play a role for selectivity in the interplay with Ni sites.

Given that 2-butene is the only compound capable of forming methylheptene, it is vital that the isomerization process is controlled in order to achieve the desired results. [10] The commonly used Raffinate III is a mixture of mainly but-2-enes and butanes, [127] while pure 1-butene is often used as a model compound to test the reaction without preceding isomerization. [12] Additionally, 2-butene is more stable, so reactivity decreases in the order 1-butene $>$ *cis*-2-butene $>$ *trans*-2-butene. [12] The stabilization of the more unstable intermediate with a terminal cation during the dimerization of 2-butene is a crucial step in the formation of the favored methylheptenes. This step of stabilization is likely to be the key factor in achieving selectivity.

In summary, the dimerization of butenes is a complex process governed by the interplay of Ni sites, acid sites, and reaction conditions. The selectivity and activity depend critically on the nature and proximity of LASs and BASs, Ni dispersion, and the specific isomerization of butene precursors. The stabilization of reaction intermediates, particularly during 2-butene dimerization, emerges as a key factor in achieving desired methylheptene formation.

4

NMR SPECTROSCOPIC INVESTIGATIONS OF SILICA-ALUMINA MATERIALS

ssNMR is an important extension to other techniques for catalyst characterization due to its strength in probing structure and dynamics. It is sensitive to chemical bonding states and interactions, e.g between probe or reactant molecules and the catalyst, as well as to the oxidation state of atoms. In contrast to other methods, ssNMR probes the local structure around the nucleus while at the same time being a bulk method and observing the whole sample within the active coil volume. Unlike X-ray methods, which can only detect ordered regions, ssNMR can characterize both amorphous materials and defects.

In order to maintain a concise discussion of magnetic resonance, fundamental principles are presumed to be understood. The reader is referred to the common textbooks on NMR theory for more detailed descriptions and a thorough mathematical treatment. [135–141] This chapter provides a brief overview of diamagnetic and paramagnetic shift terminology, followed by practical aspects of ssNMR for (amorphous) materials.

One of the strongest advantages of zeolitic and mesoporous silica-alumina materials is their tunable properties. The analysis of it is therefore key for a sound understanding and the ability to further improve the material. As the materials are insoluble, ssNMR is one of the central methods to characterize the bulk. It is possible to conduct direct measurements on nuclei that are present in the material itself (^{1}H, ^{27}Al, ^{29}Si, ^{71}Ga) or to use probe molecules to specifically probe the surface. Those measurements are described in Section 4.2.

It is to note, that most literature was found to describe experiments with microporous zeolites and as the general sample composition is the same in mesoporous amorphous materials, the methods should in general work for both types of material. The main difference is that ASAs are amorphous, whereas zeolites have a crystalline lattice. Additional contrasts will be mentioned in the corresponding sections. The larger pore size of ASA provides more space for probe molecules, which can be used to assess the properties of mesoporous materials. Additionally, this should result in less sterical hindrance. Interactions of the surface with probe molecules, that are hindered at small pores, are possible in materials with larger pores. This opens the space for further characterization methods.

Especially the acidic properties are of significant importance since they are often acting as catalytic centers. Most methods described hereafter are able to probe this, however, none of them is able to reveal

the full picture of the behavior of the acidic sites. Direct measurements of the involved nuclei reveal the coordination number and the local environment. Probe molecules interact with the acidic sites and report on their otherwise hidden characteristics. Advantages and limitations of each method are described in this chapter and complementary methods are mentioned in Section 4.3.

4.1 GENERAL ASPECTS

The terms that describe interactions between a nuclear spin and its environment are summarized into an overall nuclear spin Hamiltonian. The terms that describe the nuclear spin interactions involved in the system are given in Equation 4.1.

$$\hat{\mathcal{H}} = \hat{\mathcal{H}}_Z + \hat{\mathcal{H}}_{CS} + \hat{\mathcal{H}}_{DD} + \hat{\mathcal{H}}_J + \hat{\mathcal{H}}_Q + \hat{\mathcal{H}}_{HFI} \tag{4.1}$$

Here, $\hat{\mathcal{H}}_Z$ describes the ZEEMAN interaction which is the energy splitting between the magnetic sublevels of the nuclear spin. The chemical shift $\hat{\mathcal{H}}_{CS}$ arises from the interaction of a nuclear spin with the induced magnetic field of the electronic systems within the external magnetic field. The interaction between an electric field gradient and the nucleus with $I > 1/2$ is represented in the quadrupolar term $\hat{\mathcal{H}}_Q$. $\hat{\mathcal{H}}_{DD}$ and $\hat{\mathcal{H}}_J$ are the direct and indirect magnetic interactions between two nuclei, respectively. $\hat{\mathcal{H}}_{HFI}$ comprises the hyperfine interaction between electron and nuclear spins. This latter interaction plays a crucial role in paramagnetic NMR with an unpaired electron in proximity to a nucleus, and is further discussed below.

4.1.1 *Diamagnetic Chemical Shift*

The diamagnetic chemical shift is a representation of the LARMOR frequency of a single nucleus. Its origin is the electronic environment of the nucleus. The energy differences between two nuclei ω in different environments are field dependent, however, for a common, field independent description, the chemical shift is referenced with a known standard of a frequency ω^0_{ref}. By using the LARMOR frequencies ω^0 of the nuclei, the general description

$$\delta = \frac{\omega^0 - \omega^0_{\text{ref}}}{1/2(\omega^0 + \omega^0_{\text{ref}})} \tag{4.2}$$

can be simplified to

$$\delta = \frac{\omega^0 - \omega^0_{\text{ref}}}{\omega^0_{\text{ref}}}. \tag{4.3}$$

The simplification is possible since the difference between ω and ω_{ref} is in the range of 10^{-6}. [135–137]

The chemical shift scale is decreasing from left to right. This is due to historical reasons, as NMR measurements with a variable $\boldsymbol{B}_0$ field were used in the past. To keep the form of the spectra, the direction of the chemical shift scale was defined to be inverse (cf. Figure 4.1). Therefore, the commonly used descriptions of signals shifting *upfield* or *downfield* are based on the magnetic field scale.

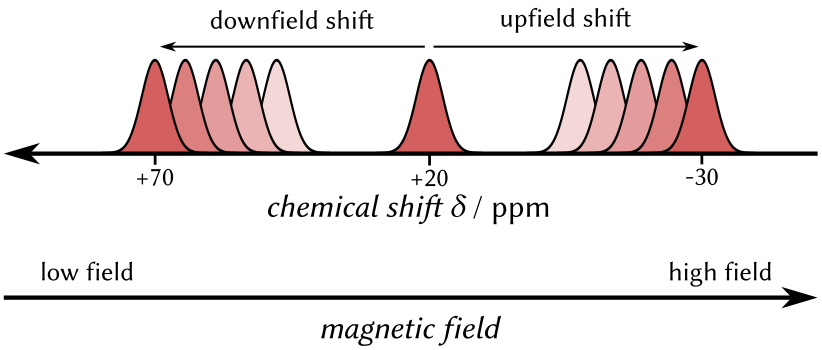

Figure 4.1: Relations between magnetic field and chemical shift and descriptors commonly used in NMR.

4.1.2 *Paramagnetic Chemical Shift*

When paramagnetism is introduced into an NMR sample, virtually all characteristic NMR properties are affected. The isotropic shift is changed as well as the anisotropy. Nuclei in proximity to the paramagnetic centers are strongly affected in their relaxation behavior (spin-lattice relaxation time constant (T_1) and spin-spin relaxation time constant (T_2)) which in turn changes the linewidth of the signal and potentially broadens the signal beyond observability. [142]

The experimental isotropic chemical shift δ^{exp} is composed of two main components: the diamagnetic shift δ^{dia} and the paramagnetic shift δ^{HF} resulting from the hyperfine interaction (HFI) between electron spin and nuclear spin. The HFI in its full form has exactly the same form as a heteronuclear coupling interaction which causes a splitting of the peak. However, in contrast to it, the former causes a change in the chemical shift. This is caused by the very short relaxation time of the electrons which is in the order of magnitude of 10^{-14} to 10^{-8} s, which is considerably shorter than that of nuclei (ms to s range). Consequently, the nucleus effectively interacts with the time-averaged electronic magnetic moment rather than its instantaneous value. This interaction exhibits identical characteristics to a chemical shift. [143] The paramagnetic shift δ^{HF} is controlled by two parts: the isotropic contact shift and the anisotropic dipolar shift as given in Equation 4.5.

$$\delta^{\text{exp}} = \delta^{\text{dia}} + \delta^{\text{HF}} \tag{4.4}$$

$$\delta^{\text{HF}} = \delta^{\text{contact}} + \boldsymbol{\delta}^{\text{dipolar}} \tag{4.5}$$

The FERMI contact shift δ^{contact} represents the electron density at the nucleus of interest. Since this is a purely isotropic term, it considers the electron density at the nucleus in a spherical environment. [136, 144, 145] The dipolar shift arises from the dipole-dipole interaction between electron and nuclear spins. Due to its orientation-dependent (anisotropic) nature, it is represented by a matrix $\boldsymbol{\delta}^{\text{dipolar}}$. The magnitude and characteristics of this shift are determined by both the spatial position and orientation of the electron spin relative to the nuclear spin, resulting in a complex spectral pattern rather than a single averaged line. [143, 145]

Both δ^{contact} and $\boldsymbol{\delta}^{\text{dipolar}}$ are inversely proportional to the temperature, however, both components can be of opposite sign. Therefore, there is no separate experimental access to those two values.

In the regime of fast relaxation, the linewidth is mainly determined by the T_2 and the bulk magnetic susceptibility (BMS). The BMS possesses isotropic and anisotropic contributions which effectively shift the signal and smear its lineshape with an approximated GAUSSIAN. [142, 143] The relaxation time constants are strongly enhanced due to the coupling with unpaired electrons. This effect is known as paramagnetic relaxation enhancement (PRE). [143] T_1 is especially enhanced in the proximity of paramagnetic centers allowing for mapping the distribution of paramagnetic centers in a mixture. Depending on the proton distribution, in other cases, the relaxation is mediated by spin diffusion in such a way that only a common T_1 is observable. On the experimental side, the fast relaxation shortens the waiting time between two experiments and beneficially allows more accumulations per unit time.

The electrons also massively decrease T_2 and therewith increase the linewidth up to the complete disappearance of the peak. However, it is not predictable whether a signal is still visible or not. Information or measurements on the overall magnetization of the sample can support the estimations. [142]

In paramagnetic systems, the above mentioned interactions fundamentally modify nuclear chemical shielding, resulting in dramatic chemical shift alterations. These interactions can induce chemical shift deviations spanning thousands of ppm from diamagnetic reference values, with the deviation direction being unpredictable. Therefore, conventional signal assignment methodologies become ineffective. Comprehensive signal detection necessitates extremely broad excitation and acquisition bandwidths. To counteract excessive signal linewidth, researchers typically implement rapid magic angle spinning (MAS). [142] Additionally, short pulse sequences are used to account for the fast relaxation. Single pulse experiments are often sufficient, a rotor-synchronized HAHN-echo sequence [146] can suppress background signals. Cross polarization (CP) [147, 148] can often only

be used with short contact times. Additional proton decoupling is usually not required. [142]

4.1.3 *Magic Angle Spinning*

In contrast to solution NMR, where molecules undergo rapid isotropic tumbling, ssNMR examines powdered samples consisting of randomly oriented small particles. This random orientation preserves all anisotropic interactions (chemical shielding $\hat{\mathcal{H}}_{CS}$, dipole-dipole coupling $\hat{\mathcal{H}}_{DD}$, and quadrupole coupling $\hat{\mathcal{H}}_{Q}$), resulting in broad powder patterns rather than sharp lines. Those interactions are all (in the first order) dependent on the second LEGENDRE polynomial $3\cos^2\theta - 1$ with θ being the orientation of a spin interaction tensor with respect to the external magnetic field. To cancel the relevant parts of the orientation dependence, the polynomial needs to be zero. This is the case for $\theta = \theta_M = 54.74°$, which is therefore called the *magic angle*. In MAS-NMR, the sample is spun around itself along that angle. [139, 140, 149] Figure 4.2 provides a simplified diagram illustrating the experimental setup. MAS has become a standard technique in ssNMR. The effect of MAS varies depending on whether the spectral broadening is homogeneous or inhomogeneous. For inhomogeneous line broadening, the MAS frequency must only exceed the spectral width of a single crystallite to result in sharp peaks. However, since the inhomogeneous chemical shift anisotropy (CSA) frequently surpasses the MAS frequencies, spinning sidebands appear at multiples of the MAS frequency ν_{MAS}.

For homogeneous broadening, such as $^1H-{}^1H$ dipolar coupling, the resolution improves only if the MAS rates exceed the static linewidth. [150] Consequently, experimental equipment undergoes continuous refinement. The proton resolution is significantly enhanced at high spinning frequencies, with spectra becoming largely free from homogeneous line broadening at 100 to 110 kHz. [151] The current MAS frequency record is at 170 kHz [152] tending towards 200 kHz. [153] Signals from quadrupolar nuclei are only partly sharpened since the second-order quadrupolar term is not averaged by rotation around θ_M. [154]

4.2 DIRECT NMR MEASUREMENTS

4.2.1 *^{1}H-NMR*

As the surfaces of the materials relevant to this work naturally contain protons, it is straightforward to directly detect those. Additionally, their spin $I = 1/2$, their large natural abundance, their high gyromagnetic ratio and the fast relaxation time allow for easy and fast detection. However, care is needed to choose the appropriate experimental con-

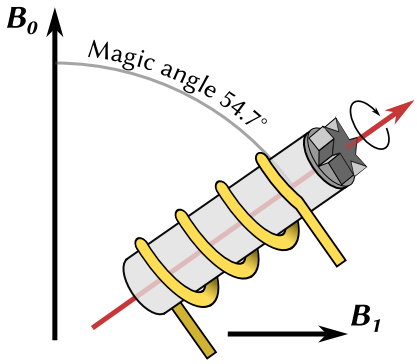

Figure 4.2: Schematic representation of the rotor tilted at the magic angle with respect to the B_0 field with the position of the coil and the orientation of B_1.

ditions for both sample preparation and the NMR measurement. [155] First and foremost: Porous materials are hygroscopic due to their large surface area and polarity and therefore attract water from ambient humidity as well as other volatile molecules from the laboratory environment. Heat treatment under inert gasses and vacuum is necessary to remove all foreign molecules prior to measurement. [155] Typically, the temperature is slowly increased under vacuum to 400 °C and kept for several hours or until the pressure drops to 10^{-2} to 10^{-3} mbar. [68, 155–158] In addition to the sample preparation, it is essential to select the measurement parameters with great care to avoid any distortion of the signal. This includes the room temperature shimming of the magnet, setting the magic angle and using low repetition rates as demonstrated by Kennedy et al. [155]. Additionally, the probe's proton background needs to be suppressed. High MAS frequencies suppress ^{1}H–^{1}H dipolar coupling, thereby enhancing spectral resolution. To this end, the proton chemical shift can be used for a quantitative evaluation of the acid density but not for the acid strength. [155]

As soon as the experimental prerequisites have been met, the spectra of zeolites allow for the assignment of various species. A series of ^{1}H spectra of zeolites are shown in Figure 4.3. The signals are relatively broad in comparison to signals in liquids. The chemical shift typically ranges between 0 and 16 ppm (referred to tetramethylsilane (TMS)), and can surpass the upper limit with signals of bridging silanols with a short O–H–O distance. [93] Signals close to 0 ppm represent hydroxyl groups at isolated metal centers such as =AlOH or –MgOH. Silanols are present between 1.3 and 2.2 ppm. [93] The protons of AlOH in extra framework aluminium appear between 2.6 and 3.6 ppm after the removal of structural aluminium sites, e.g., through steam treatment. [159] Different positions of BASs in zeolite materials do also have distinct chemical shifts: sites in super-cages of Zeolite-Y have a chemical shift of 3.6 to 4.0 ppm whereas those in smaller sodalite

cages show up between 4.8 and 5.2 ppm. [93] Although it is generally

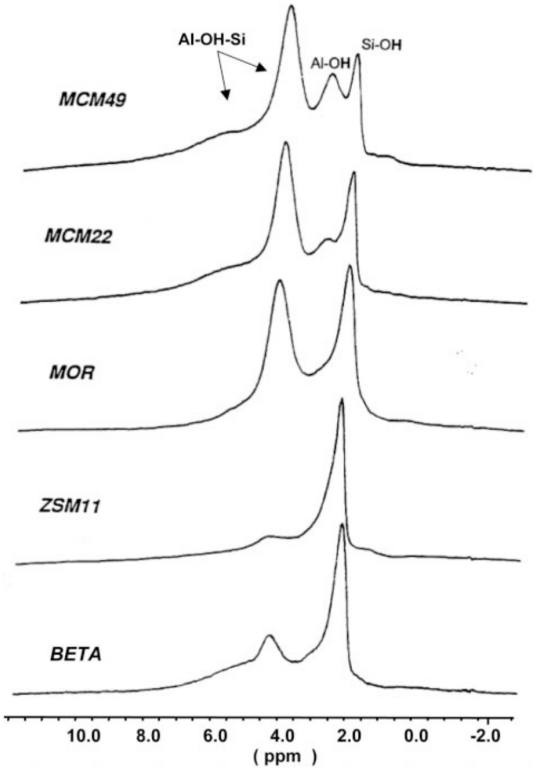

Figure 4.3: Representative ^{1}H MAS NMR spectra of different aluminosilicate zeolites which illustrate the distribution of hydrogen species in zeolites. Reprinted with permission from ref. [155]. Copyright 2004 Sage Publications.

accepted to link increasing chemical shift with increasing acid strength, this correlation is complicated by the narrow chemical shift range. [155] Correlations can only be drawn if there are no interactions with adsorbates, neighboring hydroxyl groups or the framework of the material. [160] Additionally, zeolites and mesoporous ASAs do have very different characteristics in their proton chemical shift, e.g. Al-MCM-41 in the calcined and dehydrated state shows only one signal at 1.8 ppm. [161]

4.2.2 ^{27}*Al-NMR*

The ^{27}Al nucleus has a nuclear spin of $I = 5/2$ and, therefore, possesses a nuclear quadrupole moment. With its natural abundance of 100 % and a fast relaxation time constant (T_1), spectra can be obtained relatively quickly. However, the quadrupolar interaction of 14 to 18 MHz, especially at low fields, can lead to broad and distorted spectra, rendering especially the tricoordinated Al (LAS) of the structure invisible. [87, 162] The problem of "invisible aluminium" especially

hinders the quantification of Al sites in the material. This issue specifically arises at low fields and low MAS frequencies and even at small flip angles. [162]

This has been overcome by either hydration to a symmetric tetrahedral framework Al site, or by using a probe molecule (TMPO) and 2D correlation spectroscopy between its ^{31}P nucleus and ^{27}Al in a HETCOR experiment. [87] However, in the first case, after hydration, the site is indistinguishable from a BAS. [87] Furthermore, additional 2D NMR techniques (MQMAS, homonuclear double quantum (DQ)-single quantum (SQ) correlation spectroscopy and dipolar mediated D-HMQC) are used to elucidate the coordination of aluminium in the structure. [72, 163–165]

In contrast to the threefold coordinated sites, four- five- and sixfold coordinated sites are easy to identify in a ^{27}Al spectrum at different chemical shifts. The signals of octahedral sites (sixfold coordinated) occur between -10 and 15 ppm while the tetrahedral (fourfold coordinated) signals are between 50 and 80 ppm. Fivefold coordinated Al occur in distorted environments and possess chemical shifts of 30 to 40 ppm. [162] In ASA, the fourfold coordinated Al is typically associated with lattice atoms, while octahedral Al often belongs to EFAL. NMR at the highest magnetic field strengths currently available is an effective technique for distinguishing $Al^{IV}-Al^{IV}$, $Al^{IV}-Al^{V}$ and $Al^{V}-Al^{V}$ correlations. [72]

In crystalline zeolites, Al occupies distinct positions in the lattice. AlO_4 tetrahedra are usually linked to four SiO_4 tetrahedra and therefore shows relatively well resolved signals. The effects of the quadrupolar characteristics are not particularly pronounced due to the high symmetry. In amorphous materials like Al-MCM-41, Al is the reason for disordered sites in the structure and with increasing Al content and upon calcination, the ^{27}Al sites get less defined and also transform from a fourfold coordination to five- and sixfold coordinated species. [55] This manifests itself in a broadening of the signals. [94] In a completely dehydrated material, the quadrupolar interaction is so strong that the resulting signals become very broad, making observation difficult or impossible. After hydration, however, a quantitative evaluation of the Al sites is possible after proper spectral decomposition. [166] To obtain the quadrupolar parameters from the peaks, they need to be fitted with the Gaussian isotropic model or the Czjzek model. [167, 168] The latter considers the charge distribution around a quadrupolar nucleus in amorphous solids which is not much dependent on the coordination number. [169, 170]

4.2.3 *Ga-NMR*

Two isotopes are NMR active and compared in Table 4.1. Especially the first- and second-order quadrupolar broadening of the Ga nuclei

causes the much lower NMR resolution and sensitivity than in analogous aluminium substances. [171] Due to the smaller quadrupolar splitting and higher gyromagnetic ratio, ^{71}Ga is in most cases preferred for the observation despite having the slightly lower natural abundance. However, tailored experimental parameters need to be

Table 4.1: Comparison of the two NMR active Ga nuclei. [115, 171]

Property	^{69}Ga	^{71}Ga
Spin	$I = 3/2$	$I = 3/2$
Natural abundance	60.4 %	39.6 %
Gyromagnetic ratio	$6.44 \cdot 10^7$ rad/(sT)	$8.18 \cdot 10^7$ rad/(sT)
Frequency at 9.4 T	96.28 MHz	122.33 MHz
Quadrupolar moment	$0.178 \cdot 10^{-24}$ cm^2	$0.112 \cdot 10^{-24}$ cm^2
rel. line width[1] (^{27}Al: 1)	6.64	2.01

chosen for the detection. Preferably, the detection is done at high fields and high spinning speeds (at 8 kHz, good results are possible), and short pulses are needed for excitation that translate in the higher bandwidth required for the large linewidth. [115] If a spectrum is acquired, the chemical shift also gives information about the coordination. Fourfold coordinated Ga has a chemical shift of around 140 to 160 ppm while sixfold coordinated Ga shifts upfield to 30 ppm. [172] As for Al, the peaks are fitted with the Gaussian isotropic model or the Czjzek model. The chemical shift and the intensity of tetrahedral Ga increase with increasing amount of Ga which enables to extract the amount from NMR spectra. [33, 45]

4.2.4 *^{29}Si-NMR*

^{29}Si has a spin of $I = 1/2$ and therefore possesses rather small linewidths. Unfortunately, it has a natural abundance of only 4.7 % and the relaxation times may be very long, depending on the compound. T_1 time constants of up to several hours have been observed in SiC modifications [162]. In ASA and zeolites the relaxation time is faster; mostly a waiting time between two repetitions of some minutes is sufficient to still obtain quantitative spectra. [173]

Especially in aluminosilicates, the chemical shift is relatively sensitive to its second coordination sphere environment. To mention the specific nomenclature (originally coming from silicones [175] and

1 The relative linewidth was calculated assuming the second-order quadrupolar interaction as the dominant line-broadening mechanism, the same EFG tensors and no asymmetry η. Details in ref. [115].

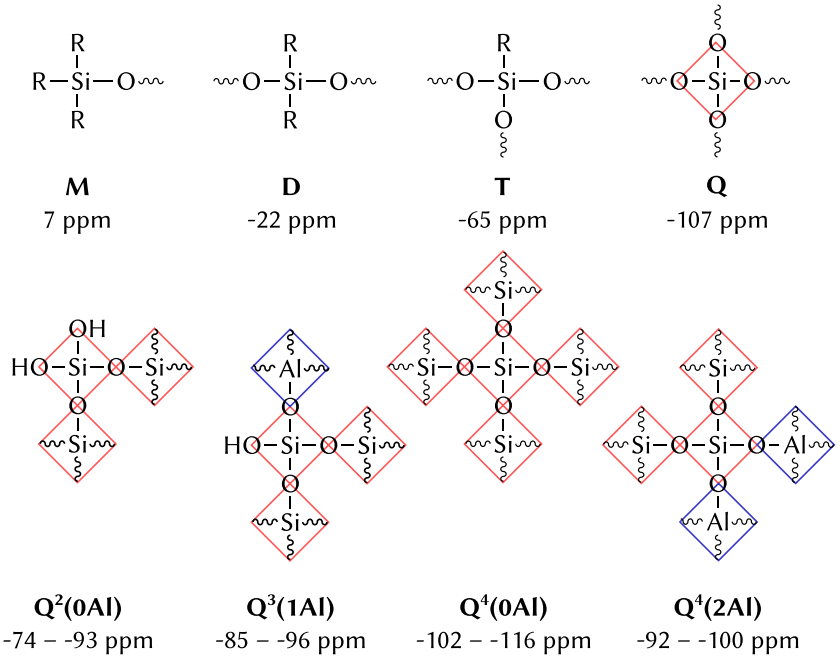

Figure 4.4: Structures and corresponding chemical shifts of siloxane species to illustrate the nomenclature. R represents an organic residue, and the wavy bond signifies a continuation of the structure. The values for the chemical shifts were taken from ref. [174] (M, D, T, Q) and ref. [162] (bottom row Q sites).

depicted in Figure 4.4), a framework Si surrounded by four SiO_4 tetrahedra is named Q^4(0Al) site. Exchanging a connected SiO_4 by AlO_4, the chemical shift changes from about $-(104 \ldots 116\,\text{ppm})$ downfield by $\sim 5\,\text{ppm}$ [162] but the site is still a Q^4 site. [19] Replacing a connected SiO_4 tetrahedron with an OH group makes it a Q^3 site, and so on. T sites, however, possess a single organic residue that is directly linked by a Si–C bond, D sites have two organic residues, and M sites three (c.f. Figure 4.4). Switching from Q to T to D to M sites, the chemical shift increases by 30 to 45 ppm for each transition. [174] In ASA, practically only Q sites are of relevance. Therefore, the chemical shift range is between -60 and $-120\,\text{ppm}$. [162, Chapter 4] The shift is also strongly dependent on the T–O–T angle (here: T = Si, Al) which can be used for the semi-empirical calculation of chemical shifts from the crystal structure. Therefore, this is of higher importance in zeolitic materials. [173, 176]

In crystalline zeolites, the signals of the different $Q^4(n\,\text{Al})$ sites (with $0 < n \leq 4$) are relatively sharp and easy to separate. [177] In ASA, the signals are much broader which makes it difficult to extract the single peaks. [178] This difference is exemplified in Figure 4.5. Equal to zeolites, in ASA, the signals of Q^4 sites shift downfield with incorporation of Al into the lattice. [94, 179]

The relaxation time constant T_1 in zeolites vary between 5 to 30 s and tremendously increase in amorphous materials with many more inequivalent Si sites. [173] In an ASA comparable to Al-MCM-41 with pore sizes of 8 to 20 Å, a ^{29}Si T_1 of 55 s was observed. [180] Adding molecular oxygen to the sample massively enhances the relaxation rate and allows for faster measurements but also reduces the resolution of the Si spectrum. [19] The large linewidth results from the variation of the T_2 relaxation which is related to the distance to paramagnetic oxygen. [19] Other paramagnetic impurities, however, do not have a strong influence on the ^{29}Si relaxation times, independent of their concentration. [173]

The silicon chemical shifts of a Ga-MCM-41 material with a silicon-to-gallium ratio of 20 at −110, −105.6 and −93.5 ppm are very similar as siliceous MCM-41 at −110.5, −101.7 and −92.4 ppm. Comparison with Ga-ZSM-5 suggests the assignment of the signal at −105.6 ppm to a Q^4(1 Ga) site. [111] In an Al-MCM-41 material, the signal at −100 ppm represents two overlapping signals: Q^4(4 Si) and Q^3(0 Al) possess the same chemical shift. [94] *J*-couplings in silica between a bridging oxygen and neighboring Si sites were measured and allowed to differentiate whether a Si is connected to two Q^4 sites or a combination of one Q^3 and one Q^4 site in its direct neighborhood. This requires, however, ^{29}Si and ^{17}O labeled silica and sophisticated pulse sequences. [181] In ^{1}H – ^{29}Si-CP experiments, the phenomenon is encountered that the longitudinal relaxation of protons in the rotating frame ($T_{1\rho}$) is faster than the polarization transfer. Dedicated pulse sequences like TORQUE (**T** **O**ne **R**ho **QUE**nching) must be employed to generate informative spectra and extract structural details. [182]

Taken together, the NMR spectroscopic properties of Si can be used to evaluate several properties of the materials under investigation. Nevertheless, there are a number of factors to consider when carrying out the experiment that are essential for a quantitative assessment of the results and for preventing erroneous conclusions.

4.3 ACIDITY MEASUREMENTS USING PROBE MOLECULES

An extensive review about the use of probe molecules to characterize the surface of materials, including general requirements, sample preparation and common pitfalls as well as the primary references is presented by DYBALLA [183]. A compilation of probe molecules and their application is written by ZHENG ET AL. [184] while SANDOVAL-DÍAZ ET AL. [93] more generally cover experiments with and without probe molecules in NMR and IR spectroscopy.

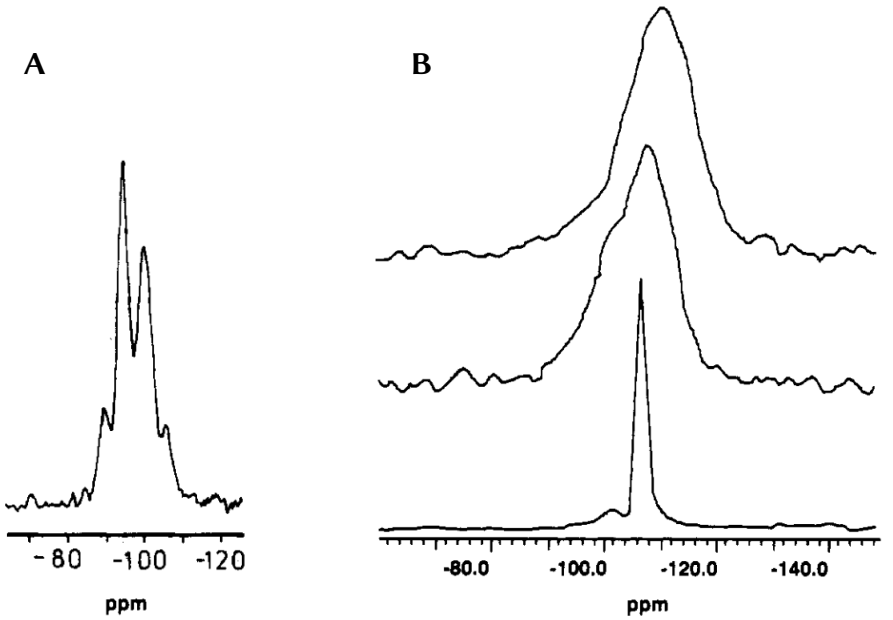

Figure 4.5: ^{29}Si spectra of zeolites and ASA to illustrate the different linewidth in crystalline and amorphous materials. A: NaY with Si/Al = 2.45, [177] Comparison between ^{29}Si spectra of ASA, MCM-41 and zeolite Y (top to bottom). [32] Note the different scales. Reprinted with permission from ref [177], Copyright 1981 John Wiley and Sons and from ref. [32], Copyright 1992 American Chemical Society.

4.3.1 *Pyridine*

Preferentially, pyridine is used in IR spectroscopy measurements to probe acid-site strengths as mentioned above (cf. Section 2.4). The proton signal of the material linked to perdeuterated pyridine occurs at 10 ppm in the case of silanols and shifts to 12 to 20 ppm on BAS due to protonation to PyH^+. The more complete the protonation, the lower the chemical shift. [93] In total, the chemical shift range with protons is relatively low, therefore, other nuclei are better suited to reach high resolution to distinguish different types of acid sites. [185] Measurements of the ^{15}N nucleus of isotopically enriched pyridine also reveal information about the bonding state to the surface of materials. The structure of siliceous MCM-41 was described in detail by a combination of low and room-temperature measurements corroborated by ^{1}H MAS NMR. Here, proton NMR revealed silanol goups that were not accessible by pyridine, because they are in small pores or within the wall. [186] It is to note, that at room temperature, exchange of the position of pyridine was observed. Therefore low temperature measurements are required for ^{15}N pyridine measurements. [183, 186]

4.3.2 *Acetone*

The ^{13}C nucleus of the carbonyl group of acetone is observed after its absorption on zeolites and silica-alumina materials. Because of the low natural abundance of ^{13}C, the carbonyl position needs to be isotopically enriched which makes this method rather expensive. Generally, the chemical shifts represent the strength of the underlying acid sites but acetone also tends to react with the latter. The reaction products also occur in the spectrum and should be addressed to avoid confusion. Moreover, the assignment of the type of acid site should be cross validated with other measurement methods. [183] Additional information about the size of a channel results from the line shape at room temperature which reports on the molecular motion on the BASs. [187]

4.3.3 *Ammonia*

Ammonia (NH_3) is a small molecule and therefore able to penetrate the small pores of zeolites. Its tremendous caveat is to form hydrogen bonds to NH_4^+ that were protonated by BASs which shifts the signals of NH_4^+ and hinders the proper determination of the acid strength. [99] To perform quantitative assessments of the acid sites, a vacuum treatment at elevated temperatures is necessary to remove the clusters formed on the acid sites. [183] Both the ^{1}H and ^{15}N chemical shift can be observed to acquire information about the acid sites. The proton chemical shift is especially suitable for materials with a low BAS concentration since the chemical shifts of NH_4^+ and NH_3 vary significantly. However, the chemical shift range of NH_4^+ is small, such that peaks would overlap at a higher concentration. The detection of LAS poses difficulties due to an equal chemical shift of BAS protons before and NH_3 protons after loading. Usually, difference spectra are used for peak assignment, but here, the two effects overlap. Despite the removal through outgassing of $^{15}NH_3$, the exchange rate between sites was so high that peaks merged to a large signal from which it was impossible to observe and assign specific sites. [67, 183]

4.3.4 *Deuterated acetonitrile*

Acetonitrile (CD_3CN) is capable of forming hydrogen bonds to surface acid sites after saturating the atmosphere. [93] However, it is a weak base and is therefore likely not to quantitatively cover the acid sites. Additionally, the probe may not cover all acid sites due to sterical hindrance at small pores, which prevents the necessary 1:1 stoichiometry for quantitative evaluation. [183, 188] Proton chemical shifts of the surface protons change from 4–5 ppm to 10.3–11.2 ppm upon impregnation with CD_3CN. The difference in the chemical shift

($\Delta\delta$) is assigned to the acidic strength. [188, 189] The ^{15}N chemical shift of $CH_3C^{15}N$ was also used to distinguish the strengths of the acid sites. [190]

4.3.5 *Phosphines*

Phosphines attach very well on the surface of silica-alumina materials and are able to reveal LASs and BASs as well as silanols via their ^{31}P chemical shift. Trimethylphosphine (TMP) is gaseous and extremely toxic which makes it difficult to work with. It is very sensitive to LAS where the signals spread over a wide chemical shift range. Signals of BASs, in contrast, are closer together. DFT calculations showed that charge-transfer complexes of BAS are only within a narrow range between -2 to -5 ppm, which is in accordance with experiments on zeolites and model compounds. [191] Therefore, it is not well suited to specifically investigate BAS. TMP easily oxidizes to TMPO in oxidative environments and even on oxygen donating materials in the absence of molecular oxygen. Generally, this is disadvantageous but can be used to quantify those oxidative sites. [183, 192] Different sizes of phosphines can be utilized to investigate the pore hierarchy and accessibility of the sites. [93, 183, 191, 193, 194]

4.3.6 *Phosphine oxides*

Trialkylphosphine oxides allow for a better assignment of LASs and BASs as well as physisorbed species, [195] however, the signals of LASs and BASs overlap with each other. Often, DFT calculations are used to support the chemical shift assignments [183] but they need to be well adapted to the investigated material. [196] Molecules with different alkyl chain lengths are used for the investigation of hierarchical pore structures as well. [85, 197] It should be noted, that T_1 of trioctylphosphine oxide (TOPO) is about 300 s. [183] Triphenylphosphine oxide (TPPO) was applied to zeolites to asses external BASs as the molecule is too bulky to enter the pores or to attach on LASs. [198] Overall, the use of phosphine oxides is an area where strict attention must be paid to systematic study design and rigorous verification of results on different materials in order to obtain reliable results. [183]

The most important method used in this work is the detection of acid centers by impregnation with TMPO. The following Section 4.4 is devoted to a detailed description of various aspects of the method.

4.4 TRIMETHYLPHOSPHINE OXIDE AS A PROBE MOLECULE

The probe molecule used in this work is a phosphine oxide. In addition to being easy to handle [199, 200] compared to the gaseous and toxic phosphines, it is particularly sensitive to BASs, which are of

particular interest for the dimerization of butene. Especially TMPO, first introduced as an NMR probe by BALTUSIS ET AL. [195] in 1986, has a widespread application for the acidity measurement of mesoporous materials and zeolites. Using TMPO, BASs and LASs have been characterized in a variety of materials such as ASA [201], γ-alumina, zeolite Y, USY [199] as well as on zeolites H-MFI, H-MOR and amorphous MCM-41. [191] Due to the polarizability of the P=O bond, the chemical shift of TMPO is linearly dependent on the proton affinity and thus, the acid strength [80] and allows the type of acid site and its strength to be deduced. [86, 194] This is possible for BASs and LASs. The ability to determine the concentration of acid sites with TMPO will be discussed in further detail below.

Among phosphine oxides, various homologues with different alkyl substituents are being used for acid site characterization depending on the targeted properties. The varieties with bulkier substituents (TOPO or TPPO) are used for exploring the surface of materials as they are often not able to penetrate the pores. [85, 197] With a kinetic diameter of ca. 0.55 nm, TMPO is the smallest variant and fits into a ten-membered ring of zeolites (average pore size of 0.6 nm). [194] The average pore size of the Al and Ga derivatives of MCM-41 is between 2 and 2.5 nm. [5, 202]

The chemical shift range for TMPO on acid sites spans between 50 and 98 ppm, allowing it to map subtle differences of acid strength. [194] The chemical shift is proportional to the deprotonation energy as shown in Figure 4.6. The assignment of the chemical shifts of LASs are more debated than those of BASs. The current consensus is that TMPO can also have chemical shifts of up to 85 ppm even though their bond to the LASs is so weak that it can be hydrolyzed by water. The LEWIS acid strength should therefore not be determined by TMPO. [76, 183] It is also to note that in zeolite ZSM-5, containing

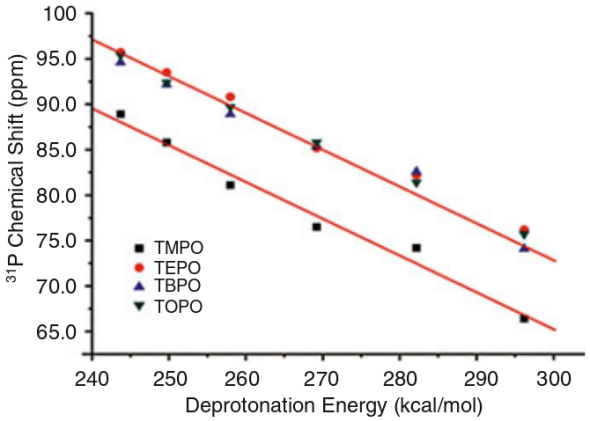

Figure 4.6: ^{31}P chemical shift of different alkylphosphine oxides vs. deprotonation energy of BASs. Adapted from ref. [203] with permission from Springer Nature.

twelve distinct Al centers, [204] TMPO acts as a strong base and removes the protons from the surface. Those $TMPOH^+$ molecules then occupy different positions in the channel system of the zeolite which gives rise to more ^{31}P signals than anticipated. [205] This is further discussed below in Section 4.4.3. Notwithstanding these observations, the value of studying materials with TMPO can be maintained if a well assessed loading strategy is followed and sufficient comparisons and control experiments are carried out. [183] The next sections discuss the different relevant aspects to consider for a reliable analysis of acid sites with TMPO.

4.4.1 *Impregnation methods*

There are various methods of impregnating the supports with TMPO. In most cases, the impregnation is conducted using the solvent dichloromethane (CH_2Cl_2) for distributing the probe uniformly on the surface.

It is to note that according to its kinetic diameter, TMPO alone is already strongly confined in micropores of zeolites sized of ~ 0.55 nm in ZSM-5 and generally < 2 nm. The larger pore size of mesoporous materials (2 to 50 nm [18]) does not allow for such close interactions with the pore walls but facilitates the evaporation of the solvent molecules.

Samples were prepared without contact to water and air using degassed and anhydrous solvents and substances in a glovebox. A known amount of TMPO was dissolved and added to the material. After evaporation of the solvent, the sealed vessel was treated at a temperature above the melting point of TMPO (413 K) at 483 K. [85, 87, 206] Variants of this method include a treatment with ultrasound [207] or prolonged agitation and solvent removal with vacuum only, without high temperature treatment afterwards. [199, 207]. N_2 flow can also be applied to remove the solvent. [193]

In 2009, Hayashi [208] introduced a solvent-free method for the impregnation. TMPO was placed in dessicator next to the sample and kept under static vacuum for one day. [208] The decision to move to a solvent-free impregnation was necessary because CH_2Cl_2 remains adsorbed to the material and cannot be completely removed. Solvent molecule attachment to BASs has been considered, but it alone cannot explain the strong adhesion which was also observed with other materials (ZSM-5, mordenite (MOR), zeolite beta and zeolite Y). Instead, the confinement in the pores keeps the solvent absorbed. [209] Different adaptations of the gas phase impregnation method have been developed. Freitas et al. [185] mixed TMPO directly with the substrate and distributed it by melting TMPO externally, while Bornes et al. [196] performed the melting inside a ssNMR rotor. The penetration depth of TMPO into micropores depends on the impregnation conditions: Heating the gas phase impregnated ZSM-5 to

373 K increased the TMPO uptake [210] compared to unheated MOR. [211] Two comparisons between gas-phase and solvent-based impregnation methods show small chemical shift differences in ^{1}H and ^{31}P spectra caused by residual solvent. Both investigate ZSM-5 but with different Si/Al ratios. HAYASHI ET AL. [212] also impregnated silica nanoparticles and mesoporous Folded Sheet Silica 16 (FSM-16). Both publications state, that only little of physisorbed TMPO is in form of crystallized substance as the rotational sidebands only have low intensity.

In a silicalite (ZSM-5 with low Al content), the spectra mainly differ in the signal between 29 to 33 ppm representing TMPO in micropores. [212] The shift therefore suggests different environments of TMPO due to the remaining solvent molecules. However, the difference in chemical shifts of physisorbed TMPO in silica nanoparticles or mesoporous silica FSM-16 compared between solvent and vapor impregnation was not significant ($\Delta\delta = 0.5$ and 1 ppm, respectively). In addition to that, BORNES ET AL. [213] proved the presence of the solvent as correlation peaks in heteronuclear correlation (HETCOR) spectra. However, solvent-free impregnation on microporous zeolite H-ZSM-5 came with the caveat of the enhanced formation of $(TMPO)_2H^+$ dimers, which in turn challenges the interpretation of the spectra.

Overall, one must carefully assess the use of preparation methods to determine surface acidity of silica-alumina materials. Both primarily applied methods bring inaccuracies with them that need to be considered during the evaluation of the results. The main points are:

- Avoid overloading with an excessive amount of TMPO in comparison to the number of acid sites. Residual molecules on the surface can form dimers that pose challenges during signal assignment.
- The number of $(TMPO)_2H^+$ dimers is lower with the solvent-based method, however, depending on the pore size, the solvent does not completely evaporate. Interactions between residual solvent and TMPO appear as additional signals in the ^{31}P spectrum.
- Solvent-free impregnation obviates solvent interactions, but the number of $(TMPO)_2H^+$ is higher due to imperfect distribution of TMPO on the material's surface. This causes more TMPO molecules to be in proximity to each other, which dimerize. [183, 213]

4.4.2 *Distinction between BAS and LAS*

Early assumptions that BASs generally possess higher chemical shifts in ^{31}P spectra [86, 191] have been proven wrong [87, 183, 214]

On the other hand, proton chemical shifts of BASs directly correlate with their bond strength. More deshielded protons appear at lower fields and indicate stronger BAS. This can be used to assign the type of acid site with the help of 2D $^{31}P\{^{1}H\}$-HETCOR spectra. [215] However, reliable assignments require the formation of 1:1 TMPO:BAS complexes.

A more distinct way of discrimination between LASs and BASs is to tailor the different type of bond of LASs and BASs. The differentiation between LASs and BASs is possible by exposing the TMPO impregnated samples to humidity. Signals belonging to LASs vanish since the interaction between LAS and phosphine oxides is weak. [214] There are different protocols for the hydration: Wiper et al. [214] hydrate their H-[B]-ZSM-5 samples for 2.5 h in an undetermined atmosphere and Rakiewicz et al. [199] use a controlled atmosphere of 20 % relative humidity for 2 h and a saturated atmosphere for 1 h. Because LAS consist of a tricoordinated Al site (see Figure 2.1), they form weak BASs upon exposure with water. This is the case even if the site is covered by a phosphine oxide molecule. On the other hand, there is nearly no dissociation of the strong hydrogen bond between a BAS and phosphine oxide caused by the strong hydrogen bonds in TMPO···H. [194] This selectively quenches the LASs signals. [207, 214] However, also superacid BASs at a ^{31}P chemical shift of 85 to 88 ppm vanish upon exposure with humidity. [87, 216] Instead of the vanished signals, now the signal at 53 ppm represents the dissolved TMPO in water at pH values between seven and one. If only a small amount of water is linking the TMPO molecules with each other, the signal is shifting 12 to 14 ppm downfield to approximately 41 ppm. Depending on the proticity of the solvent, the chemical shift for the similar triethylphosphine oxide (TEPO) ranges between 42 and 65 ppm. [217] By using deuter-

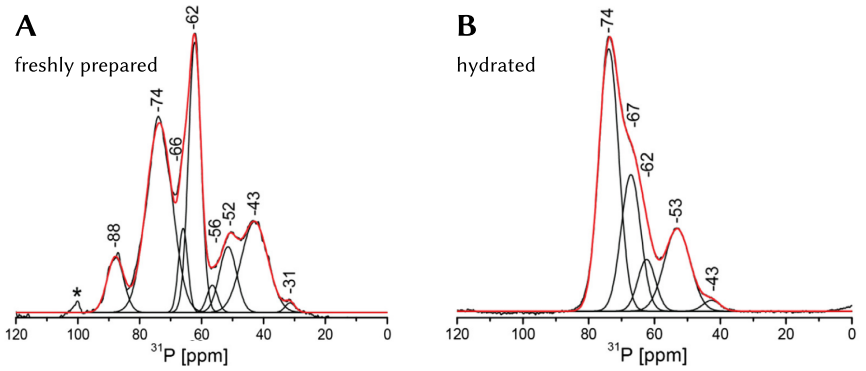

Figure 4.7: ^{1}H-decoupled ^{31}P MAS NMR spectra of TMPO-treated dehydrated borosilicate zeolite HAMS-1B (A) and its corresponding profile after exposure to humidity for 2.5 h (B). The asterisk denotes a spinning sideband. Adapted from ref. [214]. Copyright 2014, with permission from Elsevier.

ated TMPO, BASs can be identified through the $^{1}H-^{31}P$ coupling

probed by CP. Signals of protons close to phosphorus nuclei are enhanced in comparison to direct polarization (DP), revealing the close proximity in Zeolite Y (FAUJASITE structure). [218] Recoupling experiments like rotational echo double resonance (REDOR) and transfer of populations *via* double resonance (TRAPDOR) are also used to probe the internuclear distance from ^{31}P to ^{27}Al and ^{1}H of the acid sites, however, the precise distances cannot be obtained at room temperature due to the molecular motion of the TMPO molecules. Three BASs are detected at 65, 55 and 40 ppm, representing three distinct BAS positions in the structure, two being bridging Al–O–Si sites and one being a weakly acidic silanol group. [218]

4.4.3 *The issue of dimer formation with TMPO*

The amount of TMPO on the surface depends on the number and the desired coverage of acid sites. YI ET AL. [216] recommend a full coverage of all acid and other protic sites with TMPO with a total loading of 120 % (wt/wt). This number is regardless of the actual amount of acid sites but the authors also suggest to adapt the amount to the number of acid sites as calculated from the number of Al atoms in the zeolite. However, for zeolite ZSM-5, BORNES ET AL. [205] demonstrated that even a P/T = 0.75 loading may form 2:1 TMPO:acid site complexes, compromising both qualitative and quantitative analysis. To better control the amount of non-acid-site-bound TMPO, the loading should be based on the estimated number of acid centers. This limitation becomes critical as excess TMPO deposition distorts the results. Increasing the TMPO loading not only intensifies the signal of physisorbed TMPO but also amplifies the BAS signal at 64 ppm. Given that the number of acid sites does not change with varying amounts of TMPO loading, this is an artifact of the method. [205] With the help of *ab initio* molecular dynamics (AIMD) based calculations, this can be assigned to protonated TMPO ($TMPOH^+$) confined in ten-membered ring sinusoidal channels of a zeolite ZSM-5. At the same time, evidence of the formation of $(TMPO)_2H^+$ dimers was provided by the calculations. Unfortunately, these centers cannot be easily distinguished by NMR since the signals of monomers and dimers occur at the same chemical shift in a 2D ^{1}H–^{31}P HETCOR spectrum (see Table 4.2 and Figure 4.8) [196] The formation of dimers was already shown previously [196, 219] but is not often taken into consideration in further studies. Depending on the sample system, the preparation and pretreatment (baking) conditions have to be carefully considered.

In zeolites (e.g MOR [80]), with their narrow channels and three BASs per unit cell, one TMPO molecule can interact with every site. In such a case, VAN DER WAALS interactions arise between two TMPO molecules and thus, the chemical shifts of both change, one shifts downfield, the other upfield. [80]

Table 4.2: Chemical shifts of mono- and dimer complexes of TMPO on acid sites of the zeolite ZSM-5. Values taken from ref. [196].

Complex	δ^{31}P / ppm	δ^{1}H / ppm
TMPO···ZH	49.6–53.5	14.7–17.1
$TMPOH^+\cdots Z^-$	75.6–84.8	10.6–15.5
$(TMPO)_2H^+\cdots Z^-$	47.3–51.8	14.3–15.2
	74.7–79.0	

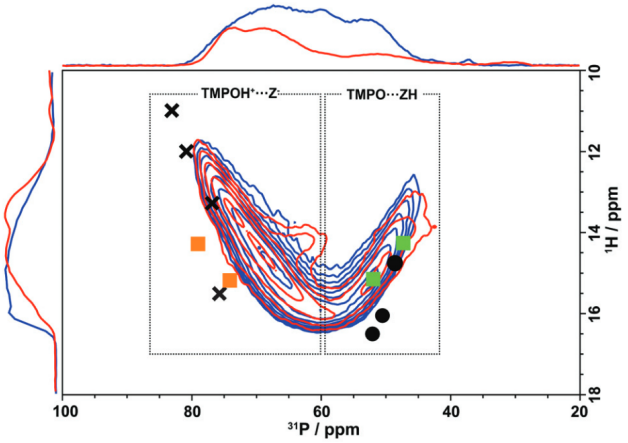

Figure 4.8: Superposition of $^{1}H-^{31}P$ HETCOR NMR spectra of HZSM-5 (blue) and HZSM-5 steamed at 500 °C (red) depicting the calculated (δ_H, δ_P) pairs extracted from TMPO···ZH (•), right dashed rectangle, $TMPOH^+\cdots Z^-$ ion pair (X), left dashed rectangle, and $(TMPO)_2H^+\cdots Z^-$ ion pair (orange/green □) models. Adapted with permission from ref. [196].

Those proximities and correlations were investigated with $^{1}H-^{31}P$-HETCOR and 2D $^{31}P-^{31}P$ DQ-SQ NMR experiments where the interactions between ^{1}H and ^{31}P or two ^{31}P nuclei are observed. The presence of 1:1 TMPO:BAS complexes is indicated by an (inverse) linear correlation between proton and phosphorus chemical shifts, as demonstrated in Figure 4.9 (a and b). [215]

HETCOR spectra show a curved (or "inverse parabolic") structure which can represent protonated TMPO confined in channels as well as $(TMPO)_2H^+$ dimers. To elucidate the underlying structure, those spectra necessarily need to be checked for other possibilities of interpretation. DQ-SQ correlations are more difficult to observe spectroscopically since the intrinsic sensitivity is low. To obtain well-resolved spectra, long acquisition times are necessary. At low loading, the absence of the signal in a DQ-filtered 1D spectrum does not necessarily indicate the absence of dimers. The low amount of TMPO and the low

excitation efficiency may also be contributing factors. [205, 215] At high loading of P/T = 0.75 in a double quantum filtering experiment, typical signatures of 1:1 and 1:2 complexes were observed. The signals from 1:1 complexes stem from TMPO molecules in proximity to each other in the channels of the zeolite. The $^{1}H-^{31}P$-HETCOR spectrum of H-ZSM-5 loaded with P/T = 0.4 TMPO (Figure 4.9, b) shows autocorrelations between TMPO molecules bound to LASs but not between those bound to BASs. This indicates that LASs cluster together while BASs remain spatially separated. The relationship between two TMPO molecules bound to the same BAS is evidenced at P/T = 1.0 by two observations: cross-correlations in DQ-SQ spectra between signals at 68 and 52 ppm in the ^{31}P dimension, and correlations to identical proton sites in the HETCOR spectrum (Figure 4.9, c). [215] No HETCOR spectra of TMPO-impregnated MCM-41 have been published to our knowledge.

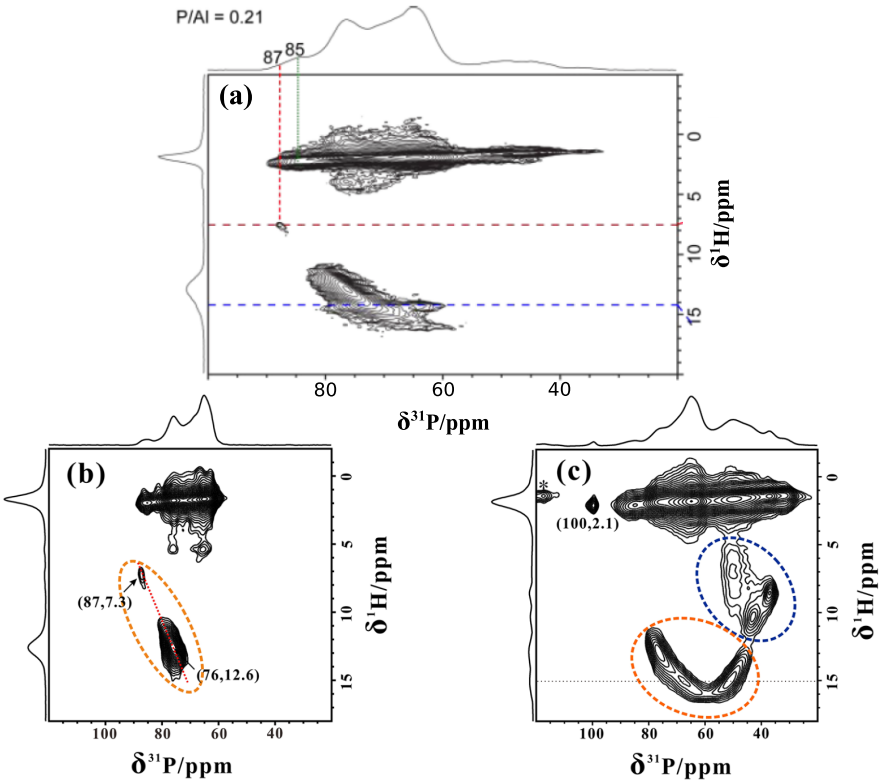

Figure 4.9: 2D $^{1}H-^{31}P$ CP HETCOR NMR spectra of H-ZSM-5 zeolites with different TMPO loadings: (a) P/Al = 0.21 [205], (b) P/Al = 0.4, and (c) P/Al = 1.0. [215] The red circle represents TMPO bound to BASs in (b) and (c), and the blue circle represents physisorbed species. Note their different scales, for details see the text, Subfigure (a) was adapted with permission from ref. [205]. Copyright 2021 American Chemical Society. Subfigures (b) and (c) were adapted with permission from ref. [215]. Copyright 2021 American Chemical Society.

4.4.4 *Quantification with TMPO?*

The formation of TMPO:BAS complexes with a ratio higher than 1:1 inevitably leads to an overestimation of the number of acidic sites, especially when only observing 1D spectra. [196] Therefore, it needs to be ensured, that only a single TMPO molecule is adsorbed on an acid site as explained above.

Assuming no dimers were formed after impregnation, Zasukhin et al. [220] analyzed the factors that need to be considered for a reliable quantification during sample preparation, measurement and analysis. They assessed different internal and external standards for their suitability. The internal standard $AlPO_4$ tridymite is more reliable in comparison to an external standard but can only be used if there are no interactions with the adsorbed TMPO probe molecule. Additionally, its long relaxation time (450 s) immensely lengthens the measurement time. While external standards such as $(NH_4)_2HPO_4$ and GaP, which are consecutively measured in different rotors, are more straightforward to use, although changes in the probe tuning and matching upon sample exchange can introduce inaccuracies.

If this method of impregnation with TMPO is to be used for absolute quantification of acid sites, it is essential to anticipate the potential for error. A recent study indicates that the error was reduced below 10 % through the optimization of preparation and acquisition. The main remaining error sources are the procedures of baseline and phase correction of the obtained NMR spectra. Therefore, if values with lower errors are given, the characterization should be treated with considerable caution. [183, 220]

4.4.5 *Literature values for acidity measurements of (Al-)MCM-41 with TMPO*

The examples of acid site characterization of Al-MCM-41 materials presented in literature show the highest chemical shift at 69 ppm mostly combined with a signal at 64 to 66 ppm which is also attributed to a BAS. All values, their assignments and the references are given in Table 4.3.

4.5 PARAMAGNETIC NMR ON $Ni(Cp)_2$ AND NI-IMPREGNATED CATALYSTS

While paramagnetic NMR presents certain challenges, it also offers valuable insights into the electronic structure of components of interest. This section will focus on NMR involving $Ni(Cp)_2$ and Ni-containing silica-alumina materials commonly used in catalysis.

First measurements of $Ni(Cp)_2$ in solid and solution were published in 1957. An explanation for the high-field shift in contrast to the ex-

Table 4.3: Chemical shifts of MCM-41 materials found in the literature.

Support Type	BAS	LAS	Other	Reference
H-MCM-41	68.5, 56.7	–	45.7 (silanol) and 40.5 ppm (physisorbed)	[85]
H-MCM-41, Si/Al = 16	69, 64	55	45.7 and 43 (physisorbed)	[221], referenced by [194]
MCM-41, Si/Al = 70	69 & 64 ppm, not annotated		48 ppm	[207]
Al-MCM-41, Si/Al = 18	66 on weak BAS		45 ppm (physisorbed)	[222]
MCM-41	56.7, 64, 68.5, 69	–	45.7 (silanol), 39, 40.3, 48 (physisorbed)	[191] references [207] and [85]

pected lowfield shift is the delocalization of the unpaired electrons of the cyclopentadienyl-rings and the $\sigma - \pi$ configuration interactions of the orbitals. [223] This was further confirmed and offered a basis for the refinement of molecular orbital calculations. [224, 225] The proton chemical shifts in metallocene compounds show an interesting pattern. Vanadocene and chromocene exhibit negative proton chemical shifts, while manganocene, cobaltocene, and nickelocene display positive chemical shifts. This represents an inverse relationship between these two groups of metallocenes in terms of their NMR behavior. [226, 227] In an MAS NMR experiment, the ^{1}H chemical shift of $Ni(Cp)_2$ was found to be strongly temperature-dependent and therefore, MAS frequency-dependent. The temperature normalized proton chemical shift is -257 ppm. [228] Information about the geometric structure were obtained from the isotropic chemical shift. The electronic structure was investigated by a Herzfeld-Berger analysis of the sidebands of the ^{13}C spectra and e.g. subsequent calculation of the electron population in the Cp ligands. [228]

The chemical shift origins in the interaction between the electron's g-tensor $\boldsymbol{g}$, its zero-field splitting tensor $\boldsymbol{Z}$ and its hyperfine interaction tensor $\boldsymbol{A}$ in form of their cross-terms. This expression can be split into nine terms, four terms each are a contact shift and a pseudo-contact shift and the last one is a orbital shift. The full deduction is presented by Pell et al. [143]. In the end, the only relevant contributions to ^{1}H and ^{13}C chemical shifts are the orbital and non-relativistic Fermi contact terms, while spin-orbit-coupling, g-factor, zero-field splitting and the hyperfine interaction are negligibly small. The two unpaired electrons in $Ni(Cp)_2$ and the two main contributions of the chemical shift – the back-donation of β spin density from the ligand to the metal d_σ orbital and the contributions from non-nearest-neighbor σ orbitals in the Cp ring [143, 229] – enhance each other, inducing such a large chemical shift in comparison to other metallocenes. [143]

On silica crystals, $Ni(Cp)_2$ adsorbs in monolayers and moves in a "tumbleweed" reorientation motion where it stays connected to the surface but changes from edge-on coordination to face-on coordination. This was found by using wideline and static ssNMR spectroscopy. [230] A ^{1}H NMR study of a Mo and Ni coated ASAs, different proton signals could be distinguished by the proton signals of the OH groups of SiOH and AlOH. They are at typical proton chemical shifts of 1.7 and 2.2 ppm. Upon impregnation with Mo and Ni and subsequent calcination, the signal at 2.2 ppm decreases the most, indicating a preferential attachment of Mo and Ni to the AlOH groups. In this study, other regions of the spectrum are not considered. [231]

^{29}Si NMR of microporous silica-alumina materials with incorporated NiO presented different spinning sideband patterns that give hints about the incorporation of a paramagnetic agent into the structure. However, the intensity of the sideband patterns is not strongly

dependent on the amount of Ni within the material but the amount of paramagnetism. At a high loading with Ni, the sideband intensity became lower due to clustering of Ni to form Ni^0 nanoparticles which are ferromagnetic at room temperature. [180]

On the other hand, since the Si signals are at the same chemical shift as without incorporated Ni, the paramagnetic centers are relatively remote from the observed nuclei. In case of a close contact of NMR active nuclei with paramagnetic agents, the NMR signal of those nuclei is broadened and at a different chemical shift. Those wide lines can normally be observed with HAHN-Echo experiments. [180]

In summary, paramagnetic NMR is a powerful technique but is not commonly used in catalysis research since it is not simple to set up and evaluate. Most ^{1}H-NMR studies in literature have focused on the the "normal", diamagnetic ^{1}H chemical shift region and the decrease of surface proton signals, missing the opportunities to study the region of the paramagnetically shifted signals, if they are present. The studies reviewed in this section examined only Ni-containing materials and did not investigate samples immediately after solvent-based impregnation.

Part II

MATERIALS AND METHODS

5 SAMPLE PREPARATION

Support materials were prepared in a hydrothermal synthesis. After synthesis, they were used for the preparation of the samples involved in the NMR measurements. All support materials are listed in Table A.1. Four compositions of supports exist: Al- and Ga-doped MCM-41 with Si/T ratios of 10 and 20. Those four support materials have been further treated (e.g. re-calcined or deuterated) and were impregnated with Ni and TMPO to assess the properties of the catalyst and the surface acidity, respectively. Other support materials were used as well to compare the spectra obtained using those methods with the spectra in literature.

5.1 PREPARATION OF MCM-41 SUPPORT MATERIALS

Typically, 3 g silicic acid (product name: precipitated extra pure light DAB) and 75 g tetramethylammonium hydroxide solution (10 %) were blended under continuous stirring at room temperature overnight. The desired amount of dopant precursor solutions ($Al(NO_3)_3$, $Ga(NO_3)_3$) were added dropwise under continuous stirring to establish molar ratios of Si/T^{3+} (T = Al, Ga) of 20 or 10. Then 6 g of stearyltrimethylammonium bromide was added to this solution in small portions. This suspension was stirred at 60 °C for 24 h to get a clear and homogeneous solution. To adjust pH = 5, suitable amount of acetic acid (25 wt%) was added into the clear solution. After 1 h stirring at 60 °C, the obtained white solid product was filtered off and washed several times. [5, 110] After overnight drying at ambient conditions, samples were either dried in an oven at 100 °C or kept at air and ambient conditions until the filter cake had undergone sufficient desiccation to crumble and the majority of the water had evaporated. The sample was sieved (500 µm) and then calcined (heat to 550 °C in 10 h, keep 6 h, cooling down). After calcination, the elemental composition was determined; the ratios are listed in Table A.1. The synthesized metal-doped MCM-41 samples are named according to the dopant element followed by M10 or M20, where the number (10 or 20) represents the calculated silicon to heteroatom (Si/T) ratio. For example, aluminum-doped MCM-41 with a Si/T ratio of 10 would be labeled as Al-M10. Prior to inserting the samples into the glovebox, a part of them was re-calcined (2 K/min to 400 °C, keep for 2 h, cool down at 20 K/min to room temperature under flowing Ar or synthetic air) and promptly given in either a SCHLENK-tube or a glass vial. The SCHLENK-tube was repeatedly evacuated and filled with Ar three times, the glass vials

were opened in the antechamber of the glovebox for exchanging the atmosphere. All supports were stored there until further treatment.

It is to note, however, that during the time in air, despite the effort to shorten this time as much as possible, humidity and other substances from the laboratory atmosphere were adsorbed on the surface. Possibly, BASs that were removed during the recalcination were reintroduced by the humidity. But since this catalyst was used for the catalytic experiments in which it was showing activity, it was also considered as the relevant material of interest.

DEUTERATION Deuteration of the material was carried out by adding ~4.5 mL of D_2O to ~0.3 g support material. The mixture was stirred and stored overnight at room temperature. D_2O was removed through heating in a water bath or storing the vials in a dry oven. In some cases, the support material was baked together, resulting in a less voluminous powder than that observed previously.

USY The zeolite ultra-stabilized zeolite Y (USY) was selected as comparison to MCM-41 materials. For simplicity, a material with large pores and a low amount of different Al sites was chosen to avoid complexity, especially after TMPO impregnation. USY of the FAU-type [232] possesses pores with a relatively large diameter. A sphere with a diameter of 1.12 nm can be included and a sphere with a diameter of 0.74 nm can diffuse within the pores. The structure is based on sodalite cages that are connected via hexagonal prisms forming a supercage. [233] USY possesses only one framework Al site and has a Si/Al ratio of 2.6. USY-NH_4 (CBV 300, Zeolyst International) was calcined (2 K/min to 150 °C, held for 30 min, 5 K/min to 600 °C, held for 4 h then cooled to room temperature at 20 K/min) in synthetic air. The material was transferred to a glovebox after repeated vacuum-argon cycles. The elemental composition analysis was used to determine the amount of TMPO needed to achieve a P/Al ratio of 0.6.

SILICALITE The zeolite silicalite-1 (S1) is of a MFI structure and has pores that can accommodate molecules with a kinetic diameter of 0.6 nm. [204, 234, 235] It was kindly provided by Dr. Dan Zhao. The material was heated under inert gas to remove the sorbents. The material was then introduced into a glovebox prior to impregnating it with TMPO by **method 1** (see below). An amount of 0.5 mmol g^{-1} TMPO was used.

5.2 IMPREGNATION WITH TMPO

All relevant samples are listed in Table A.2.

TMPO was purchased from ALFA AESAR and three batches were used: 1) Directly after opening the bottle, the substance was introduced

into a SCHLENK tube, evacuated and purged with Ar several times and introduced into the glovebox. 2) and 3) After purging, the substance was heated above the melting point and evacuated to remove the water which was taken up in the mean time.

Three impregnation methods were applied in this work.

METHOD 1: SOLVENT-BASED IMPREGNATION (CONVENTIONAL) TMPO is impregnated on the supports by dissolving it in CH_2Cl_2 under inert atmosphere ($c(H_2O) < 3$ ppm). The solvent is removed under vacuum and the sample is subsequently heated to 160 °C for 45 min (mp. TMPO = 140 to 141 °C) to evenly distribute the probe molecule on the surface.

METHOD 2: SOLVENT-FREE IMPREGNATION WITH DEHYDRATION (AVEIRO) The impregnation procedure on a similar or the same setup was described by BORNES ET AL. [196] and is shown in Figure 5.1. The support material was filled into a rotor and dehydrated in vacuum for 15 to 20 h at 300 °C and under vacuum ($4.6 \cdot 10^{-3}$ hPa) in the mentioned vacuum line. [236] Subsequently, the rotor-containing compartment of the vacuum line was closed with a stopper, disconnected from the line and inserted into a glovebox. TMPO was added under protective atmosphere. The rotor was subsequently sealed with an O-ring Vespel cap and re-inserted into the vacuum line compartment, removed from the glovebox and heated to 150 °C for 4 h.

Figure 5.1: Specialized vacuum line providing the possibility to seal a rotor under protective atmosphere. Left: Full line; Right: Rotor containing compartment.

METHOD 3: SOLVENT-FREE IMPREGNATION (ROSTOCK) The support was filled into a SCHLENK tube under protective atmosphere together with TMPO. The TMPO was not previously ground and was therefore partly present in larger crystals which might have hindered homogeneous distribution on the material's surface. In the same atmosphere, the tubes were heated to 160 °C for 45 min and carefully

shaken from time to time. After cooling, the impregnated materials were filled in the NMR rotors and sealed, again in inert atmosphere. The sealing was tight, that after several months, no alterations in the spectra by intrusion of water were observed. This is in line with the findings from ref. [237]

5.3 HYDRATION

Samples of the series of **method 1** were removed from their rotors, given separately into crystallizing dishes and stored in a desiccator with distilled water. A humidity of 96 % was achieved. After 10 days, samples were refilled in their rotors and sealed.

Samples prepared by **method 2** were exposed to 75 % humidity by storing the uncapped rotors for 48 h in a desiccator with saturated NaCl solution, before resealing.

5.4 IMPREGNATION WITH NICKELOCENE

All four supports were impregnated with $Ni(Cp)_2$ in an inert nitrogen atmosphere by dissolving the desired amount of $Ni(Cp)_2$ in pentane and vigorously stirring the solution. The support material was added immediately after the solution turned green. The resulting brown suspension was stirred continuously until all pentane had evaporated. The sample was packed into a rotor and sealed within the glovebox, and stored under protective atmosphere until measurement.

5.5 CO-IMPREGNATION WITH NI AND TMPO

The impregnation with Ni and with TMPO were combined. First, by impregnation with $Ni(Cp)_2$, the active catalyst is prepared. To investigate the remaining acid sites, TMPO was added on top to attach onto the acid sites. In the first step, 50 mg of each support was treated with $Ni(Cp)_2$ (1 mg) dissolved in pentane within an inert atmosphere. The solvent was evaporated under ambient, inert conditions. The catalyst was filled into a SCHLENK tube followed by the impregnation with TMPO and CH_2Cl_2 according to **method 1**. To remove the solvent, three methods were tested:

1. Evaporation of solvent CH_2Cl_2 by flowing Ar through the SCHLENK tube. The stopper was slightly open under positive Ar pressure to allow for a flow.

2. Purging between vacuum and Argon until the solvent had evaporated

3. Usual procedure for the solvent-based TMPO impregnation with evaporation of the solvent by applying vacuum and heating the sample to 165 °C.

The colors of the impregnated samples were different: the batches prepared without heating had a green color, while the third batch was brownish after the heating treatment. This indicates, that Ni changed its oxidation state from +II to +I or 0 since the green color is characteristic for solvent coordinated Ni^{2+}. [238] Proton NMR signals of CH_2Cl_2 are strongest for the samples of the first method, therefore, the second method was chosen for the following experiments. The results are detailed in Section 11.6.

6 NMR EXPERIMENTS

Solid state NMR experiments were performed on a Bruker AVANCE III HD spectrometer with a 9.4 T Bruker Ascend DNP widebore magnet operating at 400.5 MHz proton frequency. All experiments were performed at room temperature unless otherwise stated.

Two probes were used: A 4 mm MAS WVT H/X/Y probe and a 1.3 mm MAS H/X CP broadband probe.

6.1 DIRECT MAS-NMR MEASUREMENTS ON ^{1}H, ^{27}AL AND ^{29}SI NUCLEI

Direct measurements on ^{1}H, ^{27}Al and ^{29}Si nuclei were performed in the 4 mm probe which was configured in X/H double mode without rangecoil but in $\lambda/4$ mode for ^{29}Si and in $\lambda/2$ mode for ^{27}Al. The proton channel is not affected by the λ setting.

^{27}Al pulses were optimized on Al-M20 at a low pulse angle with a pulse length of 2 µs and a pulse power of 30 W. A spinning frequency of 4 kHz was employed. The measurements were referenced to the lowfield signal of adamantane at 37.77 ppm after conversion from the ^{13}C to the ^{27}Al scale.

^{29}Si MAS-NMR experiments were conducted at a MAS rate of 15 kHz and a pulse length of 4 µs at 80 W (below 90 deg) and a repetition time of 60 s. Pulses were optimized afterwards on Q_8M_8 (Octakis(trimethylsiloxy)silsesquioxane, $Si[(CH_3)_3]_8Si_8O_{20}$) to yield a 90° pulse at 4.5 µs at 130 W. The repetition time was 10 s. For the optimization on Q_8M_8, the repetition time can be shorter than for quantitative measurements on ASA.

Proton measurements were usually conducted using DP or a HAHN-echo sequence with a 3 µs 90° pulse at 64 W and were referenced to the proton pulse of adamantane at 1.8 ppm.

6.2 ^{1}H MEASUREMENTS OF NI-IMPREGNATED SAMPLES

For the detection of ^{1}H-NMR spectra on paramagnetic samples, samples were prepared in a 1.3 mm rotor. The Ni content was sufficiently low to not disrupt MAS rotation. A rotor-synchronized HAHN-Echo sequence was used to suppress the proton background of the probe. Typically, the MAS frequency was 20 kHz. The acquisition could be performed very rapidly, because the signals shifted far upfield (< 0 ppm) are relaxing very fast. The number of scans could be increased to typically 4096 for an improved signal-to-noise ratio (SNR). This was

possible by using a rapid repetition rate. The parameter for the recycle delay between two experiments, was set to its minimum value of 50 ns such that the acquisition time practically serves as the experimental delay. Usually, the acquisition time was set to 1 ms.

6.3 ^{31}P SPECTRA AFTER IMPREGNATION WITH TMPO

All measurements were referenced to the signal of $NH_4H_2PO_4$ at a ^{31}P chemical shift of 1.33 ppm.

1D DP CHARACTERIZATION EXPERIMENTS The 4 mm MAS WVT H/X/Y probe was used, which was configured in X/H double mode with an inserted rangecoil to reach the frequency of ^{31}P (162.1 MHz) on the X-channel. All experiments were performed at room temperature. All characterization experiments were performed using a simple BLOCH decay (DP) experiment. The pulse parameters were optimized until sufficient SNR was obtained, usually a length of 3.57 µs and power of 85 W was used.

HETCOR Prior to HETCOR experiments, the parameters were optimized on a CP experiment. [147, 148] They were usually acquired with a HARTMANN-HAHN matching frequency of 50 kHz, a contact time of 4500 µs and a ramp between 70 and 100 %.

7 SOFTWARE TOOLS FOR NMR ANALYSIS

7.1 TOPSPIN

Acquisition of NMR data was done with TopSpin 3.5pl6 while data processing was performed with TopSpin 4.1.4 and 4.4.0. Usually, the length of the FID was cropped to a position at which the signal was decayed to avoid accumulation of noise. The standard procedure involved exponential multiplication, FOURIER transform and automatic or manual phase correction, if necessary. Measurements were referenced externally using appropriate standard samples (cf. Appendix D). The processed data were visualized with NMRAspecds (*vide infra*).

7.2 NMRASPECDS

NMRAspecds (version 0.2.0) was used for processing and visualization of NMR data.

The Python package NMRAspecds [239] was written in the course of this thesis. It presents a simple and reproducible way to analyze and plot NMR spectra without the need to write code. The NMRAspecds package is based on the ASpecD framework [240, 241] for handling spectroscopic data focusing on reproducibility. Its core is the model of a dataset which contains (numerical) data and metadata. The dataset here is agnostic on the form or file format of the raw data. Processing and analysis steps are performed on a dataset with the dataset remembering all important parameters in its history.

The software uses YAML-formatted recipe files that specify datasets and their processing tasks in a human- and machine-readable format. When "served" via terminal to the "Chef de cuisine", it executes all processing steps and automatically saves the resulting figures, reports, and a history file. This history preserves reproducibility by recording timestamps, software versions, and all processing parameters. The recipe-driven approach enables automated, non-interactive data analysis, with the history output formatted as a new recipe.

The implementation of NMRAspecds involves a model for the metadata to define the dataset, an importer factory to choose the correct importer, importers for data and metadata from the original file format and NMR-typical processing and analysis steps (external chemical shift referencing, normalization to the number of scans). Other processing and analysis steps which are not specific for NMR are available through the underlying ASpecD framework without further specification. A specialized importer and a plotter for data fitted with Dmfit

(*vide infra*) was written to create standardized figures containing additional information such as the maximum of the signals.

The package is written object-oriented and was developed test-first to ensure correct behavior at the time of development and later upon extension and refactoring. The testing process is automated using the Python unit testing framework. Code consistency is improved using an automatic code formatter, Black, together with Prospector for static code analysis. The documentation is incorporated into the code itself, and additional concepts and examples of usage are documented alongside the code. The automated documentation formatting tool, Sphinx, transforms the documentation into HTML pages, which are available online on `https://docs.nmraspecds.de`.

The software is released under a permissive license (BSD 2-Clause) and is available for convenient installation from the Python Packaging Index (PyPI). The source code can be obtained from the widely-used code exchange platform GitHub and is also published on Zenodo, which offers enhanced possibilities for citations due to the inclusion of a Digital Object Identifier (DOI).

An example recipe is provided in Listing 7.1, an original recipe for comparing raw and fitted data is given in the appendix (Listing E.1). Most figures in this thesis were produced with NMRAspecds and used with only minor modifications.

Listing 7.1: Example recipe for the processing of NMR data including a normalization to the number of scans and separate plots of each dataset.

```
format:
  type: ASpecD recipe
  version: '0.3'

settings:
  default_package: nmraspecds

datasets:
  - /path/to/first/dataset
  - /path/to/second/dataset

tasks:
  - kind: processing
    type: Normalisation
    parameters:
      properties:
        kind: scan_number
  - kind: singleplot
    type: SinglePlotter1D
    properties:
      filename:
        - first_dataset.pdf
        - second_dataset.pdf
```

7.3 FITTING

Signals were fit with Dmfit (V. #20230120) [242] by using a deconvolution into signals with simple GAUSSian and LORENTZian lineshape parameters (half-width at half-maximum). Variable parameters were position, amplitude, linewidth and GAUSS-to-LORENTZ ratio $xG/(1-x)L$. The signals were decomposed into a variable number of signals, in which all parameters were set variable. The fitting procedure was repeated until the sum of signals matched the spectrum visually well. Signals were given starting parameters that made physical sense and were in line with literature and previously obtained results.

Fitting of CSA-parameters were conducted using the Python program ssNake (V. 1.4) [243] by using the previously processed data.

Part III

RESULTS AND DISCUSSION

8

STARTING POINT: SUPPORT CHARACTERIZATION AND CATALYTIC TESTS

This chapter presents a summary of a yet unpublished manuscript by Vuong et al. [5] which is the basis for the research described in the following chapters of this thesis. The experiments in this chapter and analyses were performed by Dr. Huyen Vuong, Christine Rautenberg and Dr. Christoph Kubis.

Differently doped MCM-41 based materials were investigated after Ni impregnation for their activity and selectivity of performing the butene dimerization. Additionally, the supports were characterized in detail by various methods. T-MCM-41 materials were prepared with T = Al, Ga, B, In in different Si/T ratios of 10 and 20. The ratios represent the ratios that were originally used for synthesis. Only Ga and Al containing materials are described here since the B was not efficiently incorporated into the lattice and only a very small amount of acid sites could be observed with In.

The number of acid centers was determined by Pyr-IR and NH_3-TPD. All values are summarized in Table 8.1. The determination by Pyr-IR yields the number of acid sites through integration of the characteristic bands at 1544 cm^{-1} (BAS) and 1455 or 1458 cm^{-1} (LAS). However, their strength cannot be reliably determined although it can be estimated from slight shifts in the wavenumber. The number of BASs is considerably lower in both Ga-MCM-41 samples than in Al-MCM-41 samples. At the same time, the amount of LASs is practically identical in the T-M10 supports, while it is lower in Al-M20 than in Ga-M20. The distribution of acid sites strengths was extracted from NH_3-TPD desorption profiles (cf. Figure 8.1), but a differentiation between BASs and LASs is not possible. The NH_3-TPD analysis revealed three distinct peaks[1], indicating at least three acid sites of varying strengths. The amount of desorbed NH_3 allows for an estimation of the number of acid sites. T-M10 materials have a higher content of T^{3+} ions and showed a greater number of acid sites compared to T-M20 materials. Interestingly, the amount of desorption differed between the two material types: In T-M10 supports, the desorption amount followed the order: Ga > Al while in T-M20 supports, the desorption amount was inverse: Al > Ga. The Ga-containing materials demonstrated higher desorption at elevated temperatures, indicating a higher concentration of the strong type of acid centers. However, the strength of this acid site is assessed from their temperature maximum. The Al-doped samples

1 The *l*-signal was not considered as an artifact here (cf. Section 2.4).

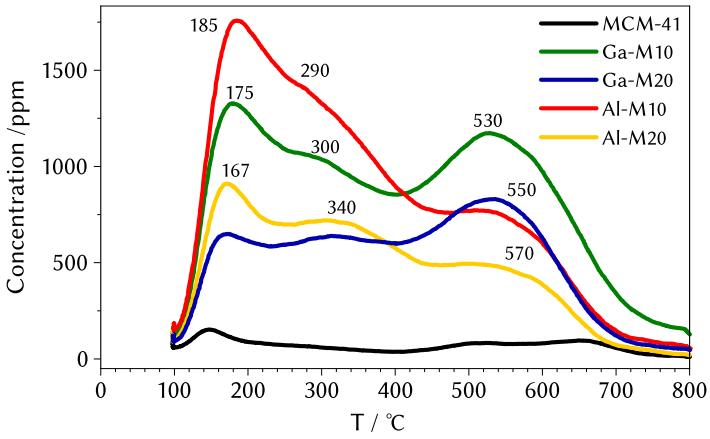

Figure 8.1: NH_3-TPD profiles of all T-MCM-41 supports that were assessed in this study.

exhibited peak desorption temperatures of 570 and 550 °C for Al-M20 and Al-M10, respectively, which are notably higher than the Ga-doped supports at 550 and 530 °C for Ga-M20 and Ga-M10. Although the maximum temperatures are higher at the Al-doped materials, the peak is nonetheless broad and potentially contains stronger sites in all four materials.

Table 8.1: Number of acid sites as determined by Pyr-IR and NH_3-TPD. For the number of BASs, the bands centered at 1544 cm^{-1} were integrated, for LASs, the integration was performed at bands centered at 1455 or 1458 cm^{-1}. The amount of desorbed NH_3 was determined by integration of the whole peak, the ratio was obtained by elemental analysis.

Support	Molar ratio Si/T	Brønsted acidity (BA)	Lewis acidity (LA)	Ratio BA/LA	Amount of desorbed NH_3 / µmol/g
Al-M20	14.1	4.6	4.0	1.2	393
Al-M10	7.3	6.4	8.8	0.7	572
Ga-M20	23.2	1.5	5.9	0.3	370
Ga-M10	11.0	2.3	8.8	0.3	635

Catalytic test reactions were performed within an EPR resonator using Ni impregnated supports. The reaction products were characterized by gas chromatography (GC) in order to determine the selectivity of the catalyst (cf. Figures B.1 and B.2 in the appendix). The active sites were monitored with *in-situ* EPR after quenching the reaction, the results are depicted in Figure 8.2. The intensity of a feature representing reactive sites at $g = 2.63$ is highest at Ni/Ga-M10. Generally, both

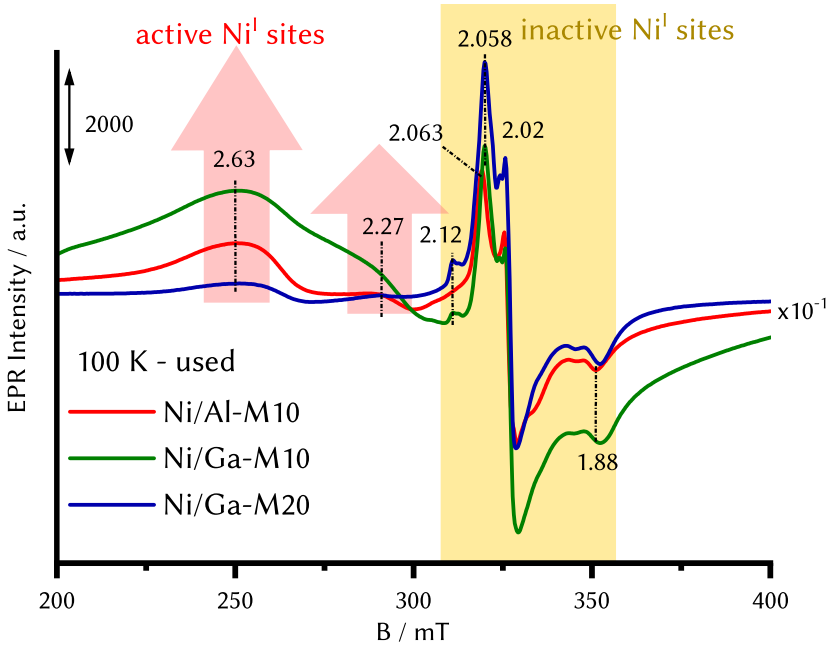

Figure 8.2: *In-situ* electron paramagnetic resonance (EPR) spectra of supports after the reaction, containing active and inactive Ni^{I} species.

Ni/T-M10 materials show much higher intensities than the Ni/T-M20 materials. This is correlating with the conversion monitored by GC that is at 55 to 60 % for the Ni/T-M10 catalysts in Figure B.1 and at 40 to 50 % for the Ni/T-M20 catalysts in Figure B.2 after 5 h. Over time, the conversion of both Ni/Ga-MCM-41 still increases, while it remains stable on Ni/Al-MCM-41 catalysts. At the same time, the selectivity for methylheptene in Ni/Ga-M10 was the highest, featuring $\sim$ 30 % while at the three other catalysts it was between 20 and 25 %. Since the selectivity towards *n*-octenes is generally low at around 5 %, the main focus in on the mentioned methylheptene, which is the preferred product. The amounts of dimethylhexenes is significantly lower in both Ni/Ga-MCM-41 catalysts than in their Ni/Al-MCM-41 counterparts.

The mechanistic pathway of butene dimerization reveals distinct characteristics between Ga-M10 and Al-M10 supports. Initially, the Al-M10 support exhibits an acid-catalyzed mechanism, with free BASs primarily contributing to the formation of branched C_8 products. In contrast, the Ga-M10 support demonstrates a different mechanistic approach from the outset. For Ga-M10, despite having a lower total number of acid sites, the catalyst shows a higher amount of active Ni^{+} species, as confirmed by *in-situ* EPR results. This EPR-active site can be tentatively associated to a Ni-olefin π-complexes complex, which forms during the metal-catalyzed mechanism. [13] The initial carbenium ion mechanism, forming branched products (dimethylhexenes), is quickly replaced by the coordinative mechanism predominantly producing methylheptenes. The Al-M10 support follows a similar but

slightly delayed progression. Branched alkenes are predominantly formed in the first two hours, after which their proportion declines, and methylheptene becomes the main product. When the amount of methylheptene reaches its maximum at a plateau, the proportion of 3,4-dimethylhexene and C_{16} by-products stabilizes at around 15 %. This mechanistic evolution can be attributed to the initial abundance of free BASs in Al-M10, which facilitate the formation of branched products. As these sites become occupied or consumed – potentially due to slower kinetics compared to metal-center catalyzed dimerization – the ratio of the reaction mechanism transitions. Notably, the Ga-M10 support maintains a significantly lower proportion of by-products compared to Al-M10. This observation emphasizes that the oligomerization mechanism is not solely determined by the number of active Ni sites, but critically depends on the chemical environment shaped by the strength of T^{3+} LASs within the MCM-41 framework.

Taken together, the Ga-M10 support possesses the best selectivity in the catalytic reaction while maintaining a similar activity than the other three supports. This goes along with the most intense signal assigned to the active center in the *in-situ* EPR measurements. The number of BASs is not linked to activity and selectivity, nor is the number of LASs. The strength of the acid sites cannot be determined with certainty from Pyr-IR measurements but there are hints for the presence of two types of acid sites and that Ga containing supports have an increased LAS strength. A direct assignment of the type of an acid site to its strength is also not possible through NH_3-TPD. The following NMR experiments were aiming to bridge this knowledge gap and to assign acid site types to their strength.

9 DIRECT NMR MEASUREMENTS

NMR investigations to elucidate the structure of acid sites of MCM-41 derived support materials started with direct investigation of the structurally involved nuclei. This means that the NMR active nuclei were excited themselves and no probe molecule was involved. The nuclei report on important characteristics, as the coordination number of Al or the variation of atoms around Si centers. This was successful for ^{29}Si, ^{27}Al and ^{1}H and will be described in this chapter. Due to the low amount and the large quadrupolar moment, observations of both Ga isotopes, ^{69}Ga and ^{71}Ga were not successful.

9.1 ^{29}SI NMR

In ^{29}Si spectra of Al-M20, three signals are observed after DP (Figure 9.1). As described in ref. [162], starting from a Q^4 site, the chemical shift increases with an increasing number of Al and OH as neighboring atoms of Si. Thus, the signal at -109 ppm represents a Q^4 site while the next signal at -101 ppm (signal B) could represent two species: a Q^4(1 Al) or a Q^3 site. The increase in chemical shift induced by the exchange of one Si by Al or OH, respectively, is of the same magnitude, leading to a similar chemical shift of the two sites. Equally, signal A around -91 ppm could be comprised of three signals: Q^4(2 Al), Q^3(1 Al) and Q^2.

In the corresponding CP spectrum, the Q^4 signal is of significantly lower intensity compared to the DP spectrum, indicating a low amount of protons in close proximity. Polarized via the protons, the two signals A and B at lower field show relatively higher signal intensities as compared to the DP spectrum. This indicates more protons nearby. The maximum of signal A is shifted by 2 ppm downfield which could be tentatively assigned to a second species. Signal B around -93 ppm also presents a shoulder at a downfield shift of 2 ppm which potentially belongs to a second species.

Generally, the signals in the amorphous materials are much broader than in zeolites which is simply caused by the lack of crystallinity, hence a much more inhomogeneous environment. Those broad signals were also reported on in ref. [35]. This hampers a clear assignment of the individual signals to one of the discussed species, hence no such assignment is made here.

1 The full simulated spectrum together with the simulation is depicted in Figure B.3.

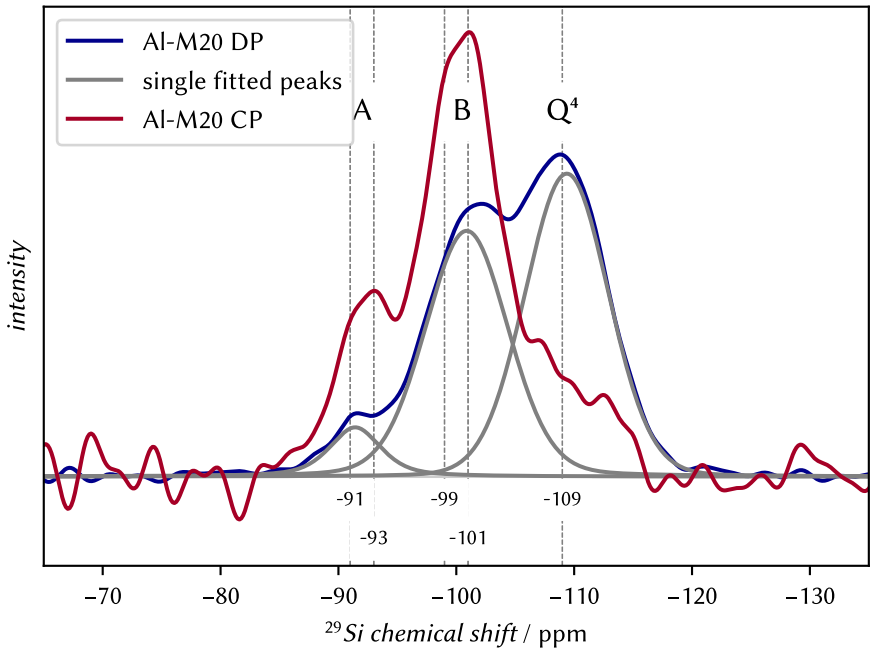

Figure 9.1: ^{29}Si-NMR measurements of the support Al-M20 using DP (blue) and CP (red), together with the deconvolved signals of the DP spectrum (gray)[1]. DP excites all ^{29}Si nuclei simultaneously, CP transfers polarization from ^{1}H to ^{29}Si nuclei and thus excites surface Si. The spectra are normalized to their number of scans. For further details on the signal assignment see the text.

9.2 ^{27}Al NMR

In ^{27}Al spectra (cf. Figure 9.2) of Al doped supports, two signals represent two different Al species: tetrahedral Al with higher (54 ppm) and octahedral Al at lower (1 ppm) chemical shift values. The highfield signal shows the presence of extra framework aluminium (EFAL) present in form of clusters or areas on the surface (cf. Section 4.2.2). Those clusters possess LASs and are not relevant for the catalytic butene dimerization. [1]

9.3 ^{1}H NMR

The proton spectra are a tool to directly observe surface BASs among the other proton sites within the materials. However, as described in Section 4.2.1 the correct treatment is key for a conclusive spectrum. Therefore, different methods of dehydration were tested.

The two Ga-M10 samples were dehydrated at 450 °C under static (referenced as method 1.1 in this section) or dynamic (method 1.2) vacuum (10^{-3} mbar). The container was sealed and inserted in a N_2 glovebox where the material was packed into a rotor. The dehydrated samples, referenced as method 2, were dehydrated under dynamic vacuum ($5 \cdot 10^{-3}$ mbar) at 300 °C and subsequently sealed in a helium

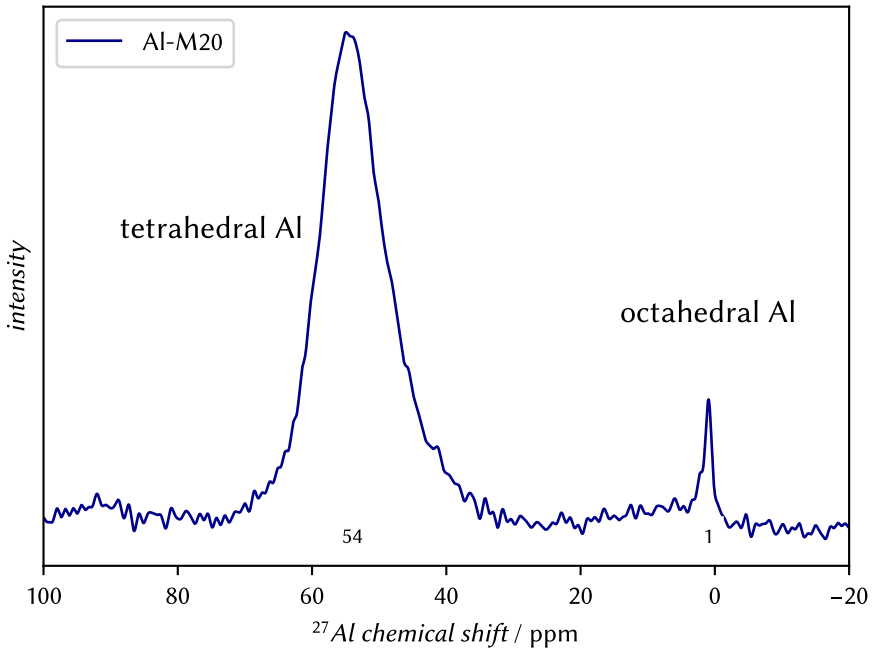

Figure 9.2: ^{27}Al-NMR measurements of the support Al-M20.

atmosphere in the vacuum line. The non-dehydrated samples were filled into rotors directly after re-calcination (cf. Section 5.1, 2 K/min to 400 °C, keep for 2 h, cool down at 20 K/min to room temperature under flowing Ar or synthetic air). Although brief exposure to air while removing the material from the oven allowed some surface interaction with humidity, potentially affecting the acid sites, this treatment likely preserves the material's key properties – evidenced by its retained catalytic activity [5]. The spectra of those samples are shown in Figure 9.4.

In order to ensure that my method provides meaningful results, results known from the literature were repeated, as is good scientific practice. **[feyn-engsci-37-7-10]** USY was used as a reference material because it contains only one Al crystal position and has large pores, making it both simple in structure and not too far from the mesoporous structure in terms of pore size. Details are given in 5.1. In comparison to Al-MCM-41 materials, there are more references available in the literature for USY. It is therefore described first. It was not further dehydrated and analyzed after calcination and short contact to the laboratory atmosphere. In its proton spectrum in Figure 9.3, many more distinct sites than in MCM-41 derivatives are present. The signals are comparable to literature as shown in Table 9.1. The protonic sites are much better defined in USY due to its crystallinity in comparison to amorphous MCM-41. The signal assignments of USY in the literature agree in general between themselves, however, they vary somewhat in their chemical shift and attribution to SiOH or framework groups. The comparison between the literature values and the obtained spectrum

of USY is given in Table 9.1, the spectrum is compared with one measurement of Ga-M10 in Figure 9.3. The signals obtained for USY do not deviate significantly from the literature. Therefore, it seems that the surface of the prepared USY zeolite material is relatively "clean" and adsorbents from the laboratory atmosphere are not observable to any great extent.

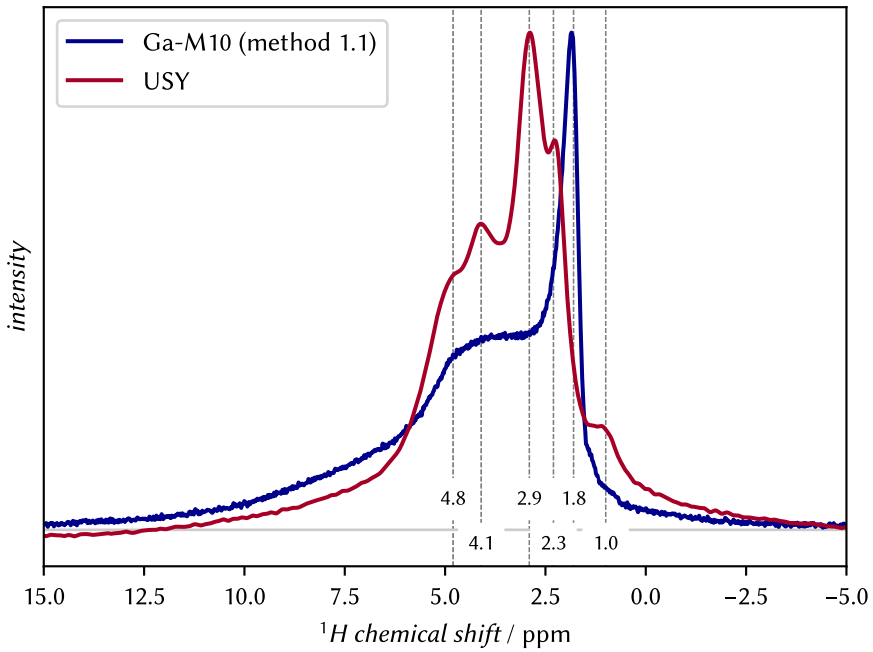

Figure 9.3: ^{1}H-NMR measurements of USY in comparison to Ga-M10 (method 1). The spectra are normalized to their maximum.

Table 9.1: Comparison of ^{1}H chemical shifts of USY in this study (spectrum in 9.3) and in literature to estimate the accuracy of NMR for this material. All references observe the protonic form of USY.

	proton chemical shift $\delta(^1\mathrm{H})$ / ppm			
site	this study	ref. [244]	ref. [245]	ref. [246]
isolated BAS (Al-OHSi)	–	–	6.5	–
BAS (sodalite)	4.8	4.8	4.5	4.6
BAS (super)	4.1	4.1	3.2	3.6
Si-OH	1.8	1.8	1.9	–
Al-OH	2.3	2.3	2.6	2.6
SiOH (nonacidic)	1.0	1.0	–	1.6
framework defects	–	1.3	–	–

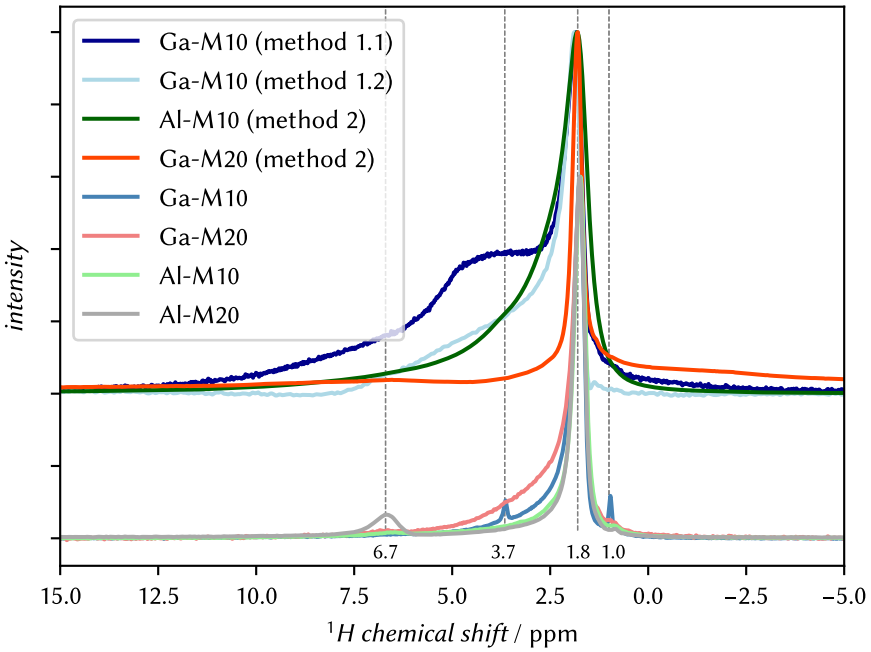

Figure 9.4: ^{1}H-NMR measurements of differently dehydrated support materials. The top part shows spectra of dehydrated samples, while the bottom part presents spectra of supports that were not separately dehydrated. All spectra are normalized to their maxima.

The spectra of the differently treated MCM-41 derived materials are shown in Figure 9.4. Non-dehydrated MCM-41 support materials (bottom in Figure 9.4) possess a strong signal 1.8 ppm, accompanied by smaller signals at 1.0, 3.7 and 6.7 ppm. The main signal is caused by silanols. While the signal at 1.0 ppm is present in all samples, this is not the case for the two other signals. The former likely results from non-acidic silanols as compared to Table 9.1. The origin of the other signals remains ambiguous, since they appear at one single sample each. Since the protons of EFAL are characterized by signals between 2.6 to 3.6 ppm, the analogous extra-framework Ga species could cause the signal at 3.7 ppm in Ga-M10. Acid sites typically produce signals at chemical shifts of 3.6 ppm and above. While the observed signal at 6.7 ppm in Al-M20 falls within this range and could potentially correspond to an acid site, definitive confirmation of this assignment requires additional evidence.

Since no clear evidence of acid sites was observed with the non-dehydrated materials, the treated supports are compared in the upper part of Figure 9.4. The dehydrated materials show a major proton signal with shoulders in the range between 0 and 15 ppm. Signals of acid sites are expected in this region. The signal of silanols [247] was observed at $\sim$ 1.8 ppm in all spectra with a prominent shoulder extending to 12.5 ppm. The shoulder of the signal shows distinct regions that can be separated into two parts from the approximate turning point of the signal of Ga-M10 (method 1.1): one from 2.5

to 5.5 ppm and another from 5.5 ppm towards the low-field region. Despite similar dehydration procedures, Ga-M10 (method 1.1) shows pronounced intensity in both shoulder regions, while the similarly treated Ga-M10 (method 1.2) displays reduced intensity in both regions, with the signal decreasing to the baseline at around 7.5 ppm. The two spectra of materials treated with method 2 exhibit notably less prominent shoulders compared to the other samples. Above 1.8 ppm, they decrease relatively quickly to the baseline. The species causing the shoulder-signals were presumably removed by the heat treatment. A significant decrease in the number of acid sites was, however, not observed after impregnation with TMPO (cf. Section 11.4). The shoulders could be related to protons of acid sites but no specific site can be distinguished, as it is possible in USY.

While the proton spectra reveal slight differences in their signal patterns, a definite interpretation of these variations cannot be made. Samples that were dehydrated very similarly show distinctly different signals that do not allow for assignments of the acid sites apart from potentially acidic and non-acidic silanol protons.

10

NI IMPREGNATED SUPPORTS

The surface of the MCM-41 based materials contains protons in form of silanols or as BASs, making proton detection the most straightforward way to observe BASs. This was done directly after impregnation with Ni. The accumulation rate was very high, with a delay of only 1 ms. Therefore, the free induction decay (FID) had not always decayed, which is why the signal is broadened at 1 ppm and shows oscillations. This trade-of was deliberately accepted to allow for sufficient accumulations and hence signal-to-noise ratio of the recorded spectra. Additionally, signals with long T_1 are suppressed, the short repetition rate therefore acts as a T_1-filter. The four support materials

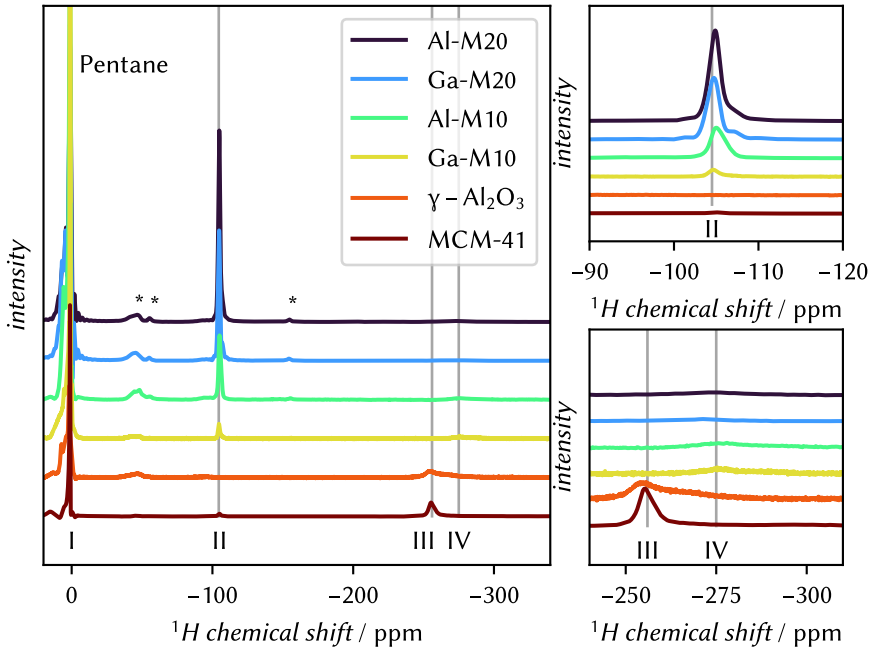

Figure 10.1: ^{1}H-NMR measurements of MCM-41-based supports impregnated with $Ni(Cp)_2$. The remaining educt $Ni(Cp)_2$ is visible at −256 ppm while the signal at −105 ppm is only present on Brønsted acid supports and not on non-Brønsted acidic MCM-41 and γ-Al_2O_3. The spectra are normalized for their scan-number. Asterisks denote spinning sidebands from MAS.

as well as γ-Al_2O_3 and purely siliceous MCM-41 were impregnated with Ni and ^{1}H-NMR spectra (cf. Figure 10.1) were obtained as described in Section 6.2. Four signals are apparent at chemical shifts of 1, −105, −256 and −275 ppm and are denoted with Roman numerals I to IV, respectively.

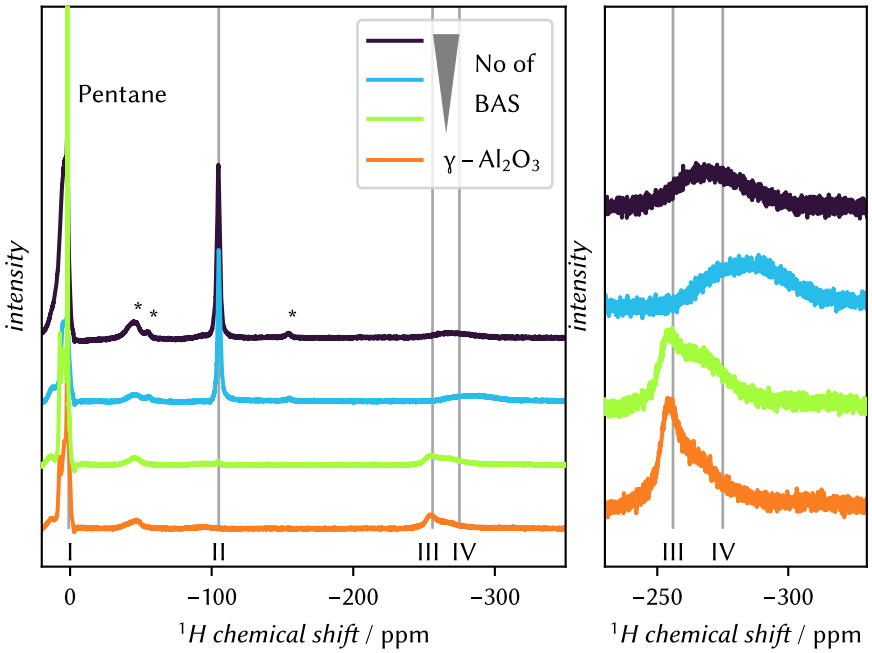

Figure 10.2: ^{1}H-NMR measurements of γ-Al_2O_3-based supports impregnated with $Ni(Cp)_2$. The substances are sorted according to the number of BASs as determined by Pyr-IR, which increases from bottom to top. Asterisks denote spinning sidebands from MAS.

Signal I at 1 ppm results from residual pentane that was used for impregnation. Upon acquisition of an undistorted spectrum with a longer acquisition time (cf. Figure B.4), the signal is split into three peaks which fit the literature values of pentane and silanols. [248] An analysis on this signal is pursued below after a description of all the other signals.

In the presence of nickel, paramagnetically shifted signals II, III and IV appear in different combinations. According to literature, signal III belongs to (crystalline) $Ni(Cp)_2$ [228, 249] that did not attach to an acid center and remains unbound. This signal is present on siliceous MCM-41 and γ-Al_2O_3 only. Both supports are not Brønsted acidic. γ-Al_2O_3 does only contain LASs while siliceous MCM-41 only possesses non-acidic silanols. Both are lacking signal II at −105 ppm which is the most interesting signal. It is only present at T^{3+} doped supports – materials that possess BASs. This provides evidence that BASs are required to bind Ni and subsequently drive the catalysis. This correlates with the results of the catalytic tests which were not successful on SiO_2, siliceous MCM-41 or γ-Al_2O_3. [1, 5] The narrow linewidth of signal II suggests fast dynamical motion and a resulting self-decoupling mechanism of protons from the immediate paramagnetic environment. Both the short relaxation time and the significant paramagnetic shift, further indicate proximity to a paramagnetic center. When signal II is present, signal III from $Ni(Cp)_2$ disappears. T^{3+} doped supports possess signal IV instead of signal III, but signal IV is significantly

less intense than signal III in the aforementioned supports, or even barely visible. However, this signal becomes especially evident on a different series of alumina-based materials with increasing amount of Si. They were investigated by Lasse Serger in his Bachelor thesis [250]. Composition-wise, this class of materials is the counterpart to MCM-41 based materials. The aim was to investigate similarities of those materials, since they can also be used for the dimerization of butenes. [3] Starting from pure γ-Al_2O_3, with incorporation of Si, the number of BASs increases simultaneously. The corresponding spectra are shown in Figure 10.2. In this series, the intensity of signal II increases with an increasing amount of BASs. At the same time, a broad signal IV below -275 ppm is present at different chemical shifts. It is much broader than signal II, reporting on slower dynamical processes of the underlying proton. This signal may therefore result from surface protons experiencing the paramagnetic influence of Ni. However, further characterization or a more precise assignment was not possible.

In all materials, the large signal I around 1 ppm results from pentane and other surface protons and is partly suppressed due to their longer relaxation time combined with the rapid acquisition. The paramagnetic high field peaks have a very short relaxation time, which allows for rapid detection. This is depicted in Figure 10.3 where measurements of Al-M20 with different repetition times are shown. For a repetition time of 2 ms, the intensity of signal II is not significantly smaller than after full relaxation at 5 s, indicating that the observed protons are again fully relaxed before the next excitation. At the same time, signal I presents an increasing intensity with longer repetition times. This evidences the longer relaxation time and a larger distance to paramagnetic Ni. The repetition time of 1 ms that was chosen for further measurements is very close to the limit of acquisition, since the FID has not decayed by then. The proton chemical shift of signal II depends highly on the temperature and therefore on the MAS frequency. Exemplarily, Figure 10.4 shows the MAS frequency dependency for II. With increasing MAS frequency, the temperature rises from friction of bearing and driving gas flows and the signal moves downfield. Refs. [249] and [228] provide a more detailed description of temperature-dependent $Ni(Cp)_2$ signals. Therefore, the spectra were always obtained using a constant MAS frequency of 20 kHz.

To investigate the origin of the paramagnetically shifted signals, deuterium-exchanged samples were impregnated with $Ni(Cp)_2$ as well and monitored with ^{1}H NMR. Hypothetically, if signal II results from a neighboring proton, the deuterated samples should possess a significantly less intense, or even no signal at all. The spectra are compared with the non deuterated samples in Figure 10.5. The position of the signals II and IV is the same as in the non-deuterated supports. Signal II is present in all three spectra. Peak IV is also present in

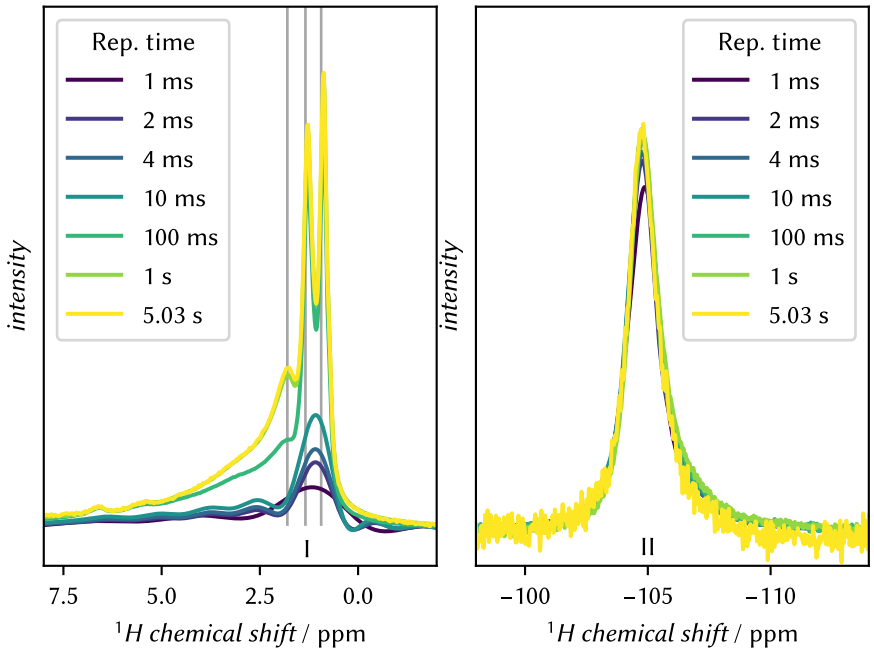

Figure 10.3: Measurement series with Ni impregnated Al-M20 to investigate the influence of the experiment repetition time on the signal intensities of signals I and II. The lines in the left part are at 0.94, 1.34 and 1.8 ppm.

supports prior and after deuteration. This observation suggests that signal II is unlikely to originate from a neighboring acidic proton, as such a proton would have been exchanged with deuterium, which would have depleted the signal completely. Signal IV is present on both protonated and deuterated supports. Therefore, it either belongs to non-acid – and therefore non-exchanged – species or to another proton species that is unknown so far. The presence of protons at −105 ppm (signal II) can be explained by different mechanisms: 1) an insufficient portion of acid protons was exchanged by deuterium, 2) the acid deuterium sites were back-exchanged during the impregnation process, 3) signals do not originate from protons of the surface, but from protons of a part of the solvent pentane which is in proximity to Ni. The deuterated supports were also characterized by ^{2}H NMR (cf. Appendix C). Spectra were obtained at temperatures between 220 K and 293 K, however, no proper characterization of specific sites was possible since spinning sidebands were Gauss distributed and did not present a characteristic Pake pattern. This is described in more detail in the Appendix chapter C. However, a significant amount of deuterium was present. The group of F. Perras carried out the exchange in the same way [251] and showed in their publication [70] that the procedure exchanges most of the acid centers of ASA and ZSM-5. Therefore, the deuterium exchange seemed to be successful. In combination with the recorded spectra, this confirms that the exchange took place in the MCM-41 materials as well. The back-exchange mentioned

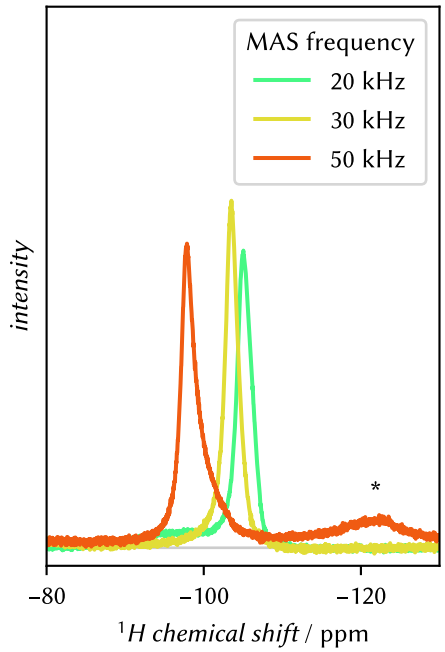

Figure 10.4: ^{1}H-NMR measurements of Al-M20 impregnated with $Ni(Cp)_2$, detailed view on the signal around −105 ppm that shifts downfield with increasing MAS frequency.

in the second point requires exchangeable protons during the impregnation. While benzene is used to selectively exchange strong acid sites ($pK_a = 43$), pentane is slightly less acidic ($pK_a = 45$). Therefore, a large-scale deuterium exchange of acid sites of medium strength by pentane is unlikely.

The assignment of signal III at −256 ppm to Cp protons is based on literature. [228] Upon impregnation with $Ni(Cp)_2$ one Cp^- anion reacts with a proton from a BAS and is then released. The residual $[Ni(Cp)]^+$ gets bound by the electrons of the corresponding basic center. [3] A part of the Ni changes its oxidation state from Ni^{2+} to Ni^+, but the majority remains as Ni^{2+}. The signal at −105 ppm therefore likely results from the residual Cp^- attached to surface-bound Ni. The difference in chemical shift might result from variations of the oxidation or coordination state. The Ni atom of surface-bound $[Ni(Cp)]^+$ receives less electron density from the support than it did from the second Cp^- ring which interacts via one σ bond and two π bonds. [238] Thus, the electron density at the surface-bound Ni center is considerably lower than in $Ni(Cp)_2$. Therefore, a change in the coordination state of Ni could also induce the downfield shift of signal II. However, no systematic NMR investigations of Ni in different oxidation or coordination states could be found in literature.[1] Quantum-chemical calculations could be able to elucidate on the effects of a change in the oxidation

1 There are a few publications on ssNMR on Ni complexes with different ligands, however, a systematic change in chemical shift was not observed. [252, 253]

state and the ligand exchange on the chemical shift. It is also possible to associate this signal with the solvent pentane, but this signal, which could also consist of two signals, would be significantly broader and therefore probably not recognizable as such.

Due to the paramagnetic nature of $Ni(Cp)_2$, precise characterization and quantification are difficult if not impossible using NMR spectroscopy. Short relaxation times and large peak linewidths render it impossible to use longer pulse sequences like CP. This being said, the aforementioned arguments indicate the assignment of signal II to the protons of the non-deuterated cyclopentadienyl ring of $[Ni(Cp)]^+$ that is present on the surface in any case. The pentane that was used for the impregnation also contains protons. However, it is not able to back-exchange D vs. H on the acid centers. For complementary experiments, the use of fully deuterated $Ni(Cp)_2-d_{12}$ was not possible, as this variant is not available for preparation or purchase.

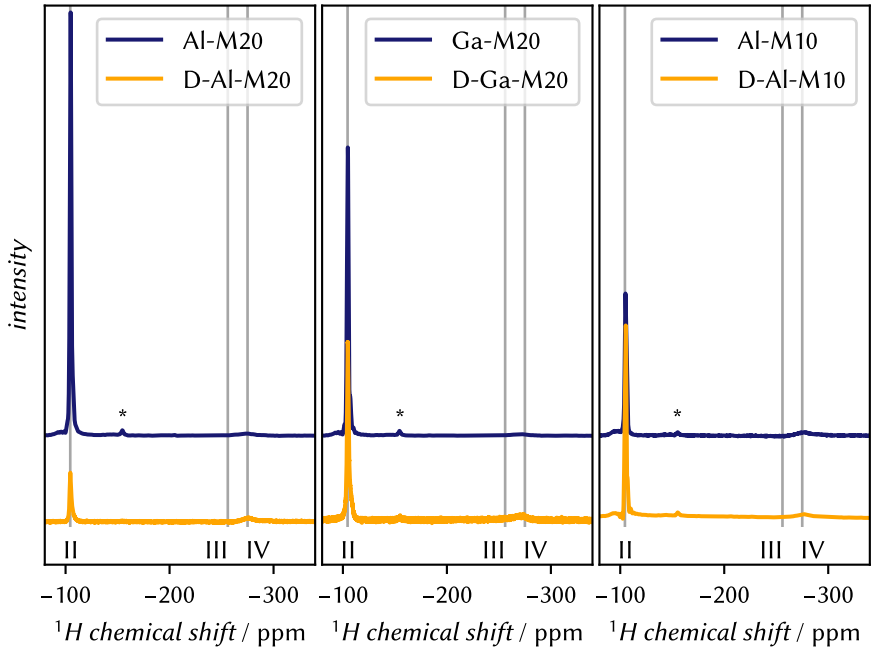

Figure 10.5: ^{1}H-NMR measurements of deuterium exchanged, Ni impregnated materials in comparison with their non-deuterated counterparts. The signal position is the same, the intensities do not follow a trend.

In summary, given the fact, that signal II at −105 ppm is only present when the support's surface is also BRØNSTED acidic, the observable protons are necessarily very close to the reactive metal center. To conclude about the nature of those protons, the signal shape and the experiments with the deuterated supports are taken into account. The signal is rather sharp and intense. Upon impregnation of the support with $Ni(Cp)_2$, one Cp ring is released and the residual $[Ni(Cp)]^+$ is attached to an acid site. The second ring is still connected to the Ni atom. The ring rotates at room temperature, decoupling the protons

and narrowing the signal. Surface protons are potentially observable at −275 ppm as a very broad signal (signal IV). Here, the paramagnetic interaction is not averaged and therefore broadens the signal much more. The signature of the pure $Ni(Cp)_2$ is only found as signal III if no BAS is available on the support to attach to. The differences between the four MCM-41 support materials are rather small: The signals occur at the same position, only the intensity varies slightly. A correlation with the amount of acid sites seems plausible, however, the paramagnetic properties of the Ni hinder proper quantification.

11

ACIDITY MEASUREMENTS OF SUPPORT MATERIALS

Acid sites were also investigated using Pyr-IR and NH_3-TPD. The analysis reveals the existence of two types of acid sites of at least two strengths. However, both methods are not able to assign the strength to a type of acid sites and *vice versa*. This is the reason for detailed investigations using the NMR probe molecule TMPO which allows for this assignment and to correlate the type of acid site with their strength.

The spectrum of TMPO impregnated supports was usually decomposed into four signals which will be labeled *B1*, *L*, *B2*, *P* and *C* as shown in Figure 11.1, which stands for the assignment to BASs (*B1* and *B2*), LASs (*L*), physisorbed species (*P*) and crystalline TMPO (*C*). Physisorbed TMPO possesses a chemical shift below 50 ppm [194] while crystalline TMPO appears at $\sim$ 41 to 42 ppm and possesses a spinning sideband pattern from the relatively large CSA of TMPO. Superacid sites with a chemical shift above 80 ppm occur on one sample and are designated *SA*.

Samples were prepared using three different impregnation methods, the solvent-based **method 1** and the two different solvent-free **methods 2** and **3**. The two latter differ since in **method 2**, the support material was first heated under vacuum, before TMPO was applied directly in a rotor. In **method 3**, support and TMPO were mixed in a SCHLENK tube before distribution of the probe by heat. All methods are explained in Section 5.2.

In the first part, the optimal ratio of TMPO loading was assessed by impregnation of one material with different amounts of TMPO and subsequent assessment of the spectra. Secondly, the distinction between BASs and LASs is discussed. Next, it was investigated, whether TMPO-dimers form upon impregnation via two-dimensional HETCOR spectroscopy. Due to an extra signal which is not related to an acid site, dimers would mislead the interpretation of the spectrum. Different impregnation methods are compared to recognize artifacts from the preparation. Eventually, the characteristic features of the four materials are discussed.

In a further experiment, a double impregnation with TMPO and Ni was performed to extract information on the occupation of acid sites by Ni on the active catalyst.

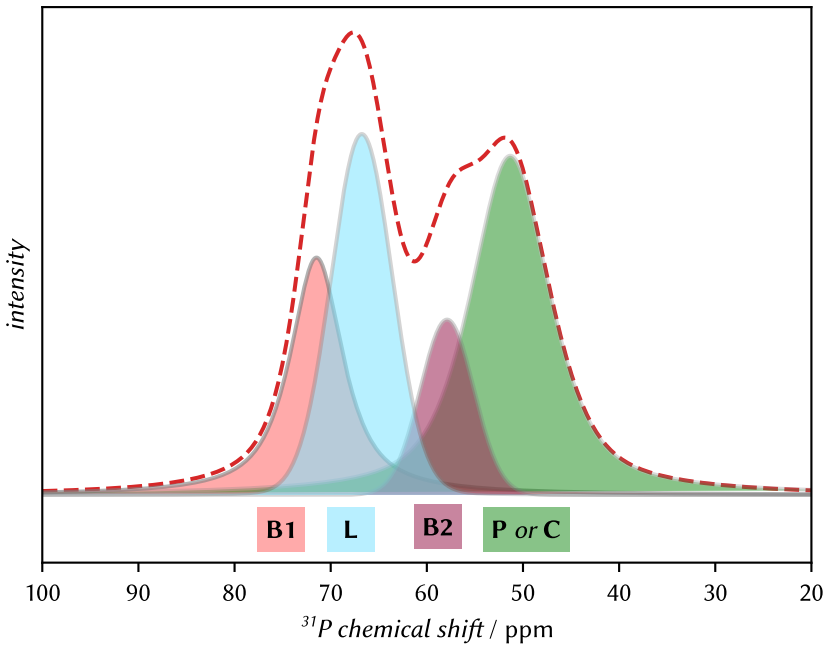

Figure 11.1: Prototypic ^{31}P NMR spectrum after impregnation with TMPO on a MCM-41 support. The naming of the four signals is provided, the signals are here colored for clarity. The names are derived from B – Brønsted, L – Lewis, P – physisorbed and C – crystalline.

11.1 AMOUNT OF TMPO

For the impregnation with TMPO, different amounts are suggested in literature as mentioned in Section 4.4.3. The amount of TMPO is relevant for the accuracy of the results. The TMPO concentration must be sufficient to detect all acid sites, yet excess unbound TMPO should not obscure signals from bound species. Furthermore, the formation of $(TMPO)_2H^+$ dimers needs to be avoided.

A concentration series was conducted on Al-M20 with P/T = 0.2, 0.6, 1.0 and 1.5 to estimate the optimal amount of TMPO for the impregnation in this case. The spectra are shown in Figure 11.2. Two signals are observed: a combined (*B1* + *L*) signal around 65 ppm and another (*B2* + *P*) around 45 ppm. Their intensities vary with TMPO content. At the lowest TMPO amount, the 45 ppm signal is barely visible. As TMPO increases, both signals grow, but the 65 ppm signal appears to saturate, while the 45 ppm signal continues to increase without reaching saturation within the tested TMPO amounts. From the direct comparison of the four spectra, it is obvious, that with a low amount of TMPO (P/T = 0.2), only the stronger acid sites, present in the lowfield signal, are covered while the signal(s) between 40 and 50 ppm are not present at a reasonable SNR. With increasing loading, the intensity of the highfield signal increases more than the lowfield signal. The spectra were deconvolved subsequently, the results are

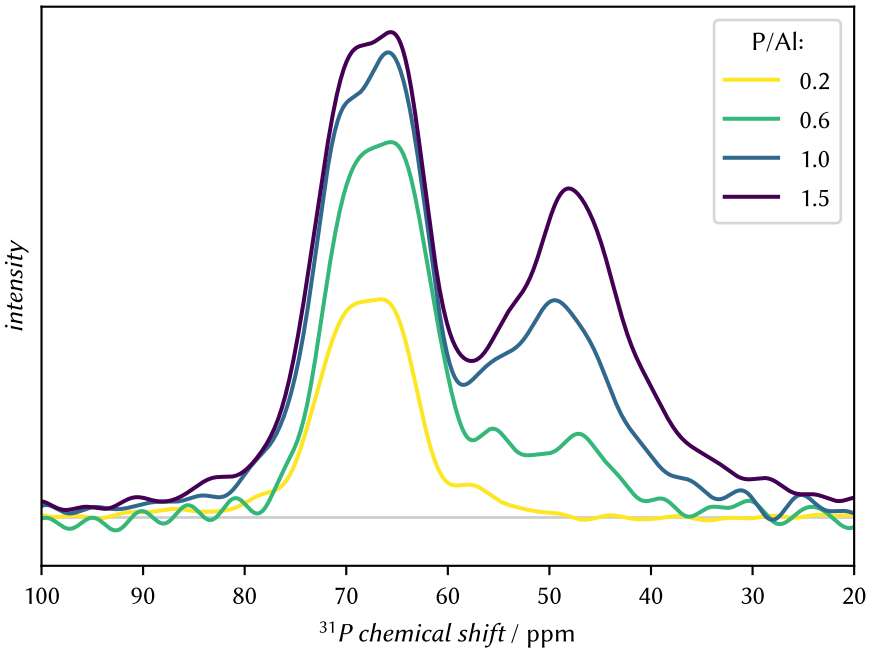

Figure 11.2: ^{31}P NMR spectra of Al-M20 impregnated with a varied amount of TMPO. The TMPO amount ranges from P/Al = 0.2 to 1.5. All spectra are normalized to their number of accumulations (1024 for 0.2, 128 for 0.6 and 1.0, 256 for 1.5).

presented in Figure 11.3. At P/T = 0.6, three sites are observable after decomposition in Figure 11.3: two in the range from 60 to 75 ppm and one sites between 40 and 55 ppm, respectively. The latter is relatively broad, and splits into the two signals *B2* and *P* in the following two spectra of the series with P/T = 1.0 and 1.5. The signal *P* at 48 or 49 ppm most likely reflects the signal of physisorbed TMPO that is unspecifically bound to the surface. [207, 222] No spinning sideband pattern was observed. This suggests, that the residual TMPO is in an amorphous, and not in a crystalline form. The signal *B2* at 55 and 56 ppm is in the chemical shift region of acid sites, but its amount is rather small. The two signals *B1* and *L* belong to acid sites, that are characterized in more detail later.

From this series, it was decided to use the ratio P/T = 0.6 for further investigations since it allows for the detection of the acid sites of different strengths without too much free TMPO present. It was decided against the P/T = 0.2 for a better SNR. The choice of P/T = 0.6 ensures the maximum ratio of 1:1 between acid sites and TMPO such that the risk of dimer formation in minimized. Moreover, it was decided to use a given P/T ratio instead of using a certain mole fraction per gram of material, which is also present in literature. [254] This decision takes into account the varying amounts of T^{3+} in the four support materials.

A third method of impregnation was performed only on Ga-M10 with two amounts of TMPO of P/T = 0.2 and 0.6. The different impreg-

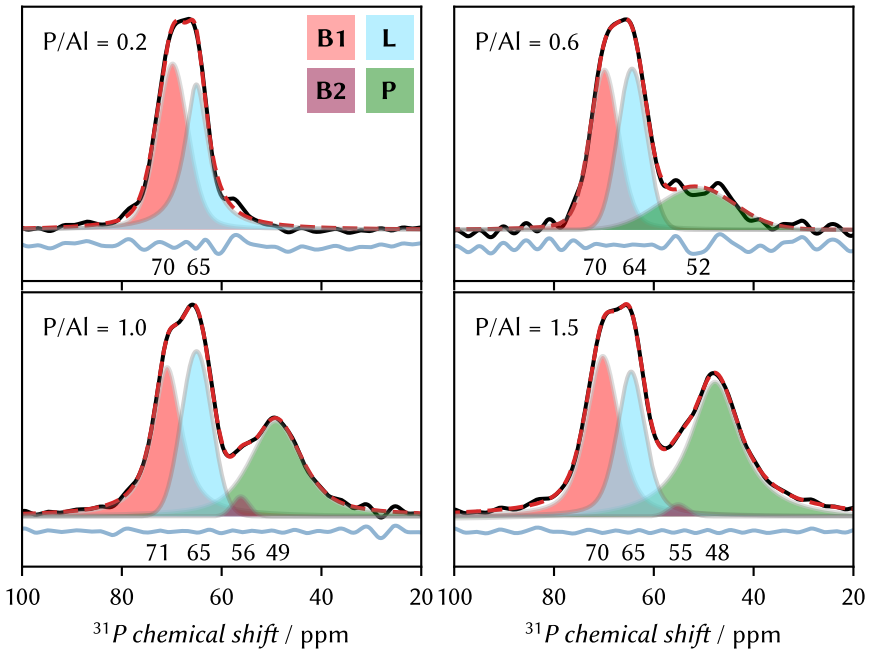

Figure 11.3: Experimental spectra (black), sum (red) and single peaks (grey) of the deconvolved ^{31}P NMR spectra of Al-M20 impregnated with a varied amount of TMPO between P/Al = 0.2 and 1.5 applying **method 1**. Residues are displayed in blue below the spectra, the numbers are the maxima of the single peaks.

nation methods are described in the experimental part Section 5.2. The resulting spectra (cf. Figure 11.4) possess signals of very comparable chemical shifts after deconvolution as the spectra of impregnation **method 1** in Figure 11.3. It is to note, that for **method 1** in Figure 11.3, Al-M20 was used while Ga-M10 was prepared using **method 3** as shown in Figure 11.4. At low loading (Figure 11.4, left), the signal *P* at 48 ppm is smaller than the lowfield signal of *B1* and *L* together. At higher loading (Figure 11.4, right), the signal intensity of *P* is larger than signals *B1* + *L*. At the same time, the lowfield combined signal (*B1* + *L*) has a higher absolute intensity at higher loading. At low loading, the ratio suggests that acidic sites bind the probe molecule strongly, with most TMPO being bound to the surface rather than remaining unbound. However, this does not mean that TMPO exclusively or primarily covers all strong acid sites. If that were the case, the (*B1* + *L*) signal would not increase in intensity as TMPO loading increases.

In contrast to the first series with Al-M10 (Figure 11.3), signal *P* is present on the solvent-free impregnated sample with P/T = 0.2. Otherwise, there are no major differences between the two impregnation methods. With both, four signals were observed at comparable chemical shifts. After establishing the differences between both impregnation **methods 1** and **3**, they were subsequently applied to characterize the acid properties of four different materials.

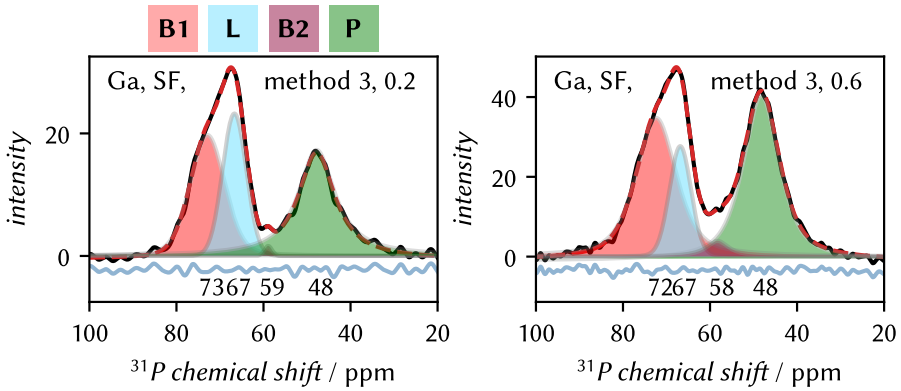

Figure 11.4: Deconvolved ^{31}P NMR spectra of Ga-M10 impregnated with P/T = 0.2 (left) and 0.6 (right) TMPO applying the solvent-free (SF) impregnation **method 3**.

11.2 DISTINCTION BETWEEN BRØNSTED AND LEWIS SITES

To discriminate between the different types of acid sites, hydration experiments were performed for the samples of the impregnation series with **method 1** and **2**. Upon hydration, signals of LASs are expected to disappear due to their weak bond in contrast to the stronger hydrogen bonds of TMPO with BASs. as described in Section 4.4.2. The deconvolution of the spectra before and after hydration of the solvent-based impregnated supports are shown in Figure 11.5 the ones of the solvent-free supports in Figure 11.6. The spectra in the top row of each series were acquired directly after impregnation. The spectra with blue background represent the hydrated samples. The hydration procedure is described in Section 5.3. All spectra of **method 1** posses four signals, however, the support material Ga-M20 exhibits an additional signal *SA* at 86 ppm which represents superacid sites. This signal was observed only once.

In direct comparison of spectra before and after hydration of **method 1**, it is observed that signals *B1* of each material does not shift more than the anticipated 1 ppm, this is in the error range of ssNMR. The signal *L* between 66 and 70 ppm has disappeared in all hydrated samples, as has *SA* at Ga-M20. In the spectra of the hydrated samples, a signal appears at 55 to 56 ppm which is much sharper than any previously observed signal. The signal from TMPO dissolved in water has a chemical shift of 53 ppm, but is dependent on its environment. [184, 255] A comparison of hydrated spectra with water-dissolved TMPO is given in Figure B.7. Since the mesoporous support represents a less protic environment than water, TMPO has a slightly higher chemical shift (cf. 4.4.2). The corresponding signal is therefore assigned to hydrated TMPO, which is now abundant in the pores. During hydration, the bond between LASs and TMPO is hydrolyzed, therefore, the signals of LASs disappear. Signals of BASs remain, since the bond

between TMPO and BASs is strong enough. Therefore, the signal *B1* between 73 to 75 ppm of the solvent-based samples (Figure 11.5) stem from a BAS, while the disappearing signals *L* at 66 to 67 ppm result from a LAS. The low amplitude of signal *B2* between 57 and 59 ppm is still present after hydration and therefore belongs to a BAS. The physisorbed TMPO (49 to 54 ppm), dissolves in water and is now present in the sharp signal at 52 to 56 ppm.

The comparison of the spectra after solvent-free impregnation **method 2** (Figure 11.6) yields analogous results: After hydration signal *B1* remains, while signal *L* disappears. Samples of **method 2** possess a signal of residual TMPO at 43 to 45 ppm which possesses spinning sidebands (cf. Figure B.5). This indicates that TMPO is present in its crystalline form and the signal is referenced as *C*. In this experiment, Ga-MCM-41 samples were impregnated with P/Ga = 1.5 while Al-MCM-41 supports are impregnated with P/Al = 0.6. Unlike the spectra obtained after applying **method 1** (Figure 11.5), the spectra of all samples display the *C* signal with markedly increased intensity. Seemingly, the heat transfer from the heating jacket to the rotor was not high enough to melt and to evenly distribute TMPO on the supports. Since *C* is more intense than that of TMPO on acid sites, it potentially covers the small *B2* signal that is present for the solvent-based impregnated samples. The large signal, in this case, can either be fitted with one single or two peaks. The use of two peaks results in a very similar chemical shift, but one signal is of a high intensity and narrow width, while the other is of a lower intensity and broader width. Upon hydration, the whole signal completely disappears and hydrated TMPO is represented at 52 to 54 ppm. This again is fitted with two signals, one shifted by 1 ppm. It was not possible, to adapt the parameters, that one signal would suffice for an accurate fit. Probably, one signal stems from dissolved crystalline TMPO while the other is dissolved TMPO within the pores.

An additional signal at 58 to 63 ppm of low intensity is present in the hydrated spectra. Its position is exactly in the valley between the two peaks of the non-hydrated spectra, the direct comparison is shown in Figure B.8. It might be the case that this additional signal is also present in the non-hydrated spectrum, but is too small to be taken into account during the fitting procedure. This is in contrast to the samples from **method 1** where three of four materials possess this signal after impregnation that is conserved after hydration. Since with **method 2**, the signal is only present after hydration, it could belong to an acid site that was vanishing during the strong dehydration process, the samples were exposed to. Upon hydration, the BAS could have formed again, observable as the small signals *B2*.

The assignment of the other signals is analogous to the solvent-based impregnation: The highest chemical shift belongs to a BAS, the second to a LAS. The large signal at 43 or 44 ppm belongs to crystalline

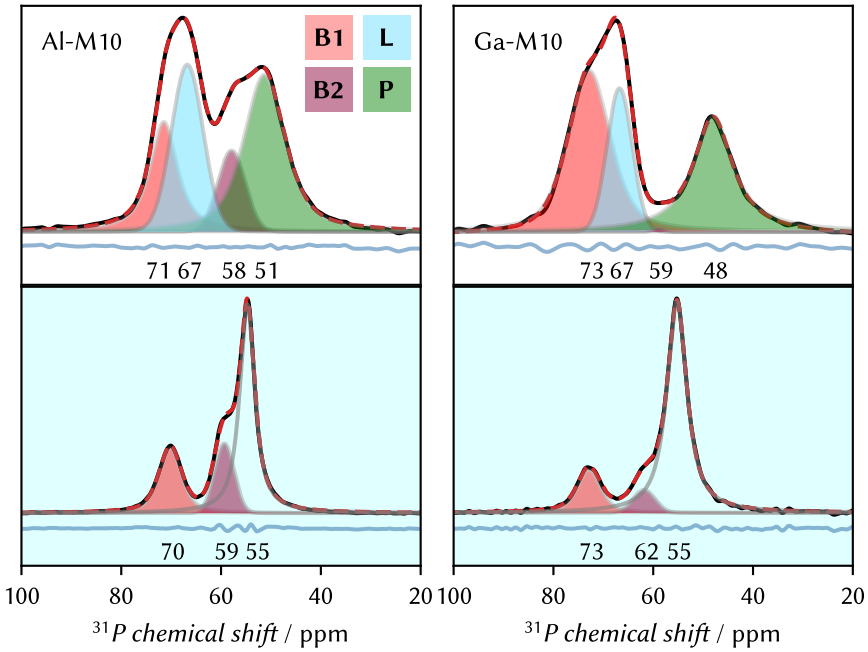

(a) T-M10 supports

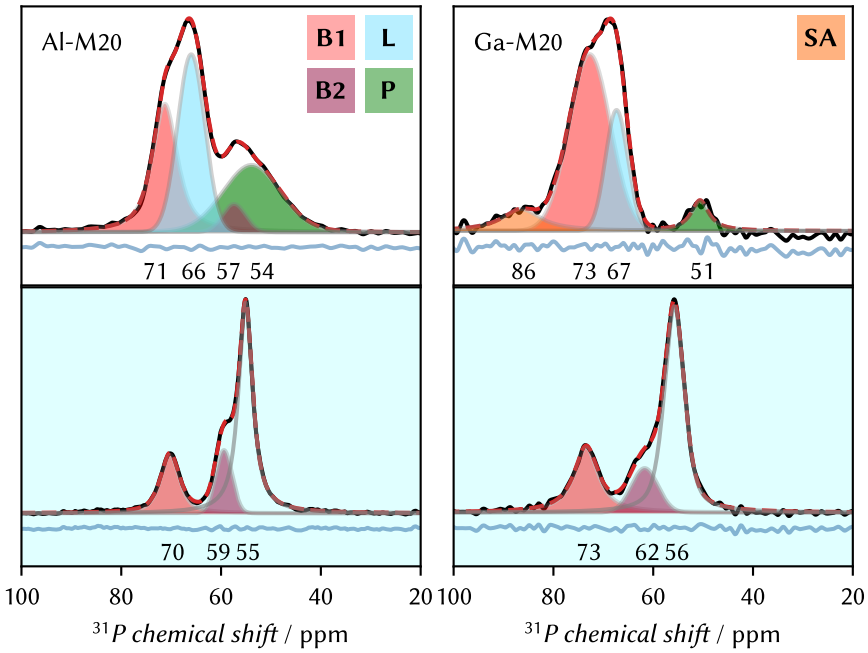

(b) T-MCM20 supports

Figure 11.5: Deconvolved ^{31}P-spectra of solvent-based samples prepared according to **method 1** (white background) and after subsequent hydration (blue background). Ga-MCM-41 samples were impregnated with P/Ga = 1.5 while Al-MCM-41 supports are impregnated with P/Al = 0.6. The intensities are arbitrary and not normalized.

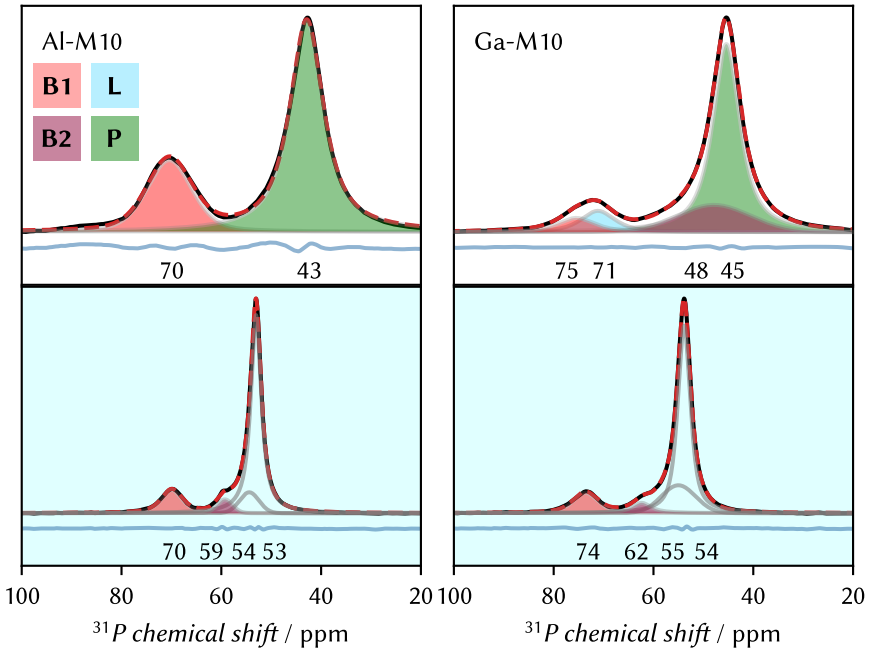

(a) T-M10 supports

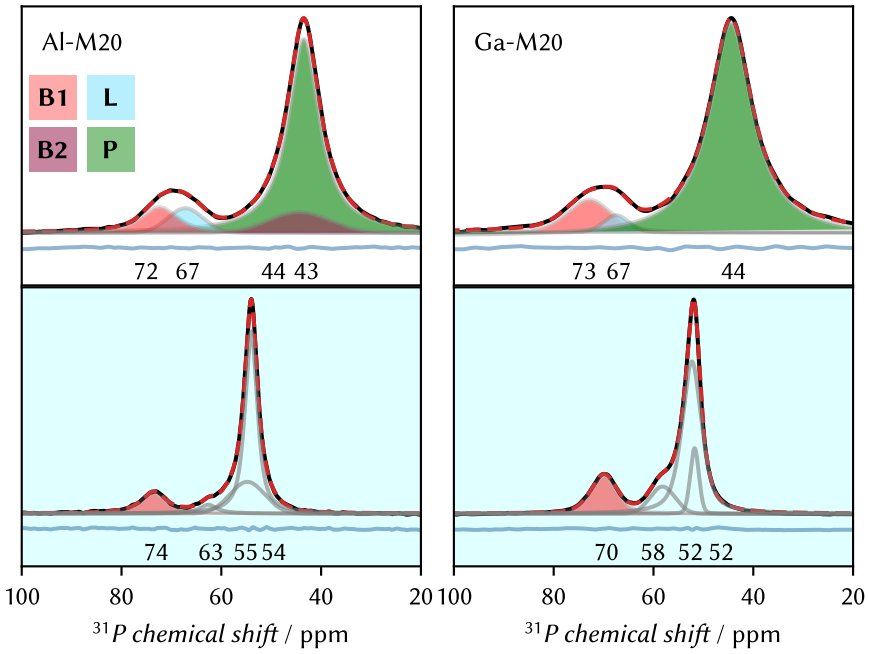

(b) T-MCM20 supports

Figure 11.6: Deconvolved ^{31}P-spectra of solvent-free, heated samples prepared according to **method 2** (white background) and the hydrated samples (blue background). Ga-MCM-41 samples were impregnated with P/Ga = 1.5 while Al-MCM-41 supports are impregnated with P/Al = 0.6. The intensities are arbitrary and not normalized.

TMPO that did not diffuse into the pores of the support. However, it remains unclear if and how many species are hidden in the large signal.

Taken together, all materials exhibit characteristic signals: two BASs – one strong (*B1*) and one weaker (*B2*) – one LAS (*L*), and either physisorbed (*P*) or crystalline (*C*) TMPO. These signal patterns are more readily observable in supports prepared using **method 1** compared to **method 2**, due to the distribution of the probe molecule on the surface.

11.3 COMMENT ON POSSIBLE $(TMPO)_2H^+$ DIMER FORMATION

To address the issue of $(TMPO)_2H^+$ dimer formation that challenges the evaluation of this method as a whole, HETCOR spectra were acquired where the dimer formation would become observable. Dimers show characteristic signatures in HETCOR spectra, as detailed in Section 4.4.3. It often depends on the impregnation method, whether dimers do form. Examples in microporous zeolites showed the formation of $(TMPO)_2H^+$ sideproducts, especially after solvent-free impregnation, which possess misleading signals that are not related to an acid site. [205, 209, 213]

Samples with different P/T ratios were assessed. HETCOR spectra of P/T = 0.6 and 1.5 were acquired and the ratio is given in the spectra. However, as demonstrated in the following section, at both ratios no signatures of $(TMPO)_2H^+$ dimers were observed.

HETCOR spectra were obtained of the solvent-based **method 1** (see Figure 11.7a) as well as of solvent-free impregnated samples of **method 2** (see Figure 11.7b). For some samples of **method 1**, the spectra do not have the required high SNR. It is directly apparent, that no spectrum contains a characteristic "parabola" [215] proving the presence of $(TMPO)_2H^+$ dimers. A TMPO-impregnated sample of the zeolite silicalite-1, that was used as a reference, however, shows characteristic crosspeaks around 40 ppm/7 to 9 ppm in ^{31}P and ^{1}H dimension, respectively (see Figure 11.9). This analogy was drawn from a study of the literature. There have been no theoretical studies on mesoporous materials to date, probably due to the difficulty of calculating amorphous structures. However, no evidence was found suggesting that the conclusions drawn from zeolitic materials cannot be applied to amorphous materials.

The direct comparison between the T-MCM-41 samples does not reveal significant differences. The most prominent signals after solvent-free impregnation **method 2** are broader in the proton dimension. The signals represent the intramolecular coupling between methyl protons and the ^{31}P nucleus. The signal is sharper in the proton dimension because of remaining solvent which still allows the methyl groups to rotate more easily. The cross peaks at acid centers (3 to 10 ppm in

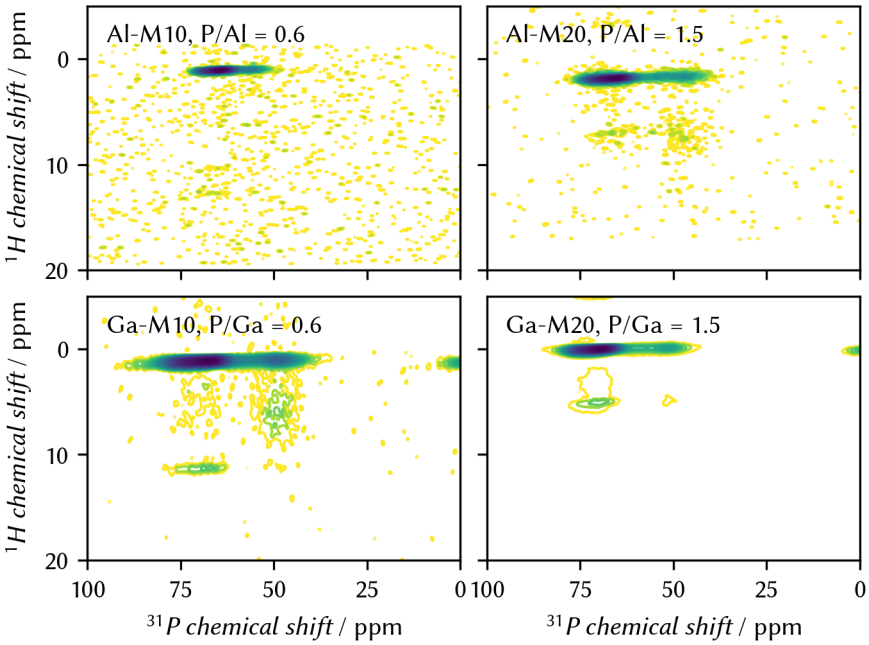

(a) Samples prepared with **method 1**. The spectra of the Al-MCM-41 samples were obtained with a lower number of accumulations than the Ga-MCM-41 samples.

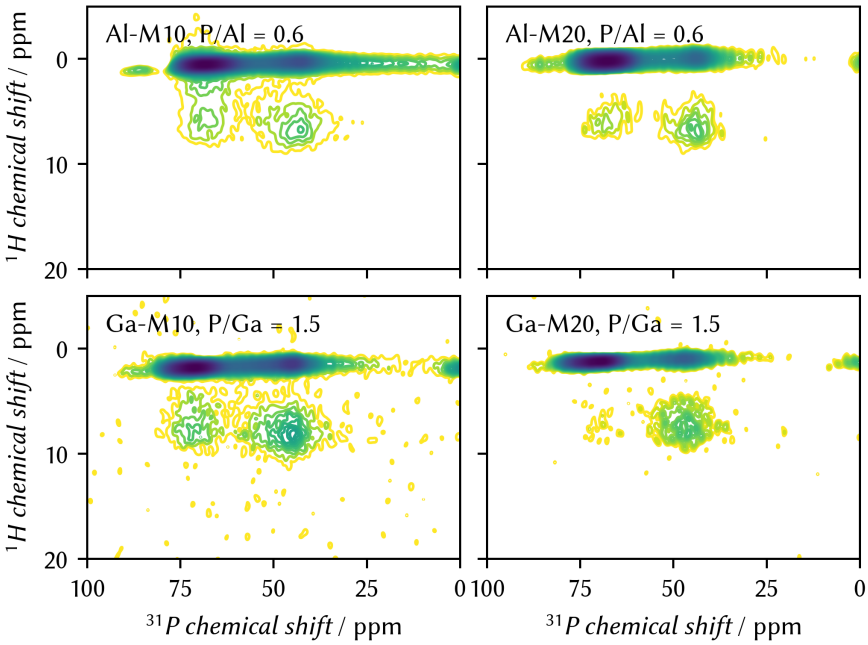

(b) Samples prepared with **method 2**.

Figure 11.7: $^1H-^{31}P$-HETCOR spectra of samples impregnated with TMPO by methods 1 and 2. The P/T ratio is indicated on the spectra. The threshold of the contour lines for representation was set to a level that allowed for distinction between the sites and an estimation of their intensity.

the ^1H dimension) are only slightly above the noise level. Most likely, these are the correlations between the surface protons involved in

the acid sites and the attached phosphorous nucleus. Since the direct proton spectra are not ranging further downfield than 10 ppm it was not expected to observe protons with a higher chemical shift. However, Ga-M10 in Figure 11.7a possesses a signal that spans between 56 and 66 ppm in the ^{31}P dimension at $\sim$ 11 ppm (^{1}H).

The protons at $\delta_{^1\mathrm{H}} = 6$ to 8 ppm show two distinct crosspeaks at $\sim$ $\delta_{^{31}\mathrm{P}} = 70$ and 48 ppm in all T-MCM-41 materials and all impregnation methods. Since the ^{31}P lowfield peak is missing at the silicalite-1 (that is lacking BASs), the lowfield signal is associated to acid sites. In all four T-MCM-41 supports, the lowfield crosspeak (^{31}P: 70 to 68 ppm / ^{1}H: 6 to 8 ppm) spans over the two signals, *B1* and *L*. The reason for this is unclear, since LAS are not directly related to protons.

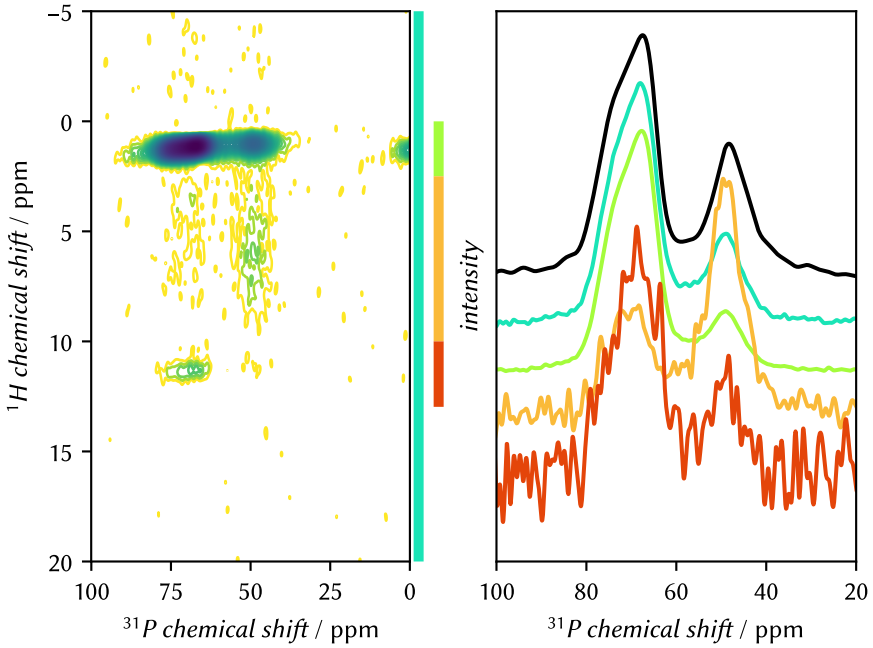

Figure 11.8: ^{1}H – ^{31}P-HETCOR spectrum of Ga-M10 impregnated with TMPO using **method 1** (left) with the experimental 1D-DP spectrum of the same sample (right, top black line), and averaged spectra along the proton dimension through the areas given by the colored lines next to the HETCOR spectrum (right). The ranges on which the average was performed are: blue: 0 to 20 ppm, green: 0 to 2.5 ppm, orange: 2.5 to 10 ppm, red: 10 to 13 ppm. The 1D spectra are normalized to their maximum.

Next, Ga-M10 impregnated with **method 1** (Figure 11.7a and Figure 11.8) is assessed in more detail. The additional HETCOR signal at 11.5 ppm (^{1}H) occurs at a relatively high proton chemical shift which is not present in proton spectra (see also the direct comparison in Figure B.9). This could belong to the broad shoulder in the direct proton spectra of the dehydrated samples, which represents all surface protons including those of acid sites. This signal is, however, not observable in the proton spectrum of the impregnated sample. In the

^{31}P dimension, the signal stretches between 56 and 57 ppm, the same chemical shift range as the HETCOR crosspeak at 7.5 ppm (^{1}H). A deconvolution of a slice between 10 to 12.5 ppm (cf. Figure B.10) is not conclusive since the SNR is low. Potentially, both signals, *B1* and *L* are present in the slice. This could mean, that due to the long contact time of 4.5 ms, TMPO on a LAS is able to do a HARTMANN-HAHN matching with a proton on a BAS. This would indicate this LAS to be in more or less close proximity to a BAS.

Despite optimized pulse parameters and an extended measurement time of 22 h, double quantum filtering experiments yielded no detectable signals. Although this suggests the absence of TMPO dimers, the method's low sensitivity prevents a conclusive determination, particularly if dimers are present in small quantities.

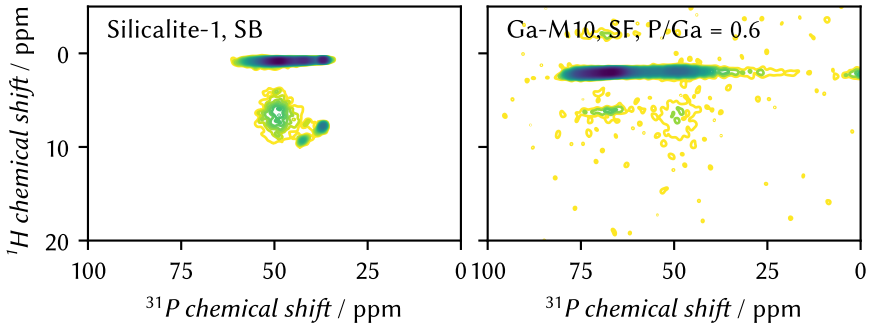

Figure 11.9: ^{1}H – ^{31}P-HETCOR spectrum of silicalite impregnated with TMPO by the solvent-based impregnation method (left) and Ga-M10 impregnated solvent-free by **method 3** (right). The loading of the silicalite was 0.5 mmol g^{-1}, the P/Ga ratio of Ga-M10 was 0.6. The threshold of the contour lines for representation was set to a level that allowed for distinction between the sites and an estimation of their intensity.

11.4 COMPARISON BETWEEN SOLVENT-BASED AND SOLVENT-FREE IMPREGNATION METHOD

In the previous chapter, no formation of dimers was detected, regardless of the impregnation method used. In this chapter, 1D spectra of these two methods are compared with each other and it is checked whether the use of solvent during preparation induces different spectra and additional interactios of support or TMPO with the solvent.

PROTON NMR SPECTRA ^{1}H NMR spectra of two series of solvent-based impregnated samples are presented in Figure 11.10. The three methyl groups of TMPO exhibit one signal at a chemical shift between 1.2 and 2.2 ppm and further proton species of the material are present as a broad signal between 1 and 7 ppm. The protons were assigned by comparison with the direct proton measurements of the supports

without a molecular probe (cf. Figure 9.4). Here, broad signals in the range above 3 ppm are assigned to proton surface species of the support materials. At the impregnated samples, sharp signals at 5.3 ppm origin from residual solvent. It seems that the solvent in the first experimental series was given enough time to completely evaporate while in the second series, this was not the case. During the preparation, the CH_2Cl_2 had evaporated before the heating phase to 165 °C, during which the solvent (b.p. 39.6 °C) is likely removed from the mesopores. Opening the SCHLENK vessel to the vacuum at high temperature aims to ensure that the gaseous CH_2Cl_2 is fully removed. At the same time, in some samples with a very low amount of acid sites, TMPO sublimated and escaped from the flask upon opening to vacuum. Despite the fact that no traces of TMPO were observed at the glass stopper of the a SCHLENK flask, it cannot be ruled out that small quantities escaped. While in zeolites, the solvent does not evaporate completely due to the smaller pore sizes [209], this does not appear to be the case in mesoporous MCM-41 materials prepared under optimal conditions. The solvent can evaporate completely, if vacuum is applied at elevated temperature. The larger mesopores allow the solvent molecules to move more easily. They are less confined in the pores and and have a lower desorption barrier.

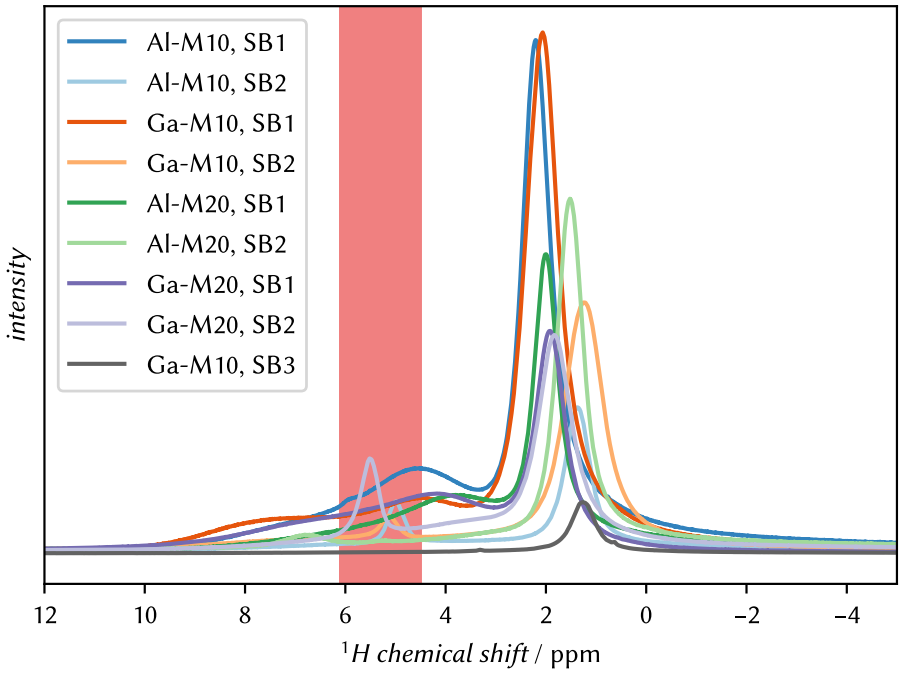

Figure 11.10: ^{1}H spectra of three series of solvent-based impregnated samples (SB1, SB2 SB3). The spectra are normalized to their number of accumulations. The region in red marks the region of the chemical shift of the solvent CH_2Cl_2 around 5.3 ppm.

PHOSPHORUS SPECTRA To address the concerns of the formation of dimers explained in Section 4.4.3, impregnation **method 2** has been performed using the vacuum line in the group of L. Mafra (Aveiro/-Portugal). The impregnation procedure is described in Section 5.2. Samples of all three impregnation methods were subsequently investigated at the same magnetic field of 9.4 T. A comparison of all spectra is shown in Figure 11.11. Here, the Ga-MCM-41 samples are impregnated with a ratio of P/Ga = 1.5 to allow for a direct comparison. The spectra of the samples prepared without solvent along **method 2** show two main peaks, of which the combined signal (*B1* + *L*) is shifted further downfield (except for Ga-M20) in comparison to the solvent-based samples. Deconvolution as shown in Figure 11.12 and Figure 11.13 reveals that for each support impregnated with both impregnation methods, the two contributions *B1* and *L* in the low-field signal possess similar chemical shifts but in different intensities. Al-M10, however, is an exception since with solvent-free preparation, the lowfield signal can be reconstructed by only one peak. The two signals *B2* and *P* in solvent-based samples are replaced by one large signal or two signals at 43 to 48 ppm. According to literature, the signals belong to physisorbed *P* or crystalline TMPO *C* and therefore do not represent TMPO on acid sites. The intense signal induces a dynamic range problem. The weakest signals are hard to detect when the strongest signal differ very much in intensity. This high intensity may mask weaker signals, potentially compromising their detection. Moreover, the signal overlap further complicates the separation and analysis of these spectral regions. Before impregnating the TMPO without solvent according to method **2**, the samples were treated at high temperature under vacuum to remove all non-inherent sites from the surface. This treatment might have removed some of the acid sites, especially BASs, [161, 256] which would in turn reduce the intensities of the ^{31}P signals of those sites. When comparing the intensity of the spectra in Figure 11.11 after normalization to the number of scans, the intensities of the signal between 60 and 80 ppm is similar except in Ga-M20 where the signal of **method 1** is much more intense, and for the sample Ga-M10 prepared with **method 3** whose intensity is lower. However, this presents only an approximation of the amounts. In three of four supports, all except Ga-M20, the spectrum of the solvent-free impregnated samples (**method 2**) shifted downfield in comparison with **method 1**. The spectrum of Ga-M10 with **method 3** in contrast has its maximum at $\sim$ 68 ppm. The two other methods possess maxima at higher chemical shifts. To investigate the support materials in further depth, the spectra were deconvolved into single signals, which is presented in Figures 11.12 and 11.13. Only one material was impregnated using the impregnation **method 3**. The amounts are P/Al = 0.6 for Al-MCM-41 and P/Ga = 1.5 for Ga-MCM-41 materials.

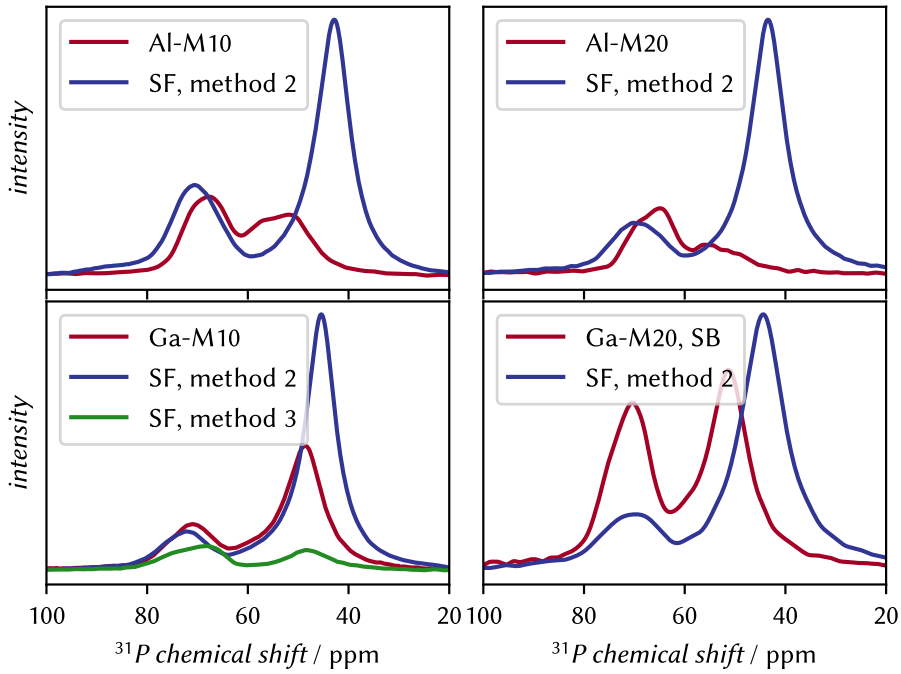

Figure 11.11: Direct comparison of ^{31}P NMR spectra of TMPO impregnated T-M10 (left) and T-M20 (right). They were impregnated using different methods: The solvent-based **method 1** (SB, red) and the solvent-free (SF) **method 2** (blue) or **3** (green). The P/T ratios are 0.6 for Al-MCM-41 and 1.5 for Ga-MCM-41 supports.

In terms of the ratio of the two overall signals, the signal (P + C) is much higher for supports impregnated with **method 2**, which again indicates the high amount of TMPO that does not interact with acid sites. Here, the different ratios of TMPO of P/Al = 0.6 and P/Ga = 1.5 do not induce a difference between Al and Ga modified materials, respectively. For the comparison of the impregnation methods, only the two lowfield signals will be considered since the P and C are not connected with the acid sites. Furthermore, the fitting of this signal is especially difficult and yielded varying intensities and shapes of signal $B2$.

Comparing measurements from all three impregnation methods, the two highfield signals $B1$ and L assigned to acid sites at a chemical shifts of 74 ± 1 ppm at Ga-MCM-41 and at 69 ± 2 ppm at Al-MCM-41 materials. Signal L varies slightly more in its chemical shift, which is between 66 and 71 ppm. An exception is Al-M10 with **method 2** that was deconvolved in just two signals with reasonable accuracy. This does not, however, constitute proof that only those two sites are present. It was furthermore observed in Ga-M10, that the intensity ratio of signals $B1$ and L is opposite in the spectra without solvent than in the spectrum with solvent. The tendency to observe a higher intensity of strong acid sites was also observed in studies on zeolites: The overall intensity is shifted towards higher chemical shifts when

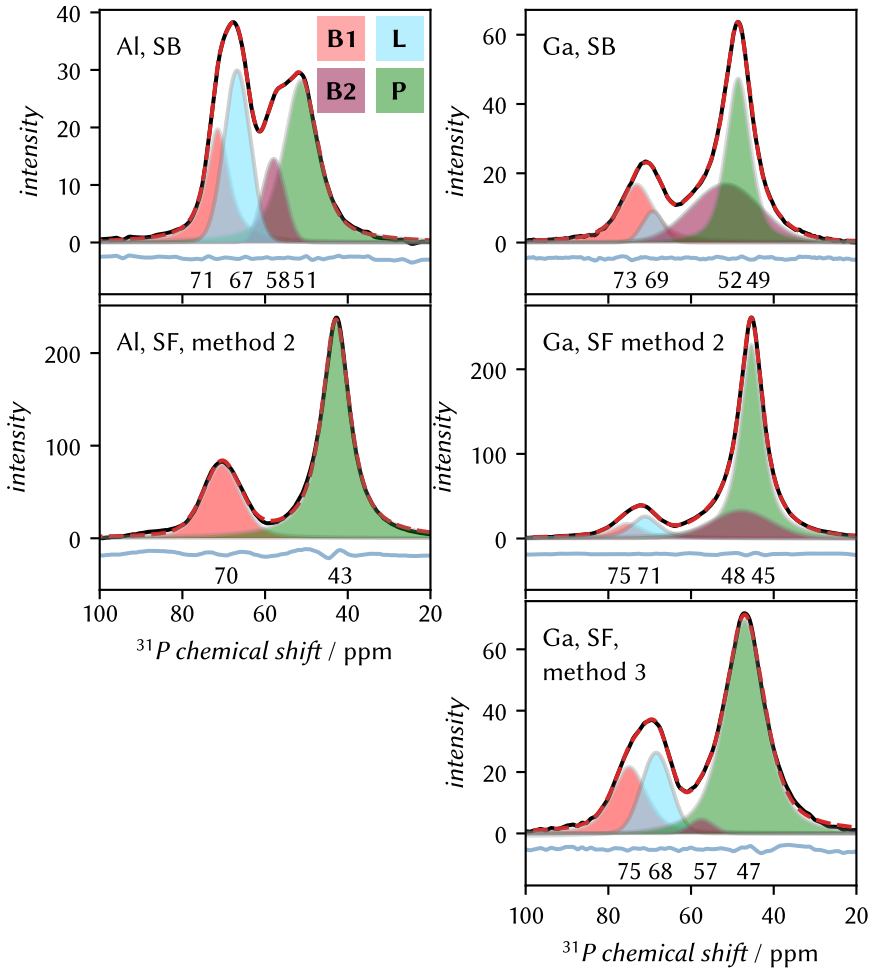

Figure 11.12: Deconvolved ^{31}P NMR spectra of T-M10 of Al (left) and Ga containing support (right) impregnated with TMPO by using three different methods (from top to bottom): solvent-based method (**method 1**, SB), solvent-free (SF) with (**method 2**), or without dehydration (**method 3**, only Ga-M10).

using a solvent based impregnation method. [208, 213] In both T-M20 materials, signal *L* is found to be smaller when solvent-free impregnation methods are employed, resulting in a shift of the whole spectrum's center of weight towards the low-field site even if the underlying chemical shifts are the same.

In the high-field part of the spectrum, the signal *B2* at 45 to 57 ppm is either broad and part of the "foot" of the signal or narrow, in both cases its inclusion in the deconvolution is necessary for a good fit of the shoulder of the large *P* signal. As described above, this signal *B2* belongs to a BAS and is most prominent for solvent-based impregnated samples, while the spectra of samples prepared by **method 2** were usually fitted either with an additional broad signal or with only one signal. The signal *C* at 43 to 45 ppm for solvent-free impregnated supports represents crystalline or physisorbed TMPO. Especially the

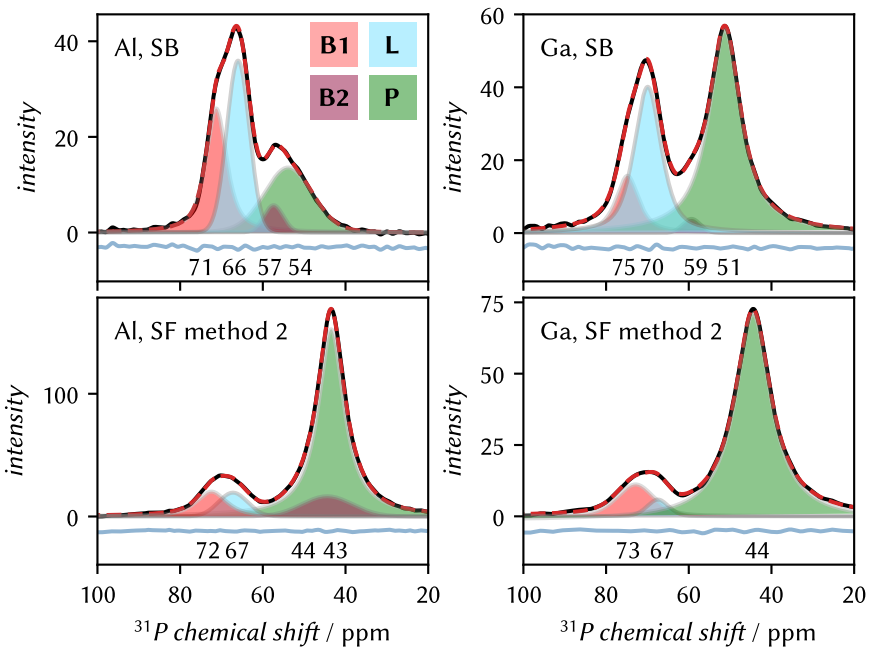

Figure 11.13: Deconvolved ^{31}P NMR spectra of T-M20 of Al (left) and Ga containing support (right) impregnated with TMPO by using two different methods (from top to bottom): solvent-based method (**method 1**, SB), solvent-free with dehydration (**method 2**, SF, H),

solvent-free impregnated supports reveal a characteristic CSA pattern of crystalline TMPO after investigation with a CP pulse sequence as shown in Figure B.5, the corresponding parameters ware given in Table B.1.

DISCUSSION The strongest acid site *B1* was observed at all three preparation methods, indicating its stability also in harsh dehydration conditions as applied in **method 2**. Therefore, this acid site is structurally defined and stable. It is unlikely that this results from a water molecule adsorbed on a LAS. In Al-M10 (**method 2**), no *L* site was observed. This discrepancy might be due to either fitting limitations or the absence of this center due to an instability against the thermal vacuum treatment. Typically, materials lose BASs upon vacuum treatment since the OH group is removed. Inversely, BASs form from LASs upon addition of water. [257] Upon dehydration, materials therefore would rather lose BASs than LASs. [94] Therefore, the absence of signal *L* cannot be deviated from adsorbents on the surface of the material. The only difference that becomes clear with the different impregnation methods is a difference in the intensities in the high-field shifted peak. But even this is rather small and can be significantly changed and adjusted by the method and the settings of fitting. The main difference to zeolites is the linewidth of the signals. Crystalline materials as zeolites consist of a repeating atomic pattern while amorphous materials

do not possess a long range order. This broadens the signal which consists of multiple overlapping signals that represent an ensemble of structurally similar but unequal sites. On zeolites ZSM-5 and USY, between five and eight sites can be assigned through deconvolution. [199, 200, 210, 213] Given the crystalline structure of USY, only one Al position is apparent, nevertheless two signals from BAS were assigned and proven by TRAPDOR measurements. [199] The second site results from mobile TMPO on different lattice sites. The MCM-41 supports contain a number of less defined sites but their signals are relatively well to assign to the acid sites with the help of hydration experiments.

11.5 COMPARISON BETWEEN SUPPORT MATERIALS

With only minor differences between the impregnation methods, the classification of the acid strengths is carried out using samples impregnated with **method 1**. For clarity, the spectra (top) together with their fitted signals (bottom) are again displayed in Figure 11.14.

TMPO impregnated siliceous MCM-41 (c(TMPO) = 0.5 mmol g^{-1}), serves as control experiment. Its single signal at 49 ppm (Figure 11.14) corresponds with literature values for physisorbed TMPO (45 ppm [222] or 48 ppm [207]) or silanols (45.7 ppm [194]). T-doped materials possess two major signals with varying intensities. The decomposition with VOIGT-lines into four signals is ambiguous due to the relatively large linewidth and the fact that the two signals in each composite signal are not well separated from each other. Therefore, it is unclear and impossible to prove, whether this is the least number of constituents. Here again, the high dynamic range possibly reduces the accuracy of the fit. An attempt of global fitting of spectra with the hydrated counterparts could potentially increase the precision of the fit, provided, that the signals remain at the same position upon treatment.

The two low field signals *B1* and *L* are generally shifted downfield in Ga-MCM-41 supports. The *B1* signals are at at 73 ppm in Ga-MCM-41 and 71 ppm in Al-MCM-41 while the *L* signals are at 67 ppm in Ga-MCM-41 and 66 to 67 ppm in Al-MCM-41.

Ga-M20 shows a different behavior than the other samples. It possesses an additional lowfield signal *SA* with a chemical shift above signal *B1*. This represents a superacid site. Signals *B1* and *L* are of the same chemical shift than in Ga-M10. While *P* is of low intensity, *B2* is missing in this spectrum. This spectrum was, however, not reproducible and other spectra revealed a similar spectrum than Ga-M10. The high field signal is often difficult to divide into two peaks *B2* and *P* or *C*. The shoulder left of the maximum can either belong to a small signal *B2* only covering the approximate width of the shoulder (compare to Al-M10), or to a broad peak that overlaps with the downfield peaks (*B1* and *L*) and thus reducing their apparent signal areas as a side effect (compare to Ga-M10). The position of *B2* ranges

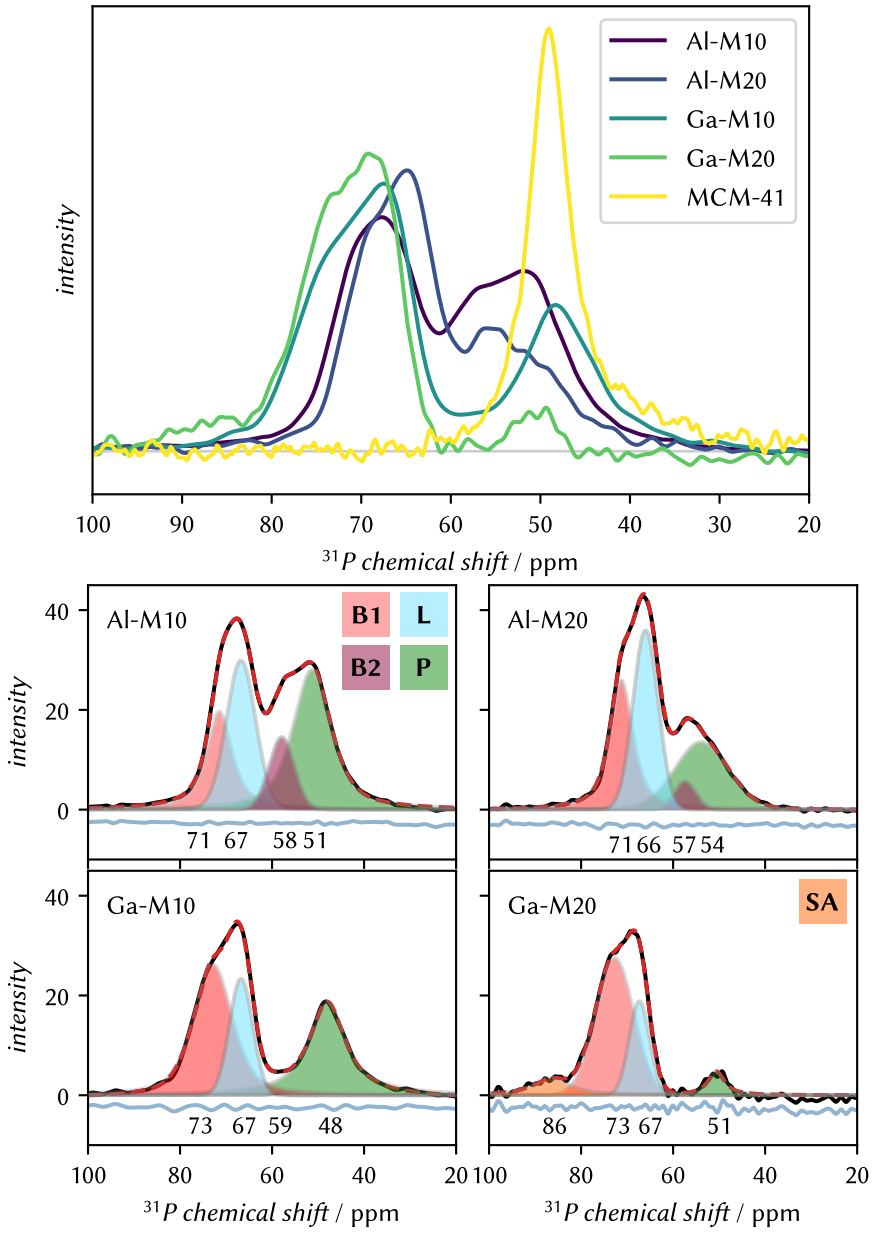

Figure 11.14: Top: ^{31}P NMR spectra of all doped supports and purely siliceous MCM-41 impregnated with TMPO. The TMPO amount is P/Al = 0.6 for all T-MCM-41 and c(TMPO) = 0.5 mmol g^{-1} for MCM-41. Bottom: ^{31}P spectra with fits of all TMPO impregnated T-MCM-41 samples using **method 1**.

from 57 to 59 ppm while *P* is from 48 to 54 ppm. Assignment of the signals to Lewis or Brønsted acid sites was possible using hydration experiments.

The solvent-based impregnation reveals stronger acid sites in Ga-MCM-41 compared to Al-MCM-41 materials, evidenced by a 2 ppm separation between their respective *B1* signals. At the same time, the signals *L* have the same shift at 67 ppm. The highest chemical shifts of the aluminium-containing supports are higher than literature (69 ppm, see Section 4.4.5), however, Ga-MCM-41 samples present an even higher chemical shift indicating a higher acidic strength than Al-containing supports. Previous studies on ammonia desorption showed that MCM-41 doped with elements Ga, Al and Fe have decreasing acid strengths Al > Ga > Fe for BASs and Ga > Al > Fe for LASs, respectively. [55]. In NH_3-TPD analyses of the materials used here, Ga-MCM-41 supports showed a higher number of stronger centers than sites of an intermediate strength. This was opposite in Al-doped samples. It is likely, that the temperature of the highest signal in the NH_3-TPD does not precisely represent the strongest acid site, since a slight increase of the negative slope of the curve can be observed around 590 °C. Thus, the results of the NH_3-TPD can be reconciled with the results of the ssNMR study. However, it is not only the type of dopant that determines the acid strength, but also the amount of it incorporated in the material. As described in Section 2.5, the increasing amount of T can either increase or decrease the acid strength. The net effect is assessed by considering the combined influence of the opposing effects. Sanderson's overall electronegativity explains the decrease of acid strength with increasing Al content. [107] This effect is most pronounced at Si/Al ratios below 10. Above this threshold, the behavior is linear with only a slight slope. Since the supports used in this work have Si/Al ratios of 10 and 20 (and the real ratios from elemental analyses are higher than that), the difference between the acid strengths caused by the amount should be negligibly small. The individual ratios determined by elemental analysis are different in both T-M10 and T-M20 supports, respectively. Both Al-MCM-41 have a lower ratio (more Al) than previously employed in the synthesis, while both Ga-MCM-41 supports have a higher ratio (less Ga). In terms of ratio, Al-M20 (Si/Al $\approx$ 13.3) and Ga-M10 (Si/Al $\approx$ 11) can be considered the most comparable. If the acid strength were solely determined by the amount of T atoms in the lattice, Al-MCM-41 should exhibit stronger acid sites than Ga-MCM-41, which contradicts the observations. Independent of their ratio, both Ga-MCM-41 supports possess higher Brønsted acidity. Therefore another factor must be responsible for the acid strength. The Ga atoms may be more exposed to the surface due to their larger atomic diameter or arrange differently in the mesoporous structure.

11.6 CO-IMPREGNATION OF NI AND TMPO

One key point in the mechanism is the role of the remaining acid sites on the surface, their interaction with the Ni sites, and their role in the catalytic cycle. It was reported, that the Ni centers need a BAS in close proximity to donate a proton to the butene reactant prior to attaching the carbenium ion to the Ni site. [1] Those acid sites were to be examined with the double impregnation. The experiments in this chapter were only performed with Ga-M10 as this is the most selective catalyst.

11.6.1 *Choice of the impregnation method*

To specifically investigate those remaining acid sites that are left after impregnation with $Ni(Cp)_2$, TMPO was applied onto the Ni impregnated support that formed the active catalyst. Given that the two species, $Ni(Cp)_2$ and TMPO, exhibit contrasting polarities, they are unable to dissolve in the same solvent. Therefore, when the $Ni(Cp)_2$ is applied using pentane (irrespective of whether it directly binds to an acid site or only physisorbs on the surface), it will not be dissolved by the solvent CH_2Cl_2 which is used for the application of TMPO.

As this method has not been reported previously, the following considerations were made to find a suitable impregnation method.

- The application of vacuum changes the oxidation state from Ni^{II} to Ni^{I} [3] and could lead to further reduction and the formation of Ni^0-clusters
- CH_2Cl_2 should be completely removed in order to ensure proper attachment of TMPO to the surface of the support material rather than remaining in solution and leading to misinterpretation

In light of the aforementioned considerations, three variants of the $Ni(Cp)_2$-TMPO double impregnation method were conducted with the objective to identify a process that would result in the retention of Ni sites and a minimal residual solvent content. With those methods, the process of solvent evaporation after the application of TMPO is varied.

1. Evaporation of solvent CH_2Cl_2 is conducted by flowing Ar through the SCHLENK tube. The stopper was slightly opened under positive Ar pressure to allow for a flow.
2. Purging between vacuum and Ar until the solvent evaporated completely.
3. Usual procedure for the solvent-based TMPO impregnation with evaporation of the solvent under vacuum and heating the sample to 165 °C.

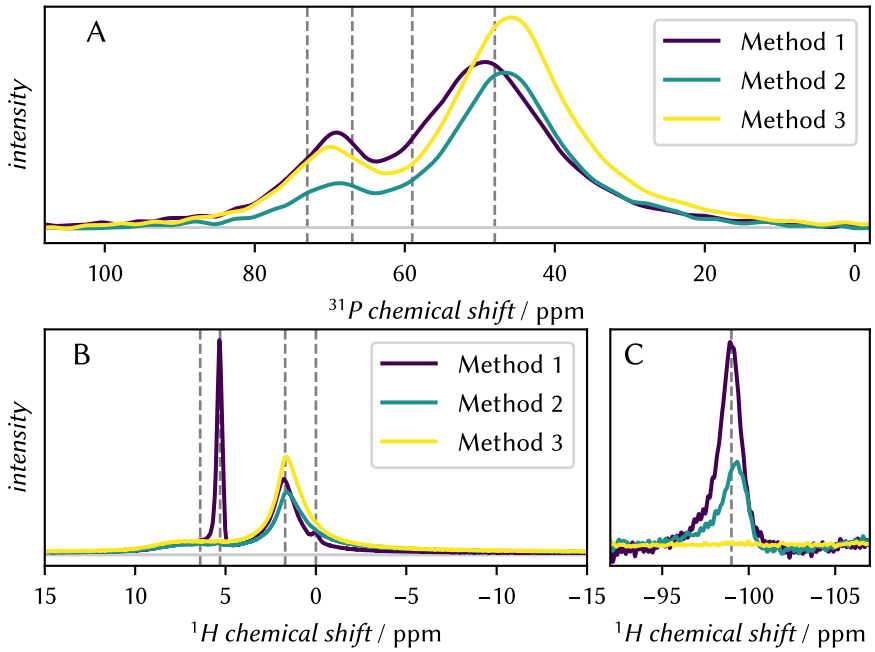

Figure 11.15: Spectra of samples prepared with three different impregnation methods. A: ^{31}P spectra. The lines are at 73, 67 and 48 ppm according to the single signals in Ga-M10 (Figure 11.14). B: ^{1}H spectra with slow repetition time, C: ^{1}H spectra with fast repetition time, focused on the paramagnetic signal at −99 ppm. The vertical lines are at −99, 0, 1.7, 5.3 and 6.4 ppm. Note, that the methods correspond to the solvent evaporations methods of this section. For details, see the text.

The methods were evaluated by ^{1}H and ^{31}P NMR spectroscopy as presented in Figure 11.15. The ^{31}P spectra in Figure 11.15 A are relatively similar. There are differences in the intensity of the spectra, but there is no big deviation in chemical shifts. The intensity of the lowfield signal of method 2 is the smallest. This peak represents the position of TMPO adsorbed on acid sites. First and foremost, the signal's intensity is reduced if the TMPO molecule is within the paramagnetic sphere around Ni. Additionally, the intensity might slightly vary due to slightly different amounts of sample and packing of the rotors. The different treatment probably also influenced how the nickel is arranged on the surface. It could have formed a cluster or migrated to other surface positions. Proton spectra in Figure 11.15 B were recorded with an inter-scan delay of 3 s to detect residual solvent signals. The dominant peak at ∼1.7 ppm corresponds to the TMPO methyl groups. In method 1, CH_2Cl_2 appears as a prominent sharp signal at 5.3 ppm (Lit: 5.443 ppm [258]), accompanied by two minor signals at 6.4 ppm and 0.0 ppm (cf. Figure B.11 for a zoomed version). Method 2 exhibits two small downfield signals at 6.4 and 5.3 ppm adjacent to the methyl peak, matching the chemical shifts observed in method 1, though with notably reduced CH_2Cl_2 intensity. Method 3 shows only trace amounts

of CH_2Cl_2, evidenced by a minimal signal at its characteristic position. For the characterization of the species, the proton shifts of the potentially involved species were considered. Proton signals of pentane are at 0.8 and 1.3 ppm while the three signals of cyclopentadiene (Cp) are at 6.43, 6.3 and 2.8 ppm. The observed lowfield signal at 6.4 ppm likely originates from Cp, which is released when $Ni(Cp)_2$ attaches on a surface BAS. During this process, a Cp^- anion abstracts a proton from a BAS and desorbs into solution. Both this Cp and residual CH_2Cl_2, appear to persist through the short vacuum cycles. While the signal at 0.0 ppm does not align well with chemical shifts of pentane, its disappearance upon sample evacuation suggests a connection to the solvent, potentially experiencing a slight paramagnetic shift. Part C of Figure 11.15 shows the high-field region of the proton spectrum, where signals appear after successful bond formation of $Ni(Cp)_2$ to the surface of the support. Similar to the proton spectra acquired after Ni impregnation (see Chapter 10), the repetition time between two accumulations was only 10 ms to suppress the solvent signal and to better observe the paramagnetically shifted signal at −99 ppm. Due to the acquisition in a larger rotor (outer diameter was 4 mm instead of 1.3 mm) the MAS frequency was slower (12 kHz instead of 20 kHz). The decreased gas flow friction results in a lower temperature, causing a downfield shift of the signals, similar to the behavior shown in Figure 10.4.The sample prepared using method 3 shows no detectable signal, suggesting that Ni may have detached from the surface. Method 1 produced the most intense signal, while method 2 yielded approximately half that intensity.

Combining all the results of the three spectra, method 2 was chosen to continue with. This is due to the minimal amount of solvent that is observable in the proton spectra. At the same time, the proton signal at −99 ppm is still present, indicating the best possible trade-of between the removal of solvent and the Ni adsorbed on the surface.

11.6.2 *Impregnation with different amounts of Ni*

The support material Ga-M10 was impregnated with an increasing amount of $Ni(Cp)_2$ of 0.0 %, 0.2 %, 0.6 % and 1.2 %. It was aimed to observe differences in the spectra with increasing Ni content to pinpoint the sites that are closest to the reactive Ni centers.

The measurements were performed using two different inter-scan delay times: a standard inter-scan delay times of 10 s and a rapid delay of only 2.8 ms. This approach allows for the detection of sites with short relaxation times, which may indicate proximity to nickel centers. The signals were deconvolved in both cases and are presented in Figure 11.16. The intensity of the signal *B1* at 73 to 74 ppm significantly decreases with increasing amount of Ni on the surface. At the same time, the signal *L* at 69 ppm does not seem to vary very much. The

signal of the physisorbed TMPO at about 49 ppm decreases in its intensity as well but gets broader at the same time.

In rapid acquisition measurements, which preferentially detect species with fast relaxation rates, the signal intensities show minimal variation across different nickel loadings (low, medium, and high).The spectra reveal only two remaining signals: The LAS signal observed at 65 and 69 ppm and the physisorbed TMPO signal *P*. The BAS signals are not detectable in these measurements. Notably, the spectral patterns remain consistent regardless of nickel's presence, indicating that these signals originate from fast-relaxing species that are not influenced by nickel content. This indicates, that TMPO on BASs relaxes more slowly than the repetition time of 2.8 ms in this measurement. Thus, only spectra acquired using long relaxation times were used for the evaluation of the areas.

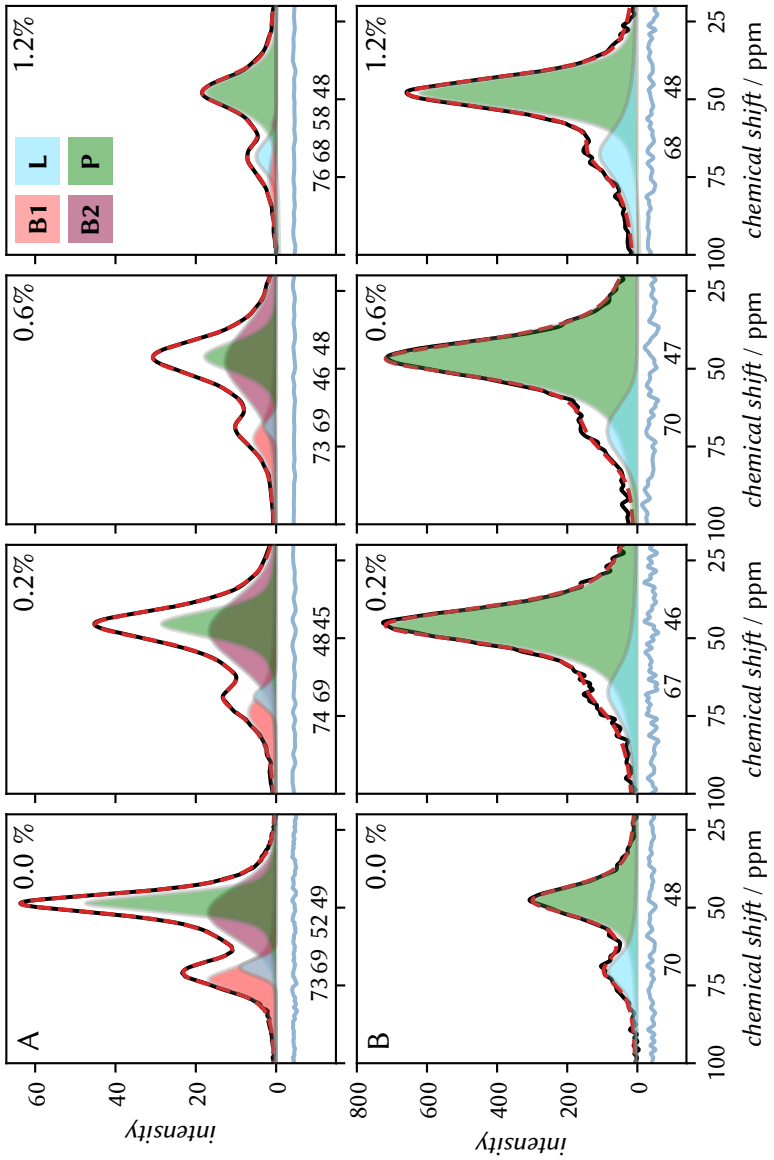

Figure 11.16: Deconvolved 31P-NMR spectra of slow (A) and fast (B) measurements of Ni and TMPO impregnated samples. The samples contain Ni amounts of 0.0, 0.2, 0.6 and 1.2 % from left to right. The spectra from the lower row stem from the same sample as the spectra in the upper row but show rapid measurements to observe fast relaxing species.

The areas of the deconvolved signals of the slow measurements are shown in Figure 11.17. It is especially apparent for *B1* at 72 ppm and *P* at 49 ppm that the signals' areas decrease with increasing amount of Ni. There can be two scenarios explaining the decrease: (i) Ni itself occupies the BASs and therefore TMPO cannot attach to this center anymore. Therefore, no signal of TMPO on that site can be present. (ii) TMPO on the BASs is very close to nickel-containing sites which reduces the intensity of the signals due to the induced rapid relaxation caused by a nearby paramagnetic center. From literature and previous

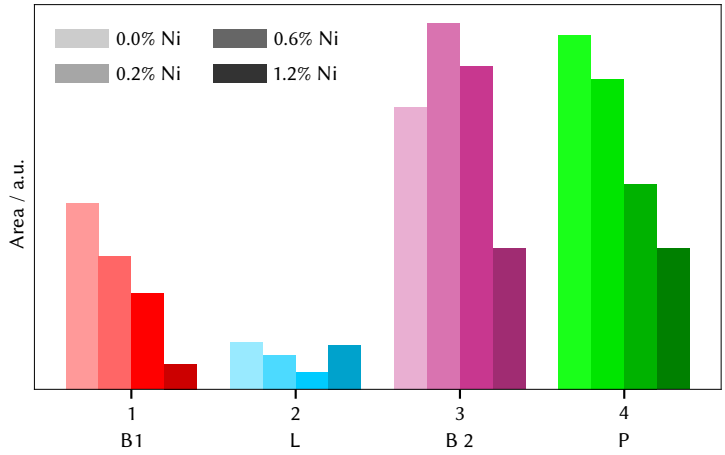

Figure 11.17: Areas of the deconvolved peaks of Ga-M10 with varying amount of nickel and the experiments with normal inter-scan delay of 10 s. The shade of each bar corresponds to the amount of nickel, as indicated in the legend.

measurements, it did become clear, that Ni binds selectively to BASs. From to the low amount of Ni (0.6 wt%) there are 0.055 atoms/nm^2 (or 1 atom every 18.18 nm^2) present on the surface of Ga-M10 while the amount of TMPO is 0.31 molecules/nm^2. If all Ga atoms would be exposed to the surface as acid centers, there would be 0.51 atoms/nm^2. In reality, a part of the Ga atoms is within the walls, and not exposed to the surface. However, this amount is neglected for this rough estimation. If all Ga were exposed, Ni covers around 10 % of the acid centers, while TMPO is present on 60 % of the acid sites. With a kinetic diameter of 0.55 nm, TMPO covers approximately 7.3 % of the surface area. The radius of a "blind sphere" around a paramagnetic Mn^{2+} ($3\,d^5$) is 0.7 nm when measured with ^{31}P nuclei. [259] For Ni^+ ($4\,s^2\,3\,d^7$), the presence of spin-orbit coupling leads to faster electron relaxation, which should result in a smaller blind sphere radius. The half mean distance[1] between two Ni centers is 2.41 nm. It is therefore apparent that the blind sphere around a Ni atom is smaller than the distance between two Ni centers on the surface, meaning that not the whole surface area is influenced by an environment that induces

1 The half mean distance is used to allow an easier comparison with the radius of the blind sphere.

strong relaxation. The successful measurement of a spectrum supports this assumption, as a fully bleaching surface would prevent spectral measurement. This approximation was performed assuming an equal distribution of the atoms or molecules on the surface. This is not necessarily the case and particularly two acid centers of different type could be next to each other. To get insights into the distance distribution between two Ni centers, distance measurements could be elaborated in future work by developing recoupling NMR methods (REDOR, symmetry based REDOR or resonance-echo saturation-pulse double-resonance (RESPDOR)) between ^{27}Al of the support and ^{31}P of TMPO and applying them to supports with and without impregnation with Ni.

12

THE BIGGER PICTURE: DISCUSSION OF RESULTS AND MECHANISTIC IMPLICATIONS

12.1 RESULTS AND THEIR IMPLICATIONS

The rational design of heterogeneous catalysts remains one of the most compelling challenges in modern materials chemistry and it is particularly important for reactions of industrial relevance. While crystalline zeolites have traditionally dominated acid-catalyzed reactions and are well characterized, the emergence of amorphous, mesoporous materials like MCM-41 is beneficial since they allow for a better material transport within their larger pores. The characterization of acid sites in these materials presents both unique opportunities and distinct analytical challenges that need to be addressed to develop an understanding of structure-property relationships.

NMR in general is a perfect tool to probe the local environment of acid sites and complements other techniques such as Pyr-IR and TPD. A repertoire of NMR methods was elaborated, tested and evaluated to determine whether it can provide information about the structure and properties of the acid centers. Different approaches were tested: Direct detection of the NMR active nuclei contained in the material (^{29}Si, ^{27}Al, ^{1}H), and experiments on a ^{31}P containing probe molecule that is sensitive for acid sites. The coordination of Ni atoms was targeted and their preference to attach to sites with elevated Si or T content was evaluated. Both atom types participate in acid site formation.

From one-dimensional NMR of the different elements contained in the material, the proton measurements provided some insights. The amorphous nature of the mesoporous material MCM-41 broadens all signals and makes assignment of specific sites more difficult. Proton spectra look very different depending on the heating treatment the samples underwent. The signal is very broad and stretches over the known range of acid sites. In ^{1}H – ^{31}P-HETCOR spectra of TMPO impregnated supports, however, distinct signals appeared in the proton dimension at 7.5 ppm and in one case additionally at 11 ppm which were not that distinctly observed in the proton spectrum. Those signals originate from potentially reactive acid sites that were revealed by probe molecules selectively attaching to them.

After impregnation with $Ni(Cp)_2$, only support materials with BASs possess a proton signal at -105 ppm which represents protons of the remaining Cp ring of the remaining $[Ni(Cp)]^+$ species. The absence of

this signal on surfaces containing only silanols or LASs indicates that BASs play a crucial role in anchoring Ni to the surface.

Through impregnation with TMPO and deconvolution of the ^{31}P spectra, the strength and the type of acid sites was determined. Overall, three sites were distinguished: two BASs and one LAS. This was possible since no formation of $(TMPO)_2H^+$ that has been observed in HETCOR spectra.

This methodological transition of the impregnation method with TMPO from zeolites to mesoporous materials has revealed unexpected advantages in the characterization of acid sites. The traditional TMPO probe molecule approach, while well-established in literature for zeolites, has historically been complicated by solvent-related challenges when using CH_2Cl_2. Specifically, incomplete solvent removal often led to the formation of $(TMPO)_2H^+$ species, resulting in misleading spectroscopic signatures. However, the wider pore architecture of mesoporous materials effectively resolves this limitation. Their larger pore diameters allow for more efficient solvent evaporation, thereby eliminating the risk of artificial dimer formation. Notably, even when using high TMPO loadings which would typically promote dimer formation in conventional systems, no spectroscopic evidence of TMPO dimers was observed[1]. This finding does not only simplify the experimental procedure but also enhances the reliability of acid site characterization in mesoporous materials and generally allows for quantification. However, since the signals on the amorphous materials are relatively broad, deconvolution of the spectrum to individual signals is ambiguous which in turn hinders a reliable quantification. Potentially, a global fitting procedure involving CP and DP spectra or spectra from fresh and hydrated samples could promote a more certain assignment of the acid sites. This is due to the greater number of independent data points for the same number of parameters, as different signals are more or less pronounced in both pairs of spectra.

From the decomposition of the ^{31}P spectra, Ga-MCM-41 exhibits stronger BASs than Al-MCM-41, with the acid strength being independent of the T^{3+} content in the siliceous MCM-41 lattice. Additionally, one type of a strong LAS is present, which probably participates in the catalytic reaction by stabilizing the intermediate. Assessing the remaining acid sites after Ni impregnation reveals a decreasing intensity of the BAS *B1* signal and the signal of physisorbed TMPO with increasing amount of Ni, while the other two sites, *B2* and *L*, do not show this trend so clearly. This again confirms the attachment of Ni on BASs since the presence of Ni decreases the signal through occupation of the sites as well as by its paramagnetic bleaching effect. This experiment opens the space for developing recoupling methods to assess distance relationships between the paramagnetic Ni center and the framework atoms Si, Al, and potentially Ga, and H (cf. Section 12.2.1).

1 and proving the inexistence is philosophically impossible.

In catalytic reaction of butene dimerization, a high number of BASs correlates with a higher product fraction of branched octenes. From the product formation ratio, it is likely that the carbenium ion mechanism is predominant in the case of Ni/Al-MCM-41 catalysts. Ni/Ga-MCM-41 are more selective towards the desired methylheptene and possess a lower number of BASs. Investigation with NH_3-TPD and Pyr-IR showed that Ga-MCM-41 supports overall possess a lower number of BASs, at the same time, the number of the strong type of acid centers is higher in Ga-MCM-41 than in Al-MCM-41 materials.

TMPO probe molecule measurements revealed that the strongest acid sites are BASs, with Ga-doped materials exhibiting higher chemical shifts, indicating increased acid strength. Notably, regardless of the extent of Si site substitution by T^{3+}, both Ga-M10 and Ga-M20 supports demonstrated consistently stronger acid sites than in their Al-doped counterparts. This observation supports the theory that catalytic activity primarily stems from a few potent active centers. [70, 77]

Ni-free T-M10 supports displayed minimal activity and are non-selective for this reaction, conclusively demonstrating that free Lewis Ga^{3+}/Al^{3+} sites do not significantly contribute to the reaction mechanism. A recent study [3], further corroborated by ^{1}H-ssNMR experiments of Ni-impregnated supports in this study, confirmed the critical role of BASs in stabilizing Ni single sites. Higher BAS strength of the support enhances the Lewis acidity of Ni centers, potentially facilitating more efficient butene attachment to active sites.

A high amount of BASs does not contribute to enhanced activity of the catalyst, neither did the performance increase. However, due to a low amount Ni single sites, it is likely that potential positive stabilizing effects of BASs next to Ni sites will not be apparent in the distribution of reaction products.

The study also identified strong LASs on the surface, although their precise impact on the reaction mechanism remains ambiguous. An intriguing possibility emerged: the formation of superacid sites on Ga-M20 might result from a synergistic interaction between Brønsted and Lewis acid sites. However, the specific conditions and mechanisms governing these synergies could not be definitively identified.

In summary, the characterization of acid sites in amorphous, mesoporous MCM-41 materials has revealed distinct advantages over traditional zeolite systems, particularly in the reliable application of TMPO probe molecules due to enhanced solvent removal in larger pores. While Ga-MCM-41 exhibits stronger BASs than Al-MCM-41, the presence of BASs proves crucial for anchoring Ni single sites, albeit a higher quantity of BAS does not necessarily improve catalytic performance. The study also suggests potential synergistic effects between strong BASs and LASs, though the exact mechanism of catalysis requires further investigation.

12.2 NEW AND EMERGING PROBLEMS

From the approaches applied in this work, further aspects became clear, that can help to approach the answer to the question "Where is the Ni?". Those questions could be addressed in future projects with the foundation presented in this work.

12.2.1 *Establish distance relations between acid sites and TMPO*

Can the distance between the acid site of the support and the TMPO probe molecule report on exposed acid sites? How does the distance distribution change after impregnation with $Ni(Cp)_2$ and can we learn something about the most reactive sites?

Correlation spectroscopy is able to extract distance information between support lattice atoms and probe molecules. KAO AND GREY [68] showed that they could extract distances between probe molecules and the ^{27}Al nucleus. The number of remaining acid sites on the surface after impregnation with $Ni(Cp)_2$ is important for the selectivity of the dimerization reaction. Recoupling MAS-NMR methods, namely REDOR, symmetry based REDOR, or RESPDOR allow to draw conclusions about distances between ^{27}Al of the support and ^{31}P of the probe molecule TMPO. Impregnation with paramagnetic Ni adds complexity to the system and perturbs effective recoupling. This indicates the close distance to the observed atom. The first step is to find out whether these methods are applicable at all. Secondly, methods for measurement and evaluation need to be explored and established based on existing tools (e.g. [260]).

12.2.2 *In-situ spectroscopy of catalyst with butene*

Is the observation of the catalyst "in action" possible? Can we observe the position of labeled carbons in the products and draw conclusions on the reaction pathway(s)?

In this experiment series, butene will be added to the Ni impregnated catalyst into the rotor. The interaction of butene with the catalyst will then monitored by NMR. A first attempt will happen under normal pressure. Butene will be simply given into a SCHLENK tube containing the Ni impregnated support materials. This mixture will be filled in a rotor under inert atmosphere. The amount of butene contained in the pores could be enough to observe the interaction between the gas and the surface. If necessary, the reaction can be activated by increasing the temperature within the NMR spectrometer. In catalysis, the reaction is conducted at 80 °C. This temperature can be achieved in the ssNMR probehead as well. In a next step, a vacuum line will be set up to seal the rotor in a butene saturated atmosphere without contact with other gases. However, only low overpressure can

be applied, otherwise there will be a high risk that the rotor cap in the spectrometer will be pushed out of the rotor by the overpressure and cause a rotor crash.

Furthermore, labeled 1-butene in positions C_1 or C_2 could be used to additionally monitor their positions in the products, which enables to draw conclusions on the isomerization of butenes and the product formation mechanism. The attachment position of the C_4 molecule to the Ni single site and any preceding butene isomerization can be determined through analysis of the two ^{13}C nuclei distribution in the products. If the reaction proves unsuccessful within the ssNMR rotor, the reaction can be conducted *ex-situ* and the labeled products are then analyzed.

12.2.3 *Optimize Ga-NMR*

Which NMR techniques are needed to obtain high quality Ga spectra to characterize Ga lattice sites?

Pulse sequences can be optimized on Ga-MCM-41 support materials. The ^{71}Ga nucleus is preferred due to its lower quadrupolar moment resulting in a smaller linewidth. This, in combination with the recoupling sequences mentioned above, could enable the investigation of the cause of the higher acidity. Potentially, the exposition of Ga sites varies significantly from Al sites due to their larger atomic diameter. Increasing sensitivity for Ga could be attempted by the use of a rotor synchronized Carr-Purcell-Meiboom-Gill (CPMG) pulse sequence.

12.2.4 *Application of dynamic nuclear polarization*

Is dynamic nuclear polarization (DNP) able to enhance the surface species and does it allow for site-specific investigation of distinct acid sites?

Surface enhanced NMR by DNP (DNP-SENS) is a great tool to enhance the NMR signals of surface sites as demonstrated in literature, e.g. in refs. [261–263]. The application of paramagnetic polarizing agents on the surface specifically enhances exposed sites and allows e.g. for the detection of ^{17}O NMR spectra at natural abundance. One can also think of enhancing the signals of TMPO impregnated on acid sites, however, the solvent for the polarizing agent needs to be carefully chosen to neither detach TMPO from the surface nor modify the surface acid sites.

12.2.5 *Use of Ni in different oxidation states*

What are the spectroscopic signatures of sites related to Ni in a different oxidation state?

Previous studies have focused only on Ni^{2+}. By using $Ni(Cp)_2$, up to three proton signals were apparent exhibiting paramagnetic shifts below -50 ppm. The signal at -104 ppm is believed to originate from the Cp protons of Ni^{+}. Different Ni oxidation states would likely result in distinct chemical shifts for nearby protons. This hypothesis could be verified through a systematic approach:

- Individual measurements of $Ni(Cp)_2$ and Ni(COD)
- Measurements of their mixture, both with and without support

Furthermore, additional Ni precursors (e.g. NiO) could be used to investigate surface sites that might appear at more extreme shifts ($\delta < -260$ ppm).

12.2.6 *Development of a global fitting procedure*

Is it possible to assign acid sites signatures with greater precision and reliability?

The deconvolution of the spectra of TMPO impregnated samples remains somewhat ambiguous and the solution found here is not definitive. To improve the quality, spectra before and after hydration can be included in a global fitting, as well as spectra recorded via CP. The variables and the overall stability of this method need to be assessed. Therefore, software needs to be written or existing algorithms need to be adapted. They could be based on the *lmfit* package [264] in Python. This potentially increases the precision of the signal assignment to their chemical shifts and may further distinguish the acid sites of different strengths.

12.3 CONCLUSION

This dissertation has yielded several novel findings that will be succinctly summarized:

- BASs are definitely necessary to attach Ni to the surface. Their additional necessity for the reaction itself could not be verified.
- At least four different acid sites are present on all four supports: two BASs – one strong (*B1*) and one weaker (*B2*) – one LAS (*L*), and either physisorbed (*P*) or crystalline (*C*) TMPO. Additionally, a superacid site *SA* was observed once on Ga-M20 which possesses a mediocre selectivity. Especially the *B1* and the *L* are likely to be involved into the dimerization mechanism in conjunction with the Ni single site.
- Impregnation with TMPO does not pose the same issues in mesoporous materials as in zeolites. Since no $(TMPO)_2H^{+}$ dimers were

observed, the simpler impregnation method using the solvent CH_2Cl_2 can be used for the sample preparation.

- The double impregnation with Ni and TMPO presents an decreasing area of the signals *B1* and *P* with increasing Ni content, indicating the direct influence of Ni to those sites.

Taken together, ssNMR has proven to be a valuable technique to deepen our understanding of the structure-property relationship of ASA materials and the mechanism of butene dimerization. This work establishes the fundamental importance of strong BASs in selective butene dimerization and demonstrates the unique advantages of TMPO-based ssNMR characterization for mesoporous catalysts. In conjunction with the aforementioned advanced spectroscopic approaches, the results enable to bridge the current knowledge gap between catalyst structure and function, ultimately enabling the rational design of more selective and efficient catalysts for industrial alkene oligomerization processes.

BIBLIOGRAPHY

[1] J. Rabeah, J. Radnik, V. Briois, D. Maschmeyer, G. Stochniol, S. Peitz, H. Reeker, C. La Fontaine, A. Brückner, *ACS Catalysis* **2016**, *6*, 8224–8228.

[2] M. Golombok, J. De Bruijn, *Industrial and Engineering Chemistry Research* **2000**, *39*, 267–271.

[3] T. H. Vuong, N. Rockstroh, U. Bentrup, J. Rabeah, J. Knossalla, S. Peitz, R. Franke, A. Brückner, *ACS Catalysis* **2021**, *11*, 3541–3552.

[4] A. Brückner, U. Bentrup, H. Zanthoff, D. Maschmeyer, *Journal of Catalysis* **2009**, *266*, 120–128.

[5] T. H. Vuong, M. Schröder, J. Rabeah, C. Kubis, R. Eckelt, H. Atia, B. Corzilius, J. Knossalla, R. Franke, A. Brückner, "Role of Acidic Properties of T-modified MCM-41 for Ni-catalyzed Butene Dimerization Revealed by Operando EPR, In Situ FTIR Spectroscopy and Solid-State NMR," in preparation, **2024**.

[6] F. Alscher, F. Nadolny, H. Frenzel, J. Knossalla, S. Peitz, E. Borovinskaya, C. Breitkopf, R. Franke, W. Reschetilowski, *Catalysis Science and Technology* **2019**, *9*, 2456–2468.

[7] F. Nadolny, B. Hannebauer, F. Alscher, S. Peitz, W. Reschetilowski, R. Franke, *Journal of Catalysis* **2018**, *367*, 81–94.

[8] F. Nadolny, U. Bentrup, N. Rockstroh, F. Alscher, W. Reschetilowski, S. Peitz, R. Franke, A. Brückner, *Catalysis Science & Technology* **2021**, *11*, 4732–4740.

[9] F. Nadolny, F. Alscher, S. Peitz, E. Borovinskaya, R. Franke, W. Reschetilowski, *Catalysts* **2020**, *10*, 1487.

[10] A. Ehrmaier, Y. Liu, S. Peitz, A. Jentys, Y.-H. C. Chin, M. Sanchez-Sanchez, R. Bermejo-Deval, J. Lercher, *ACS Catalysis* **2019**, *9*, 315–324.

[11] A. Ehrmaier, L. Löbbert, M. Sanchez-Sanchez, R. Bermejo-Deval, J. Lercher, *ChemCatChem* **2020**, *12*, 3705–3711.

[12] G. Podrebarac, F. Ng, G. Rempel, *Applied Catalysis A: General* **1996**, *147*, 159–173.

[13] D. Kiessling, G. Wendt, K. Hagenau, R. Schoellner, *Applied Catalysis* **1991**, *71*, 69–78.

[14] M. L. Sarazen, E. Iglesia, *Proceedings of the National Academy of Sciences* **2017**, *114*, E3900–E3908.

[15] J. W. Niemantsverdriet in *Spectroscopy in Catalysis*, John Wiley & Sons, Ltd, **2007**, pp. 1–10.

[16] J. M. Thomas, C. R. A. Catlow in *Progress in Inorganic Chemistry, Vol. 35*, John Wiley & Sons, Ltd, **1987**, pp. 1–49.

[17] G. Gottardi, E. Galli in *Natural Zeolites*, (Eds.: G. Gottardi, E. Galli), Minerals and Rocks, Springer, Berlin, Heidelberg, **1985**, pp. 1–34.

[18] Z. A. ALOthman, *Materials* **2012**, *5*, 2874–2902.

[19] J. Xu, Q. Wang, S. Li, F. Deng, *Solid-State NMR in Zeolite Catalysis*, Springer Singapore, Singapore, **2019**.

[20] D. W. Breck, *Zeolite Molecular Sieves: Structure, Chemistry, and Use*, Wiley, New York, **1973**, 771 pp.

[21] *Zeolites in Industrial Separation and Catalysis*, 1st ed., (Ed.: S. Kulprathipanja), Wiley, **2010**.

[22] M. E. Davis, C. Saldarriaga, C. Montes, J. Garces, C. Crowdert, *Nature* **1988**, *331*, 698–699.

[23] V. Chiola, J. E. Ritsko, C. D. Vanderpool (Sylvania Electric Products Inc), *US Pat.*, 3556725A, **1971**.

[24] T. Yanagisawa, T. Shimizu, K. Kuroda, C. Kato, *Bulletin of the Chemical Society of Japan* **1990**, *63*, 988–992.

[25] C. T. Kresge, M. E. Leonowicz, W. J. Roth, J. C. Vartuli, J. S. Beck, *Nature* **1992**, *359*, 710–712.

[26] C. T. Kresge, M. E. Leonowicz, W. J. Roth, J. C. Vartuli (Mobil Oil Corp), *US Pat.*, 5098684A, **1992**.

[27] C. T. Kresge, M. E. Leonowicz, W. J. Roth, J. C. Vartuli (Mobil Oil Corp), *US Pat.*, 5102643A, **1992**.

[28] J. S. Beck, C. T. Chu, I. D. Johnson, C. T. Kresge, M. E. Leonowicz, W. J. Roth, J. C. Vartuli (Mobil Oil Corp), *US Pat.*, 5108725A, **1992**.

[29] J. C. Vartuli, K. D. Schmitt, C. T. Kresge, W. J. Roth, M. E. Leonowicz, S. B. McCullen, S. D. Hellring, J. S. Beck, J. L. Schlenker, *Chemistry of Materials* **1994**, *6*, 2317–2326.

[30] F. Di Renzo, H. Cambon, R. Dutartre, *Microporous Materials* **1997**, *10*, 283–286.

[31] T. R. Somo, M. J. Hato, K. D. Modibane in *Advanced Functional Porous Materials: From Macro to Nano Scale Lengths*, (Eds.: A. Uthaman, S. Thomas, T. Li, H. Maria), Engineering Materials, Springer International Publishing, Cham, **2022**, pp. 87–111.

[32] J. S. Beck et al., *Journal of the American Chemical Society* **1992**, *114*, 10834–10843.

[33] R. Fricke, H. Kosslick, G. Lischke, M. Richter, *Chemical Reviews* **2000**, *100*, 2303–2406.

[34] R. B. Borade, A. Clearfield, *Catalysis Letters* **1995**, *31*, 267–272.

[35] A. Corma, *Chemical Reviews* **1997**, *97*, 2373–2420.

[36] E. P. Barrett, L. G. Joyner, P. P. Halenda, *Journal of the American Chemical Society* **1951**, *73*, 373–380.

[37] S. Brunauer, P. H. Emmett, E. Teller, *Journal of the American Chemical Society* **1938**, *60*, 309–319.

[38] S. Storck, H. Bretinger, W. F. Maier, *Applied Catalysis A: General* **1998**, *174*, 137–146.

[39] A. Taguchi, F. Schüth, *Microporous and Mesoporous Materials* **2005**, *77*, 1–45.

[40] C. Perego, R. Millini, *Chemical Society Reviews* **2013**, *42*, 3956–3976.

[41] H. Kosslick, G. Lischke, G. Walther, W. Storek, A. Martin, R. Fricke, *Microporous Materials* **1997**, *9*, 13–33.

[42] K. Jaroszewska, B. Szczęśniak, B. Szyja, J. Choma, M. Jaroniec, *Materials Today* **2024**, *72*, 255–281.

[43] Z. Luan, C.-F. Cheng, H. He, J. Klinowski, *The Journal of Physical Chemistry* **1995**, *99*, 10590–10593.

[44] R. Schmidt, D. Akporiaye, M. Stöcker, O. H. Ellestad, *Journal of the Chemical Society Chemical Communications* **1994**, 1493–1494.

[45] C.-F. Cheng, J. Klinowski, *Journal of the Chemical Society Faraday Transactions* **1996**, *92*, 289–292.

[46] H. Kosslick, H. Landmesser, R. Fricke, *Journal of the Chemical Society Faraday Transactions* **1997**, *93*, 1849–1854.

[47] K. M. Reddy, I. Moudrakovski, A. Sayari, *Journal of the Chemical Society Chemical Communications* **1994**, 1059–1060.

[48] A. Corma, M. T. Navarro, J. Pérez Pariente, *Journal of the Chemical Society Chemical Communications* **1994**, *0*, 147–148.

[49] P. T. Tanev, M. Chibwe, T. J. Pinnavaia, *Nature* **1994**, *368*, 321–323.

[50] M. Ziolek, I. Nowak, J. Lavalley, *Catalysis Letters* **1997**, *45*, 259–265.

[51] D. Zhao, D. Goldfarb, *Journal of the Chemical Society Chemical Communications* **1995**, 875–876.

[52] N. Ulagappan, C. N. R. Rao, *Chemical Communications* **1996**, 1047–1048.

[53] J. Rathousky, A. Zukal, O. Franke, G. Schulz-Ekloff, *Journal of the Chemical Society Faraday Transactions* **1994**, *90*, 2821–2826.

[54] M. Adjdir, T. Ali-Dahmane, P. G. Weidler, *Comptes Rendus Chimie* **2009**, *12*, 793–800.

[55] H. Kosslick, G. Lischke, B. Parlitz, W. Storek, R. Fricke, *Applied Catalysis A: General* **1999**, *184*, 49–60.

[56] P. Strodel, K. M. Neyman, H. Knözinger, N. Rösch, *Chemical Physics Letters* **1995**, *240*, 547–552.

[57] R. D. Shannon, *Acta Crystallographica Section A* **1976**, *32*, 751–767.

[58] W. Loewenstein, *American Mineralogist* **1954**, *39*, 92–96.

[59] N. Szczepanik, A. Kowalczyk, Z. Piwowarska, L. Chmielarz, *Catalysts* **2022**, *12*, 1324.

[60] X. Chen, L. Huang, G. Ding, Q. Li, *Catalysis Letters* **1997**, *44*, 123–128.

[61] D. Zhao, Y. Wan, W. Zhou, *Ordered Mesoporous Materials*, 1st ed., Wiley, **2013**.

[62] J. N. Brönsted, *Recueil des Travaux Chimiques des Pays-Bas* **1923**, *42*, 718–728.

[63] C. Walling, *Journal of the American Chemical Society* **1950**, *72*, 1164–1168.

[64] W. B. Jensen, *Chemical Reviews* **1978**, *78*, 1–22.

[65] J. Sauer, *Journal of Molecular Catalysis* **1989**, *54*, 312–323.

[66] C. Bornes, D. Stosic, C. F. G. C. Geraldes, S. Mintova, J. Rocha, L. Mafra, *Chemistry – A European Journal* **2022**, *28*, e202201795.

[67] D. Coster, A. L. Blumenfeld, J. J. Fripiat, *The Journal of Physical Chemistry* **1994**, *98*, 6201–6211.

[68] H. M. Kao, C. P. Grey, *Journal of Physical Chemistry* **1996**, *100*, 5105–5117.

[69] V. L. Zholobenko, D. Plant, A. J. Evans, S. M. Holmes, *Microporous and Mesoporous Materials* **2001**, *44–45*, 793–799.

[70] W. Salvia, Y. Zhao, P. Chatterjee, W. Huang, F. A. Perras, *Chemical Communications* **2023**, *59*, 13962–13965.

[71] Z. Wang, T. Li, Y. Jiang, O. Lafon, Z. Liu, J. Trébosc, A. Baiker, J.-P. Amoureux, J. Huang, *Nature Communications* **2020**, *11*, 225.

[72] Z. Wang et al., *The Journal of Physical Chemistry Letters* **2021**, *12*, 11563–11572.

[73] Q. Luo, F. Deng, Z. Yuan, J. Yang, M. Zhang, Y. Yue, C. Ye, *The Journal of Physical Chemistry B* **2003**, *107*, 2435–2442.

[74] U. Eichler, M. Brändle, J. Sauer, *The Journal of Physical Chemistry B* **1997**, *101*, 10035–10050.

[75] A. J. Jones, E. Iglesia, *ACS Catalysis* **2015**, *5*, 5741–5755.

[76] W. Yang, Z. Wang, J. Huang, Y. Jiang, *The Journal of Physical Chemistry C* **2021**, *125*, 10179–10197.

[77] F. Leydier, C. Chizallet, A. Chaumonnot, M. Digne, E. Soyer, A.-A. Quoineaud, D. Costa, P. Raybaud, *Journal of Catalysis*, Molecular Approach to Heterogeneous Catalysis. **2011**, *284*, 215–229.

[78] C. Chizallet, P. Raybaud, *Angewandte Chemie International Edition* **2009**, *48*, 2891–2893.

[79] F. A. Perras, Z. Wang, T. Kobayashi, A. Baiker, J. Huang, M. Pruski, *Physical Chemistry Chemical Physics* **2019**, *21*, 19529–19537.

[80] A. Zheng, B. Han, B. Li, S.-B. Liu, F. Deng, *Chemical Communications* **2012**, *48*, 6936–6938.

[81] G. Busca, *Catalysis Today* **2020**, *357*, 621–629.

[82] R. J. Gillespie, T. E. Peel, E. A. Robinson, *Journal of the American Chemical Society* **1971**, *93*, 5083–5087.

[83] R. J. Gillespie, T. E. Peel, *Journal of the American Chemical Society* **1973**, *95*, 5173–5178.

[84] G. A. Olah, G. K. S. Prakash, J. Sommer, A. Molnar, *Superacid Chemistry*, Wiley & Sons, Incorporated, John, **2009**, 872 pp.

[85] A. Zheng, S.-J. Huang, W.-H. Chen, P.-H. Wu, H. Zhang, H.-K. Lee, L.-C. de Ménorval, F. Deng, S.-B. Liu, *The Journal of Physical Chemistry A* **2008**, *112*, 7349–7356.

[86] A. Zheng, H. Zhang, X. Lu, S.-B. Liu, F. Deng, *The Journal of Physical Chemistry B* **2008**, *112*, 4496–4505.

[87] S. Xin et al., *Chemical Science* **2019**, *10*, 10159–10169.

[88] H. Mix, J. Sauer, K.-P. Schröder, A. Merkel, *Collection of Czechoslovak Chemical Communications* **1988**, *53*, 2191–2202.

[89] W. Xu, T. Ollevier, F. Kleitz, *ACS Catalysis* **2018**, *8*, 1932–1944.

[90] E. Garrone, F. Fajula in *Acidity and Basicity*, Molecular Sieves, Springer, Berlin, Heidelberg, **2008**, pp. 213–267.

[91] G. Busca, *Catalysis Today* **1998**, *41*, 191–206.

[92] A. Palčić, V. Valtchev, *Applied Catalysis A: General* **2020**, *606*, 117795.

[93] L.-E. Sandoval-Díaz, J.-A. González-Amaya, C.-A. Trujillo, *Microporous and Mesoporous Materials* **2015**, *215*, 229–243.

[94] S. Viale, E. Garrone, F. Di Renzo, B. Chiche, F. Fajula in *Studies in Surface Science and Catalysis*, (Eds.: H. Chon, S.-K. Ihm, Y. S. Uh), Progress in Zeolite and Microporous Materials, Elsevier, **1997**, pp. 533–542.

[95] F. Leydier, C. Chizallet, D. Costa, P. Raybaud, *Chemical Communications* **2012**, *48*, 4076–4078.

[96] E. P. Parry, *Journal of Catalysis* **1963**, *2*, 371–379.

[97] G. Busca, *Physical Chemistry Chemical Physics* **1999**, *1*, 723–736.

[98] L. Damjanović, A. Auroux in *Zeolite Chemistry and Catalysis*, (Eds.: A. W. Chester, E. Derouane), Springer Netherlands, Dordrecht, **2009**, pp. 107–167.

[99] W. L. Earl, P. O. Fritz, A. A. V. Gibson, J. H. Lunsford, *The Journal of Physical Chemistry* **1987**, *91*, 2091–2095.

[100] D. Zhao, C. Nie, Y. Zhou, S. Xia, L. Huang, Q. Li, *Catalysis Today*, Nanomaterials in Catalysis **2001**, *68*, 11–20.

[101] W.-H. Chen, Q. Zhao, H.-P. Lin, Y.-S. Yang, C.-Y. Mou, S.-B. Liu, *Microporous and Mesoporous Materials* **2003**, *66*, 209–218.

[102] K. Suzuki, Y. Aoyagi, N. Katada, M. Choi, R. Ryoo, M. Niwa, *Catalysis Today*, 11th Korea-Japan Symposium on Catalysis, 21-23 May 2007, Seoul, Korea **2008**, *132*, 38–45.

[103] L. H. Molina-Conde, A. Suárez-Méndez, D. E. Pérez-Estrada, T. E. Klimova, *Applied Catalysis A: General* **2023**, *663*, 119313.

[104] A. N. Mlinar, S. Shylesh, O. C. Ho, A. T. Bell, *ACS Catalysis* **2014**, *4*, 337–343.

[105] S. Moussa, P. Concepción, M. A. Arribas, A. Martínez, *Applied Catalysis A: General* **2020**, *608*, 1–53.

[106] N. Lang, A. Tuel, *Chemistry of Materials* **2004**, *16*, 1961–1966.

[107] W. J. Mortier, *Journal of Catalysis* **1978**, *55*, 138–145.

[108] E. J. Hensen, D. G. Poduval, V. Degirmenci, D. J. M. Ligthart, W. Chen, F. Maugé, M. S. Rigutto, J. R. van Veen, *The Journal of Physical Chemistry C* **2012**, *116*, 21416–21429.

[109] M. Hunger, D. Freude, H. Pfeifer, *Journal of the Chemical Society Faraday Transactions* **1991**, *87*, 657–662.

[110] C.-F. Cheng, H. He, W. Zhou, J. Klinowski, J. A. S. Gonçalves, L. F. Gladden, *The Journal of Physical Chemistry* **1996**, *100*, 390–396.

[111] M. Chatterjee, T. Iwasaki, Y. Onodera, T. Nagase, H. Hayashi, T. Ebina, *Chemistry of Materials* **2000**, *12*, 1654–1659.

[112] A. S. Al-Fatesh, A. A. Ibrahim, J. K. Abu-Dahrieh, A. S. Al-Awadi, A. M. El-Toni, A. H. Fakeeha, A. E. Abasaeed, *Catalysts* **2018**, *8*, 229.

[113] G. Turnes Palomino, J. José Cuart Pascual, M. Rodríguez Delgado, J. Bernardo Parra, C. Otero Areán, *Materials Chemistry and Physics* **2004**, *85*, 145–150.

[114] C. Otero Areán, M. Rodríguez Delgado, V. Montouillout, J. C. Lavalley, C. Fernandez, J. J. Cuart Pascual, J. B. Parra, *Microporous and Mesoporous Materials* **2004**, *67*, 259–264.

[115] H. K. C. Timken, E. Oldfield, *Journal of the American Chemical Society* **1987**, *109*, 7669–7673.

[116] W. Zhang, C. I. Ratcliffe, I. L. Moudrakovski, J. S. Tse, C.-Y. Mou, J. A. Ripmeester, *Microporous and Mesoporous Materials* **2005**, *79*, 195–203.

[117] H. Olivier-Bourbigou, P. A. R. Breuil, L. Magna, T. Michel, M. F. Espada Pastor, D. Delcroix, *Chemical Reviews* **2020**, *120*, 7919–7983.

[118] Y. Chauvin, *Angewandte Chemie International Edition* **2006**, *45*, 3740–3747.

[119] C. Chizallet, C. Bouchy, K. Larmier, G. Pirngruber, *Chemical Reviews* **2023**, *123*, 6107–6196.

[120] K. Ziegler, E. Holzkamp, H. Breil, H. Martin, *Angewandte Chemie* **1955**, *67*, 541–547.

[121] G. C. Bailey, J. A. Reid (Phillips Petroleum Co), *US Pat.*, 2381198A, **1945**.

[122] F. D. Nierlich, J. D. Neumeister, T. D. Wildt, W. D. Droste, F. D. Obenaus (Huels AG, Chemische Werke Huels AG), *European pat.*, 0395857B1, **1994**.

[123] F. D. Nierlich, J. D. Neumeister, T. D. Wildt, W. D. Droste, F. D. Obenaus (Huels AG, Chemische Werke Huels AG), *German pat.*, 3914817C2, **1995**.

[124] J. R. Sohn, A. Ozaki, *Journal of Catalysis* **1980**, *61*, 29–38.

[125] M. L. Sarazen, E. Doskocil, E. Iglesia, *Journal of Catalysis* **2016**, *344*, 553–569.

[126] W. Markownikoff, *Justus Liebigs Annalen der Chemie* **1870**, *153*, 228–259.

[127] S. Albrecht, D. Kießling, G. Wendt, D. Maschmeyer, F. Nierlich, *Chemie Ingenieur Technik* **2005**, *77*, 695–709.

[128] P. Cossee, *Journal of Catalysis* **1964**, *3*, 80–88.

[129] E. J. Arlman, *Journal of Catalysis* **1964**, *3*, 89–98.

[130] E. J. Arlman, P. Cossee, *Journal of Catalysis* **1964**, *3*, 99–104.

[131] S. H. Chikkali, *Resonance* **2017**, *22*, 1039–1060.

[132] S. Forget, H. Olivier-Bourbigou, D. Delcroix, *ChemCatChem* **2017**, *9*, 2408–2417.

[133] L. M. Kustov, V. Yu. Borovkov, V. B. Kazansky in *Studies in Surface Science and Catalysis*, (Eds.: P. A. Jacobs, N. I. Jaeger, P. Jírů, V. B. Kazansky, G. Schulz-Ekloff), Structure and Reactivity of Modified Zeolites, Elsevier, **1984**, pp. 241–247.

[134] R. Y. Brogaard, U. Olsbye, *ACS Catalysis* **2016**, *6*, 1205–1214.

[135] A. Abragam, *The Principles of Nuclear Magnetism*, Oxford University Press, Oxford, **1961**, 599 pp.

[136] C. P. Poole, H. A. Farach, *Theory of Magnetic Resonance*, Second edition, John Wiley & Sons, New York, NY, **1987**, 359 pp.

[137] M. H. Levitt, *Spin Dynamics: Basics of Nuclear Magnetic Resonance*, Second edition, John Wiley & Sons, Ltd, Chichester, UK, **2008**, 16145 pp.

[138] J. J. Keeler, *Understanding NMR Spectroscopy*, 2. ed., repr, Wiley, Chichester, **2011**.

[139] D. C. Apperley, R. K. Harris, P. Hodgkinson, *Solid-State NMR: Basic Principles & Practice*, Momentum Press, LLC, New York, **2012**, 1 p.

[140] *Solid-State NMR Spectroscopy Principles and Applications*, 1st ed., (Ed.: M. J. Duer), Wiley, **2001**.

[141] M. Mehring, *Principles of High Resolution NMR in Solids*, Second, revised and enlarged edition, softcover reprint of the hardcover 2nd edition 1983, Springer, Berlin Heidelberg New York, **1983**, 342 pp.

[142] M. Bertmer, *Solid State Nuclear Magnetic Resonance* **2017**, *81*, 1–7.

[143] A. J. Pell, G. Pintacuda, C. P. Grey, *Progress in Nuclear Magnetic Resonance Spectroscopy* **2019**, *111*, 1–271.

[144] *Paramagnetism in Experimental Biomolecular NMR*, (Eds.: C. Luchinat, G. Parigi, E. Ravera), Royal Society of Chemistry, London, UK, **2018**, 316 pp.

[145] F. H. Köhler in *Encyclopedia of Magnetic Resonance*, (Ed.: R. K. Harris), John Wiley & Sons, Ltd, Chichester, UK, **2011**, emrstm1229.

[146] E. L. Hahn, *Physical Review* **1950**, *80*, 580–594.

[147] S. R. Hartmann, *Physical Review* **1962**, *128*, 2042–2053.

[148] A. Pines, M. G. Gibby, J. S. Waugh, *The Journal of Chemical Physics* **1972**, *56*, 1776–1777.

[149] E. R. Andrew, A. Bradbury, R. G. Eades, *Nature* **1958**, *182*, 1659–1659.

[150] T. Le Marchand, T. Schubeis, M. Bonaccorsi, P. Paluch, D. Lalli, A. J. Pell, L. B. Andreas, K. Jaudzems, J. Stanek, G. Pintacuda, *Chemical Reviews* **2022**, *122*, 9943–10018.

[151] T. Polenova, R. Gupta, A. Goldbourt, *Analytical Chemistry* **2015**, *87*, 5458–5469.

[152] A. Samoson, *Journal of Magnetic Resonance* **2019**, *306*, 167–172.

[153] Y. Nishiyama, G. Hou, V. Agarwal, Y. Su, A. Ramamoorthy, *Chemical Reviews* **2023**, *123*, 918–988.

[154] J. W. Hennel, J. Klinowski in *New Techniques in Solid-State NMR*, (Ed.: J. Klinowski), Springer, Berlin, Heidelberg, **2005**, pp. 1–14.

[155] G. J. Kennedy, M. Afeworki, D. C. Calabro, C. E. Chase, R. J. Smiley, *Applied Spectroscopy* **2004**, *58*, 698–704.

[156] H. Ernst, D. Freude, I. Wolf, *Chemical Physics Letters* **1993**, *212*, 588–596.

[157] Z. Wang, Y. Jiang, C. Stampfl, A. Baiker, M. Hunger, J. Huang, *ChemCatChem* **2020**, *12*, 287–293.

[158] M. Müller, G. Harvey, R. Prins, *Microporous and Mesoporous Materials* **2000**, *34*, 281–290.

[159] M. Hunger, D. Freude, H. Pfeifer, *Catalysis Today* **1988**, *3*, 507–512.

[160] E. Brunner, H. Pfeifer in *Acidity and Basicity*, Molecular Sieves, Springer, Berlin, Heidelberg, **2008**, pp. 1–43.

[161] Y. Jiang, J. Huang, W. Dai, M. Hunger, *Solid State Nuclear Magnetic Resonance* **2011**, *39*, 116–141.

[162] K. J. D. MacKenzie, *Multinuclear Solid-State NMR of Inorganic Materials*, *Vol. 6*, Pergamon, Amsterdam, **2002**, 748 pp.

[163] K. Chen, Z. Gan, S. Horstmeier, J. L. White, *Journal of the American Chemical Society* **2021**, *143*, 6669–6680.

[164] J. Jiao, J. Kanellopoulos, W. Wang, S. S. Ray, H. Foerster, D. Freude, M. Hunger, *Physical Chemistry Chemical Physics* **2005**, *7*, 3221–3226.

[165] C. Martineau-Corcos, J. Dědeček, F. Taulelle, *Solid State Nuclear Magnetic Resonance*, Solid-State NMR Spectroscopy of Quadrupolar Nuclei **2017**, *84*, 65–72.

[166] W. O. Parker, S. Wegner, *Microporous and Mesoporous Materials* **2012**, *158*, 235–240.

[167] G. Czjzek, J. Fink, F. Götz, H. Schmidt, J. M. D. Coey, J.-P. Rebouillat, A. Liénard, *Physical Review B* **1981**, *23*, 2513–2530.

[168] D. R. Neuville, L. Cormier, D. Massiot, *Geochimica et Cosmochimica Acta*, Structure and Properties of Siliate Melts and Fluids **2004**, *68*, 5071–5079.

[169] U. Werner-Zwanziger, A. L. Paterson, J. W. Zwanziger, *Journal of Non-Crystalline Solids* **2020**, *550*, 120383.

[170] E. Lam, A. Comas-Vives, C. Copéret, *Journal of Physical Chemistry C* **2017**, *121*, 19946–19957.

[171] J. T. Ash, P. J. Grandinetti, *Magnetic Resonance in Chemistry* **2006**, *44*, 823–831.

[172] P. Castro-Fernández et al., *Chemical Science* **2021**, *12*, 15273–15283.

[173] J. Klinowski in *Solid-State NMR Spectroscopy Principles and Applications*, (Ed.: M. J. Duer), Wiley, **2001**, pp. 437–482.

[174] H. Jancke, J. Schulz, E. Popowski, H. Kelling, *Journal of Organometallic Chemistry* **1988**, *354*, 23–29.

[175] C. B. Hurd, *Journal of the American Chemical Society* **1946**, *68*, 364–370.

[176] A. T. Bell, *Colloids and Surfaces A: Physicochemical and Engineering Aspects* **1999**, *158*, 221–234.

[177] G. Engelhardt, U. Lohse, E. Lippmaa, M. Tarmak, M. Mägi, *Zeitschrift für anorganische und allgemeine Chemie* **1981**, *482*, 49–64.

[178] K. Hara, S. Akahane, J. W. Wiench, B. R. Burgin, N. Ishito, V. S.-Y. Lin, A. Fukuoka, M. Pruski, *The Journal of Physical Chemistry C* **2012**, *116*, 7083–7090.

[179] C. A. Fyfe, H. Grondey, Y. Feng, H. Gies, G. T. Kokotailo in *Zeolite Microporous Solids: Synthesis, Structure, and Reactivity*, (Eds.: E. G. Derouane, F. Lemos, C. Naccache, F. R. Ribeiro), Springer Netherlands, Dordrecht, **1992**, pp. 225–245.

[180] V. I. Bakhmutov, B. G. Shpeizer, A. V. Prosvirin, K. R. Dunbar, A. Clearfield, *Microporous and Mesoporous Materials* **2009**, *118*, 78–86.

[181] F. Pourpoint, F. Venel, R. Giovine, J. Trébosc, T. Vancompernolle, M. Taoufik, V. Sarou-Kanian, R. M. Gauvin, O. Lafon, *Journal of Magnetic Resonance* **2021**, *330*, 107029.

[182] P. Tekely in *Modern Magnetic Resonance*, (Ed.: G. A. Webb), Springer Netherlands, Dordrecht, **2006**, pp. 197–203.

[183] M. Dyballa, *Energy & Fuels* **2023**, *37*, 18517–18559.

[184] A. Zheng, S.-B. Liu, F. Deng, *Solid State Nuclear Magnetic Resonance* **2013**, *55–56*, 12–27.

[185] C. Freitas, N. S. Barrow, V. Zholobenko, *Johnson Matthey Technology Review* **2018**, *62*, 279–290.

[186] I. G. Shenderovich, G. Buntkowsky, A. Schreiber, E. Gedat, S. Sharif, J. Albrecht, N. S. Golubev, G. H. Findenegg, H. H. Limbach, *Journal of Physical Chemistry B* **2003**, *107*, 11924–11939.

[187] A. I. Biaglow, R. J. Gorte, G. T. Kokotailo, D. White, *Journal of Catalysis* **1994**, *148*, 779–786.

[188] J. Jänchen, J. H. M. C. van Wolput, L. J. M. van de Ven, J. W. de Haan, R. A. van Santen, *Catalysis Letters* **1996**, *39*, 147–152.

[189] J. Huang, Y. Jiang, V. R. Reddy Marthala, W. Wang, B. Sulikowski, M. Hunger, *Microporous and Mesoporous Materials*, Inside Pores Workshop IN SItu Study and DEvelopment of Processes Involving NanoPORous Solids **2007**, *99*, 86–90.

[190] K. Gong, Z. Liu, L. Liang, Z. Zhao, M. Guo, X. Liu, X. Han, X. Bao, G. Hou, *The Journal of Physical Chemistry Letters* **2021**, *12*, 2413–2422.

[191] D. S. Zasukhin, I. A. Kostyukov, I. A. Kasyanov, Y. G. Kolyagin, I. I. Ivanova, *Petroleum Chemistry* **2021**, *61*, 875–894.

[192] C. Rieg et al., *The Journal of Physical Chemistry C* **2022**, acs.jpcc.2c04114.

[193] H. M. Kao, P. C. Chang, Y. W. Liao, L. P. Lee, C. H. Chien, *Microporous and Mesoporous Materials* **2008**, *114*, 352–364.

[194] A. Zheng, S. B. Liu, F. Deng, *Chemical Reviews* **2017**, *117*, 12475–12531.

[195] Laima. Baltusis, J. S. Frye, G. E. Maciel, *Journal of the American Chemical Society* **1986**, *108*, 7119–7120.

[196] C. Bornes, M. Sardo, Z. Lin, J. Amelse, A. Fernandes, M. F. Ribeiro, C. Geraldes, J. Rocha, L. Mafra, *Chemical Communications* **2019**, *55*, 12635–12638.

[197] J. Yin et al., *Nature Communications* **2022**, *13*, 5112.

[198] L. Lakiss, A. Vicente, J.-P. Gilson, V. Valtchev, S. Mintova, A. Vimont, R. Bedard, S. Abdo, J. Bricker, *ChemPhysChem* **2020**, *21*, 1873–1881.

[199] E. F. Rakiewicz, A. W. Peters, R. F. Wormsbecher, K. J. Sutovich, K. T. Mueller, *The Journal of Physical Chemistry B* **1998**, *102*, 2890–2896.

[200] K. J. Sutovich, A. W. Peters, E. F. Rakiewicz, R. F. Wormsbecher, S. M. Mattingly, K. T. Mueller, *Journal of Catalysis* **1999**, *183*, 155–158.

[201] L. Baltusis, J. S. Frye, G. E. Maciel, *Journal of the American Chemical Society* **1987**, *109*, 40–46.

[202] A. Corma, M. S. Grande, V. Gonzalez-Alfaro, A. V. Orchilles, *Journal of Catalysis* **1996**, *159*, 375–382.

[203] A. Zheng, S. Li, F. Deng in *Modern Magnetic Resonance*, (Ed.: G. A. Webb), Springer International Publishing, Cham, **2018**, pp. 1049–1071.

[204] MFI: Framework Type, https://europe.iza-structure.org/IZA-SC/framework.php?ID=149 (visited on 10/28/2024).

[205] C. Bornes, M. Fischer, J. A. Amelse, C. F. G. C. Geraldes, J. Rocha, L. Mafra, *Journal of the American Chemical Society* **2021**, *143*, 13616–13623.

[206] R. Zhao, Z. Zhao, S. Li, W. Zhang, *The Journal of Physical Chemistry Letters* **2017**, *8*, 2323–2327.

[207] Q. Zhao, W. H. Chen, S. J. Huang, Y. C. Wu, H. K. Lee, S. B. Liu, *Journal of Physical Chemistry B* **2002**, *106*, 4462–4469.

[208] S. Hayashi, *Chemistry Letters* **2009**, *38*, 960–961.

[209] N. Kojima, S. Hayashi, *Bulletin of the Chemical Society of Japan* **2011**, *84*, 1090–1095.

[210] S. Hayashi, K. Jimura, N. Kojima, *Microporous and Mesoporous Materials* **2014**, *186*, 101–105.

[211] S. Hayashi, N. Kojima, *Microporous and Mesoporous Materials* **2011**, *141*, 49–55.

[212] S. Hayashi, K. Jimura, N. Kojima, *Bulletin of the Chemical Society of Japan* **2014**, *87*, 69–75.

[213] C. Bornes, C. F. G. C. Geraldes, J. Rocha, L. Mafra, *Microporous and Mesoporous Materials* **2023**, *360*, 112666.

[214] P. V. Wiper, J. Amelse, L. Mafra, *Journal of Catalysis* **2014**, *316*, 240–250.

[215] Y. Wang, S. Xin, Y. Chu, J. Xu, G. Qi, Q. Wang, Q. Xia, F. Deng, *Journal of Physical Chemistry C* **2021**, *125*, 9497–9506.

[216] X. Yi, H. H. Ko, F. Deng, S. B. Liu, A. Zheng, *Nature Protocols* **2020**, *15*, 3527–3555.

[217] M. C. R. Symons, G. Eaton, *Journal of the Chemical Society Faraday Transactions 1: Physical Chemistry in Condensed Phases* **1982**, *78*, 3033–3044.

[218] M. D. Karra, K. J. Sutovich, K. T. Mueller, *Journal of the American Chemical Society* **2002**, *124*, 902–903.

[219] N. Feng, A. Zheng, S.-J. Huang, H. Zhang, N. Yu, C.-Y. Yang, S.-B. Liu, F. Deng, *The Journal of Physical Chemistry C* **2010**, *114*, 15464–15472.

[220] D. S. Zasukhin, I. A. Kasyanov, Y. G. Kolyagin, A. I. Bulygina, K. C. Kharas, I. I. Ivanova, *ACS Omega* **2022**, *7*, 12318–12328.

[221] Q. Zhao, W.-H. Chen, S.-J. Huang, S.-B. Liu in *Studies in Surface Science and Catalysis*, (Eds.: M. Anpo, M. Onaka, H. Yamashita), Science and Technology in Catalysis 2002, Elsevier, **2003**, pp. 205–209.

[222] Y. Seo, K. Cho, Y. Jung, R. Ryoo, *ACS Catalysis* **2013**, *3*, 713–720.

[223] H. M. McConnell, C. H. Holm, *The Journal of Chemical Physics* **1957**, *27*, 314–315.

[224] K. W. Barnett, *Journal of Organometallic Chemistry* **1974**, *78*, 139–165.

[225] S. E. J. Anderson, R. S. Drago, *Inorganic Chemistry* **1972**, *11*, 1564–1572.

[226] M. F. Rettig, R. S. Drago, *Journal of the American Chemical Society* **1969**, *91*, 1361–1370.

[227] H. P. Fritz, H. J. Keller, K. E. Schwarzhans, *Journal of Organometallic Chemistry* **1967**, *7*, 105–111.

[228] H. Heise, F. H. Köhler, X. Xie, *Journal of Magnetic Resonance* **2001**, *150*, 198–206.

[229] F. Aquino, B. Pritchard, J. Autschbach, *Journal of Chemical Theory and Computation* **2012**, *8*, 598–609.

[230] J. W. Benzie, G. E. Harmon-Welch, J. C. Hoefler, V. I. Bakhmutov, J. Blümel, *Langmuir* **2022**, *38*, 7422–7432.

[231] L. Qu, W. Zhang, P. J. Kooyman, R. Prins, *Journal of Catalysis* **2003**, *215*, 7–13.

[232] FAU: Framework Type, https://europe.iza-structure.org/IZA-SC/framework.php?ID=93 (visited on 11/21/2024).

[233] A. Julbe, M. Drobek in *Encyclopedia of Membranes*, (Eds.: E. Drioli, L. Giorno), Springer, Berlin, Heidelberg, **2016**, pp. 767–768.

[234] I. Díaz, E. Kokkoli, O. Terasaki, M. Tsapatsis, *Chemistry of Materials* **2004**, *16*, 5226–5232.

[235] E. M. Flanigen, J. M. Bennett, R. W. Grose, J. P. Cohen, R. L. Patton, R. M. Kirchner, J. V. Smith, *Nature* **1978**, *271*, 512–516.

[236] J. F. Haw, B. R. Richardson, I. S. Oshiro, N. D. Lazo, J. A. Speed, *Journal of the American Chemical Society* **1989**, *111*, 2052–2058.

[237] S. Hayashi, *Analytical Sciences* **2009**, *25*, 133–136.

[238] A. F. Holleman, E. Und Nils Wiberg, G. Fischer, *Lehrbuch Der Anorganischen Chemie*, Walter de Gruyter, Berlin • New York, **2007**.

[239] M. Schröder, *NMRAspecds*, version v0.1.0, Zenodo, **2024**.

[240] T. Biskup, *ASpecD*, version v0.10.1, Zenodo, **2024**.

[241] J. Popp, T. Biskup, *Chemistry–Methods* **2022**, *2*, e202100097.

[242] D. Massiot, F. Fayon, M. Capron, I. King, S. Le Calvé, B. Alonso, J.-O. Durand, B. Bujoli, Z. Gan, G. Hoatson, *Magnetic Resonance in Chemistry* **2002**, *40*, 70–76.

[243] S. G. J. van Meerten, W. M. J. Franssen, A. P. M. Kentgens, *Journal of Magnetic Resonance* **2019**, *301*, 56–66.

[244] B. Mezari, P. C. M. M. Magusin, S. M. T. Almutairi, E. A. Pidko, E. J. M. Hensen, *The Journal of Physical Chemistry C* **2021**, *125*, 9050–9059.

[245] L. Lakiss, C. Kouvatas, J.-P. Gilson, H. A. Aleksandrov, G. N. Vayssilov, N. Nesterenko, S. Mintova, V. Valtchev, *Angewandte Chemie* **2021**, *133*, 26906–26913.

[246] Z. Yan, D. Ma, J. Zhuang, X. Liu, X. Liu, X. Han, X. Bao, F. Chang, L. Xu, Z. Liu, *Journal of Molecular Catalysis A: Chemical* **2003**, *194*, 153–167.

[247] M. T. Janicke, C. C. Landry, S. C. Christiansen, S. Birtalan, G. D. Stucky, B. F. Chmelka, *Chemistry of Materials* **1999**, *11*, 1342–1351.

[248] H. E. Gottlieb, V. Kotlyar, A. Nudelman, *The Journal of Organic Chemistry* **1997**, *62*, 7512–7515.

[249] B. Martin, J. Autschbach, *The Journal of Chemical Physics* **2015**, *142*, 054108.

[250] L. Serger, BA thesis, Universität Rostock, Rostock, **2024**.

[251] F. A. Perras, Personal Communication, **2023**.

[252] S. A. Rouf, V. B. Jakobsen, J. Mareš, N. D. Jensen, C. J. McKenzie, J. Vaara, U. G. Nielsen, *Solid State Nuclear Magnetic Resonance* **2017**, *87*, 29–37.

[253] S. K. K. Swamy, PhD thesis, Le Mans Université, **2013**.

[254] H. M. Kao, C. Y. Yu, M. C. Yeh, *Microporous and Mesoporous Materials* **2002**, *53*, 1–12.

[255] J. H. Lunsford, W. P. Rothwell, W. Shen, *Journal of the American Chemical Society* **1985**, *107*, 1540–1547.

[256] M. J. Nash, A. M. Shough, D. W. Fickel, D. J. Doren, R. F. Lobo, *Journal of the American Chemical Society* **2008**, *130*, 2460–2462.

[257] Zeev. Luz, A. J. Vega, *The Journal of Physical Chemistry* **1987**, *91*, 374–382.

[258] S. Hayashi, M. Yanagisawa, K. Hayamizu, *Analytical Sciences* **1991**, *7*, 955–957.

[259] W. Li, Q. Zhang, J. J. Joos, P. F. Smet, J. Schmedt Auf Der Günne, *Physical Chemistry Chemical Physics* **2019**, *21*, 10185–10194.

[260] J. Cunningham, F. A. Perras, *Journal of Magnetic Resonance Open* **2022**, *12–13*, 100066.

[261] A. Lesage et al., *Journal of the American Chemical Society* **2010**, *132*, 15459–15461.

[262] T. Kobayashi, M. Pruski, *ChemPhysChem* **2021**, *22*, 1441–1445.

[263] I. B. Moroz, A. Lund, M. Kaushik, L. Severy, D. Gajan, A. Fedorov, A. Lesage, C. Copéret, *ACS Catalysis* **2019**, *9*, 7476–7485.

[264] Matt Newville et al., *Lmfit/Lmfit-Py: 1.3.2*, version 1.3.2, Zenodo, **2024**.

[265] R. K. Harris, E. D. Becker, S. M. C. de Menezes, P. Granger, R. E. Hoffman, K. W. Zilm, *Pure and Applied Chemistry* **2008**, *80*, 59–84.

[266] C. R. Morcombe, K. W. Zilm, *Journal of Magnetic Resonance* **2003**, *162*, 479–486.

[267] R. Benn, H. Grondey, C. Brevard, A. Pagelot, *Journal of the Chemical Society Chemical Communications* **1988**, 102–103.

[268] W. Kolodzicjski, J. Klinowski, *Solid State Nuclear Magnetic Resonance* **1992**, *1*, 41–44.

[269] C. I. Nieto et al., *Molecules* **2015**, *20*, 15643–15665.

[270] A. Takagaki, J. Chul Jung, S. Hayashi, *RSC Advances* **2014**, *4*, 43785–43791.

[271] R. K. Harris, E. D. Becker, S. M. Cabral de Menezes, R. Goodfellow, P. Granger, *Pure and Applied Chemistry* **2001**, *73*, 1795–1818.

[272] R. Hoffman, *Journal of Magnetic Resonance* **2022**, *340*, 107231.

[273] D. L. Bryce, G. M. Bernard, M. Gee, M. D. Lumsden, K. Eichele, R. E. Wasylishen, *Can. J. Anal. Sci. Spectrosc.* **2001**, *46*, 46–82.

Part IV

APPENDIX

A

MATERIALS AND SAMPLES

Table A.1: Details on the support materials used in this work. The batch numbers indicate the support materials as synthesized and stored on air, without re-calcination or stored within the glovebox.

Support Type	Batch	Molar ratio Si/T	T /w%	Si /w%
Al-M20	4	14.1	2.1	30.7
Al-M20 (07/22)	30	12.5	2.2	28.9
Al-M10	23	7.3	3.8	29.1
Al-M10 (06/22)	26	6.1	4.7	30.0
Al-M10 (07/22)	32	6.4	4.4	29.2
Ga-M20	3	23.2	3.5	33.0
Ga-M10	45	11.0	6.6	29.1
MCM-41	20	–	–	–
USY	76	2.6	11.6	31.5

Table A.2: Details on the samples of this work.

ID	Composition	Preparation	Comment
44	Al-M20		^{27}Al and ^{29}Si measurements
231	Ga-M10 pure		
232	Ga-M20 pure		
233	Al-M10 pure		
234	Al-M20 pure		
113	Ga-M10 (extra dry)	dehydrated, method 1.1	
119	Ga-M10 (extra dry 2)	dehydrated, method 1.2	
191	Ga-M20 (Aveiro)	dehydrated, method 2	

ID	Composition	Preparation	Comment
193	Al-M10 (Aveiro)	dehydrated, method 2	
34	Al-M20 + Ni		
35	Ga-M20 + Ni		
47	Al-M10 + Ni		
230	Ga-M10 + Ni		
48	MCM-41 + Ni		
176	Al_2O_3 + Ni		
177	Sasol S9 + Ni		
195	Sasol S12 + Ni		
201	Sasol S13 + Ni		
60	D-Al-M10 + Ni		
85	D-Al-M20 + Ni		
86	D-Ga-M20 + Ni		
52	Al-M20 + TMPO	SB	P/Al = 1.5
51	Al-M20 + TMPO	SB	P/Al = 1.0
50	Al-M20 + TMPO	SB	P/Al = 0.6
49	Al-M20 + TMPO	SB	P/Al = 0.2
78	Al-M10 + TMPO	SB	P/Al = 0.6
79	Ga-M10 + TMPO	SB	P/Ga = 1.5
80	Al-M20 + TMPO	SB	P/Al = 0.6
81	Ga-M20 + TMPO	SB	P/Ga = 1.5
105	Al-M10 + TMPO (hydrated)	96 % humidity	from sa78
106	Ga-M10 + TMPO (hydrated)	96 % humidity	from sa79
107	Al-M20 + TMPO (hydrated)	96 % humidity	from sa80
108	Ga-M20 + TMPO (hydrated)	96 % humidity	from sa81
98	Al-M20 + TMPO	SB	P/Al = 1.5
97	Al-M20 + TMPO	SB	P/Al = 0.6
96	Ga-M10 + TMPO	SB	P/Ga = 1.5
95	Al-M10 + TMPO	SB	P/Al = 0.6
94	Ga-M20 + TMPO	SB	P/Ga = 1.5
61	S1 + TMPO	SB	0.5 mmol g^{-1}

ID	Composition	Preparation	Comment
203	Ga-M10 + TMPO	SB	P/Ga = 0.5
220	Ga-M10 + TMPO	SB	P/Ga = 0.6
221	Ga-M20 + TMPO	SB	P/Ga = 0.6
222	USY + TMPO	SB	P/Al = 0.6
223	Ga-M10 + TMPO	SF (**method 3**)	P/Ga = 0.2
224	Ga-M10 + TMPO	SF (**method 3**)	P/Ga = 0.6
225	USY + TMPO	SF (**method 3**)	P/Al = 0.6
226	Ga-M10 + TMPO (hydrated)	75 % humidity	from sa220
227	Ga-M20 + TMPO (hydrated)	75 % humidity	from sa221
228	USY + TMPO (hydrated)	75 % humidity	from sa222
229	Ga-M10 + TMPO (hydrated)	75 % humidity	from sa224
189	Al-M20 + TMPO (Aveiro)	SF, heated (**method 2**)	P/Al = 0.6
190	Ga-M10 + TMPO (Aveiro)	SF, heated (**method 2**)	P/Ga = 1.5
192	Ga-M20 + TMPO (Aveiro)	SF, heated (**method 2**)	P/Ga = 1.5
194	Al-M10 + TMPO (Aveiro)	SF, heated (**method 2**)	P/Al = 0.6
211	Al-M20 + TMPO (hydrated)	75 % humidity	from sa189
212	Ga-M10 + TMPO (hydrated)	75 % humidity	from sa190
213	Ga-M20 + TMPO (hydrated)	75 % humidity	from sa192
214	Al-M10 + TMPO (hydrated)	75 % humidity	from sa194
110	Ga-M10 + Ni and TMPO	Ni + TMPO method 1	P/Ga = 1.5
111	Ga-M10 + Ni and TMPO	Ni + TMPO method 2	P/Ga = 1.5
112	Ga-M10 + Ni and TMPO	Ni + TMPO method 3	P/Ga = 1.5

ID	Composition	Preparation	Comment
122	Al-M20 + Ni (0.2%) and TMPO	Ni + TMPO method 3	P/Ga = 1.5
123	Al-M20 + Ni (0.6%) and TMPO	Ni + TMPO method 3	P/Ga = 1.5
124	Al-M20 + Ni (1.2%) and TMPO	Ni + TMPO method 3	P/Ga = 1.5

B

ADDITIONAL FIGURES AND TABLES

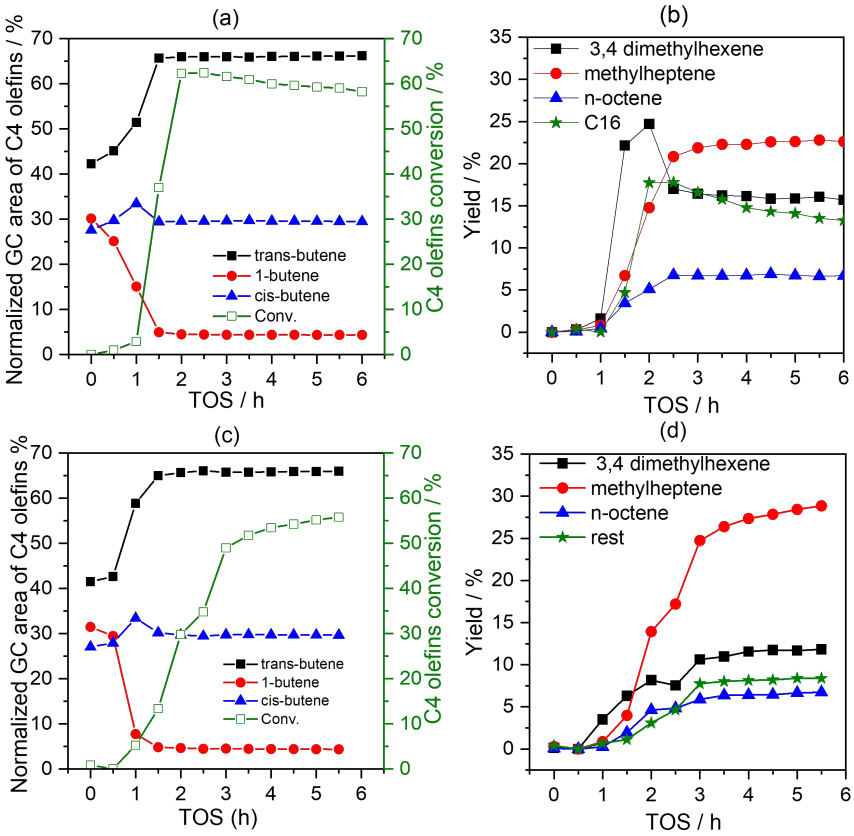

Figure B.1: On-line GC analysis of the reaction over (a) Ni/Al-M10 and (c) Ni/Ga-M10 catalysts at 80 °C under raffinate III (15 bar): fraction plotted as normalized GC areas; (b) and (d) the corresponding yield of products during time on stream.

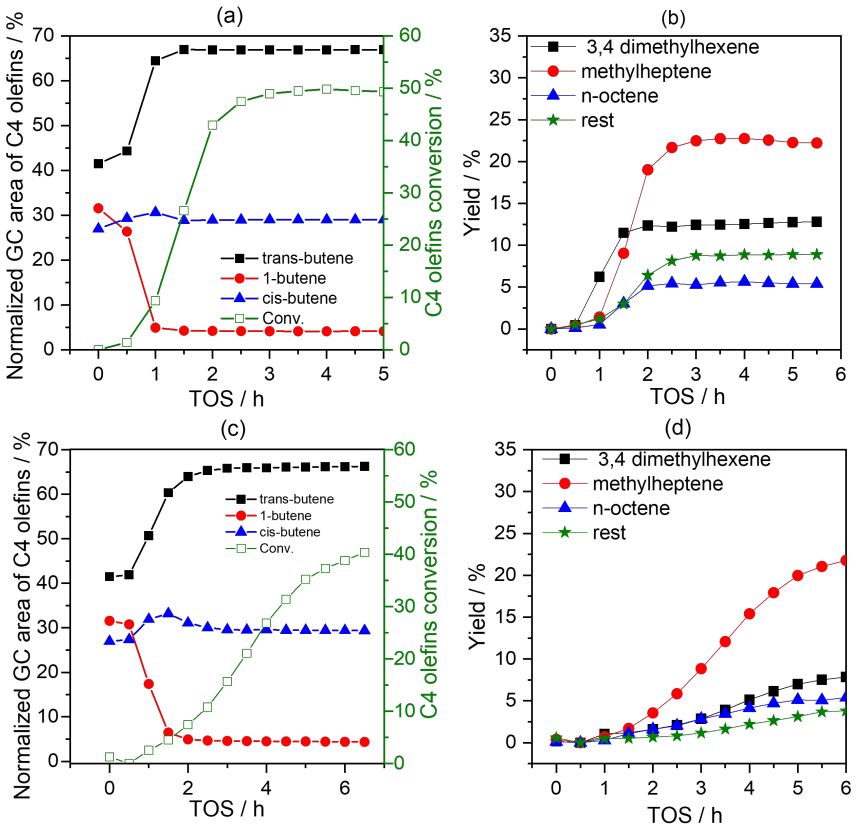

Figure B.2: On-line GC analysis of the reaction over (a) Ni/Al-M20 and (c) Ni/Ga-M20 catalysts at 80 °C under raffinate III (15 bar): fraction plotted as normalized GC areas; (b) and (d) the corresponding yield of products during time on stream.

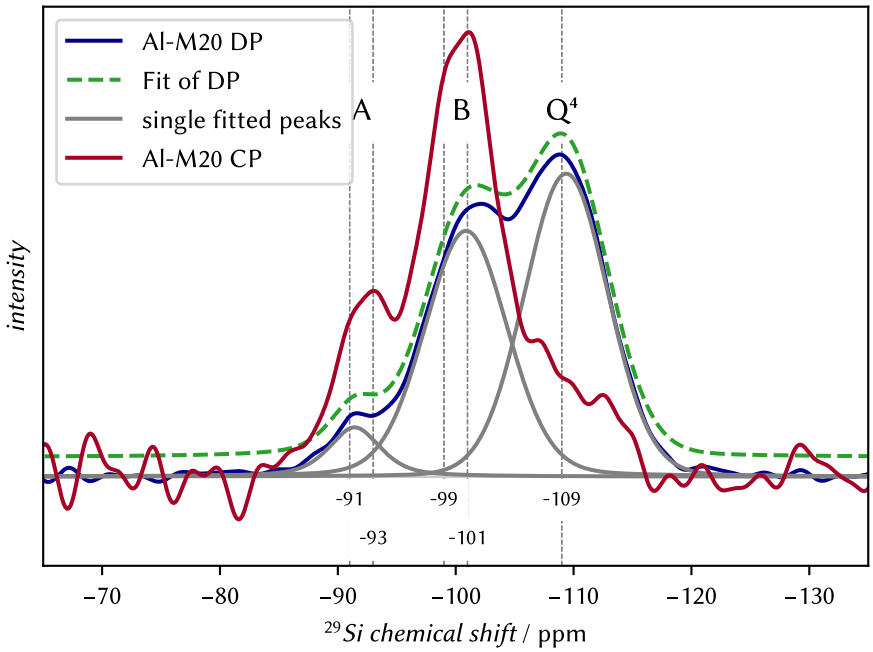

Figure B.3: CP and DP ^{29}Si spectra with deconvolution of the DP spectrum of Al-M20. The simulated spectrum is offset for visual clarity.

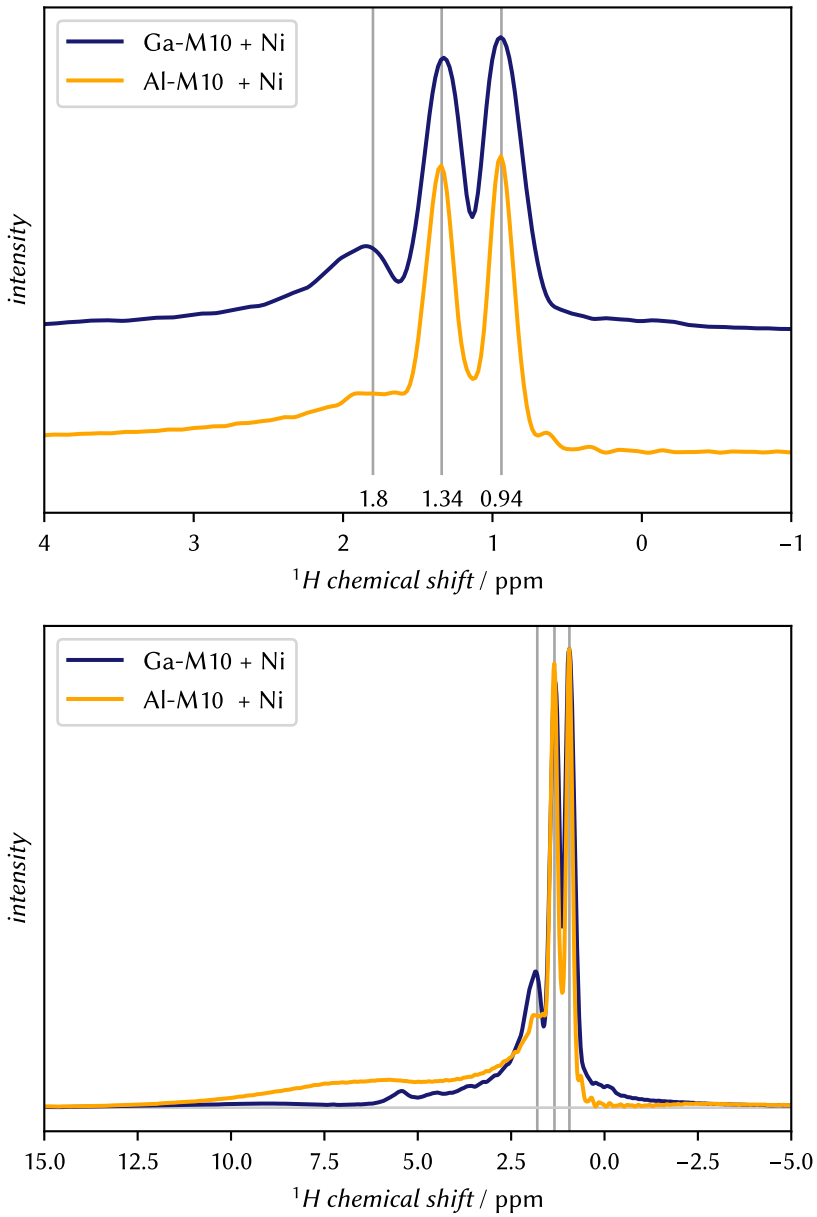

Figure B.4: Exemplary ^{1}H spectra of Ni impregnated supports recorded with a delay of 1 s between two acquisitions, zoomed to the diamagnetic signals. The spectra are normalized to their maximum. The signals at 0.94 and 1.34 ppm match the signals of pentane (Lit: 0.9 and 1.3 ppm [248]) while the peak at 1.8 ppm fits to silanols.

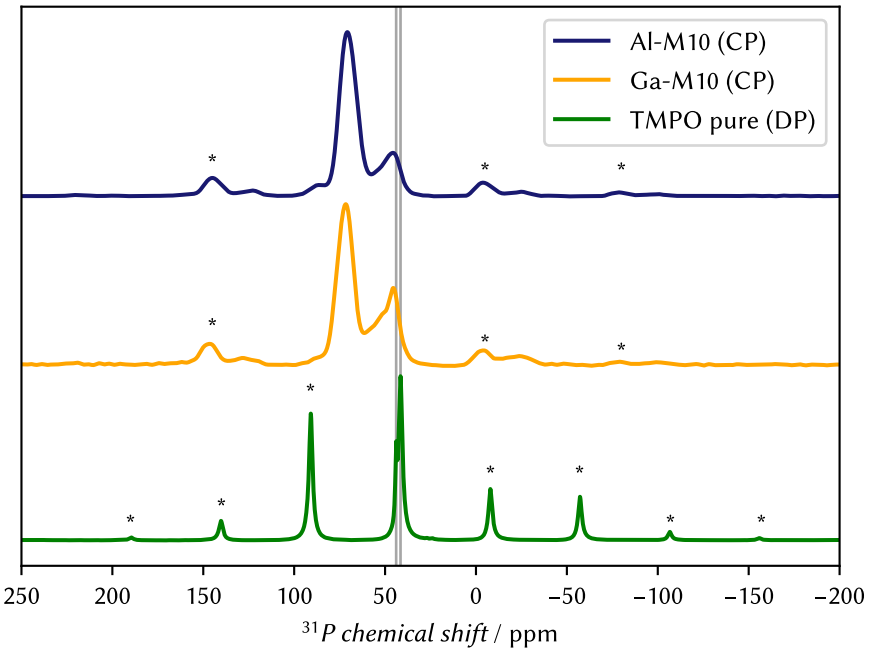

Figure B.5: Full ^{31}P spectra of TMPO impregnated samples, acquired via CP (MAS = 12 kHz) to show the CSA pattern that results from crystalline TMPO. A DP spectrum of pure TMPO at MAS = 8 kHz is shown in the bottom trace for comparison. The two lines are at 43.9 and 41.5 ppm, at the two isotropic signals of pure TMPO. The rotational sidebands are labeled with an asterisk (*) and belong to the signal at 41.5 ppm.

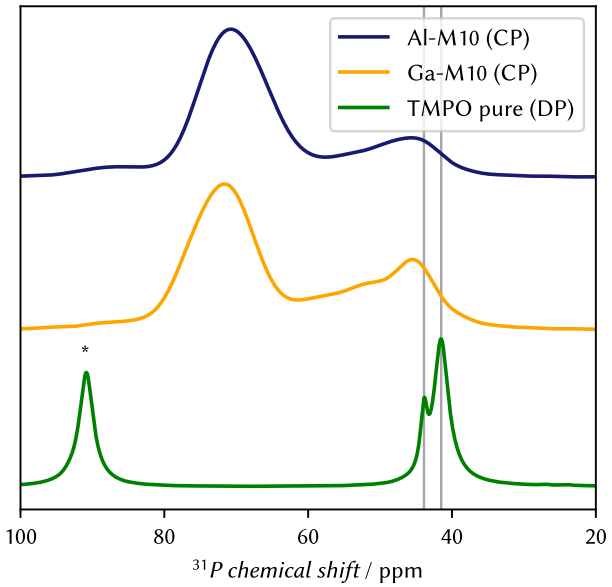

Figure B.6: Zoomed ^{31}P spectra of TMPO impregnated samples, acquired via CP to show the isotropic signals of the CSA pattern. Pure TMPO is shown in the bottom trace for comparison. The two lines are at 43.9 and 41.5 ppm, the two isotropic signals of pure TMPO. The rotational sideband (*) belongs to the signal at 41.5 ppm.

Table B.1: CSA parameters according to the HAEBERLEN convention of pure TMPO and impregnated Ga- and Al-M10 samples using **method 2**. The parameters and the linewidths (lw) were extracted using the program ssNake.

	δ_{iso} / ppm	δ_{aniso} / ppm	η	lw(Lorentz) / ppm	lw(Gauß) / ppm
ref. [199]	39.4	−170.9	0.44	–	–
pure TMPO	41.5	−125.2	0	2.5	0.0
	43.9	0.0	0	1.1	0.3
Al-M10 + TMPO	47.8	−89.7	0	2.5	13.0
	70.4	71.2	1	1.8	10.0
Ga-M10 + TMPO	52.9	−100.6	1.00	0.0	15.4
	71.9	81.8	1.00	2.0	9.5
	45.3	43.5	0.00	0.9	10.0

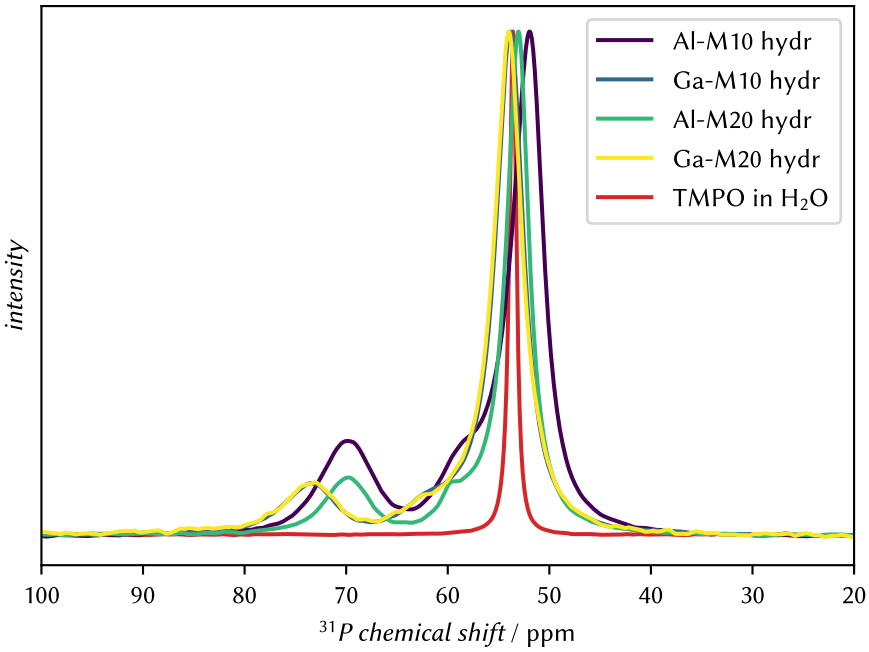

Figure B.7: ^{31}P spectra of hydrated samples after TMPO impregnation and signal of water dissolved TMPO. The latter has approximately the same concentration as is impregnated onto the supports (0.8 mmol g^{-1}). The TMPO/H_2O sample was prepared by Lasse Serger for his BSc thesis.

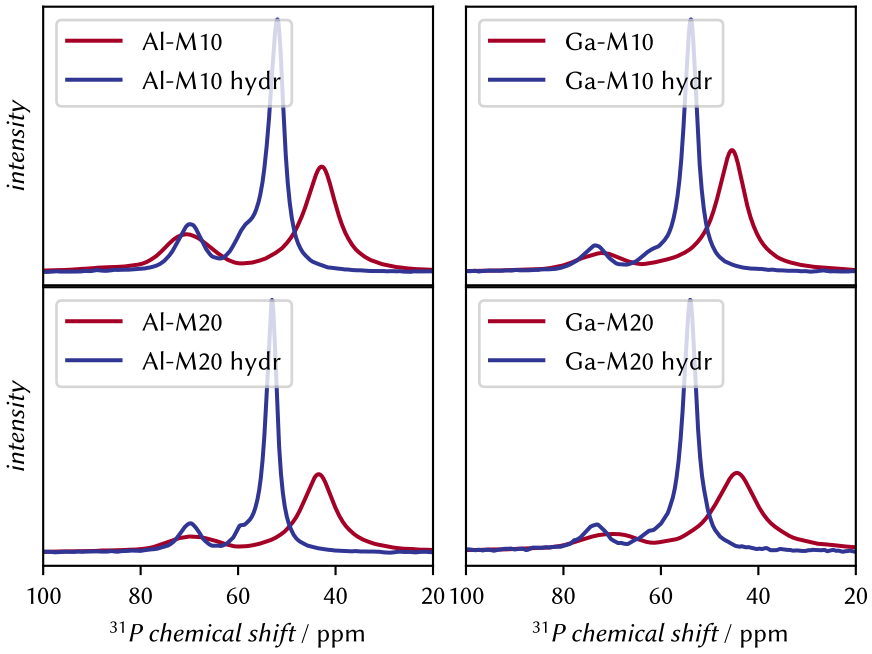

Figure B.8: ^{31}P spectra of samples after solvent-free TMPO impregnation in direct comparison with the hydrated samples.

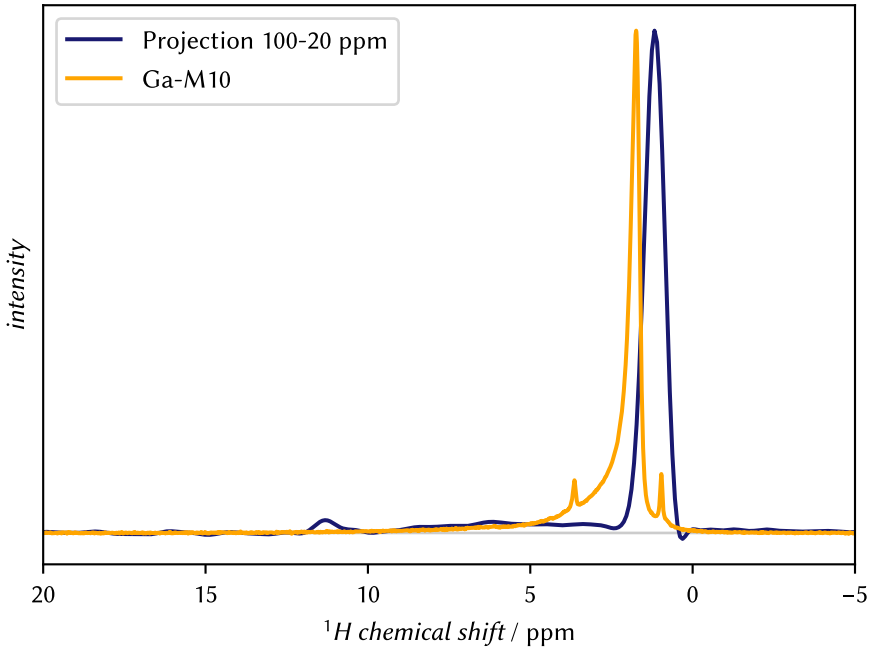

Figure B.9: Experimental 1D-DP proton spectrum (orange) and averaged spectrum along the ^{31}P dimension of the HETCOR spectrum of the same sample of Ga-M10 (**method 1**, blue). The spectra are normalized to their maximum.

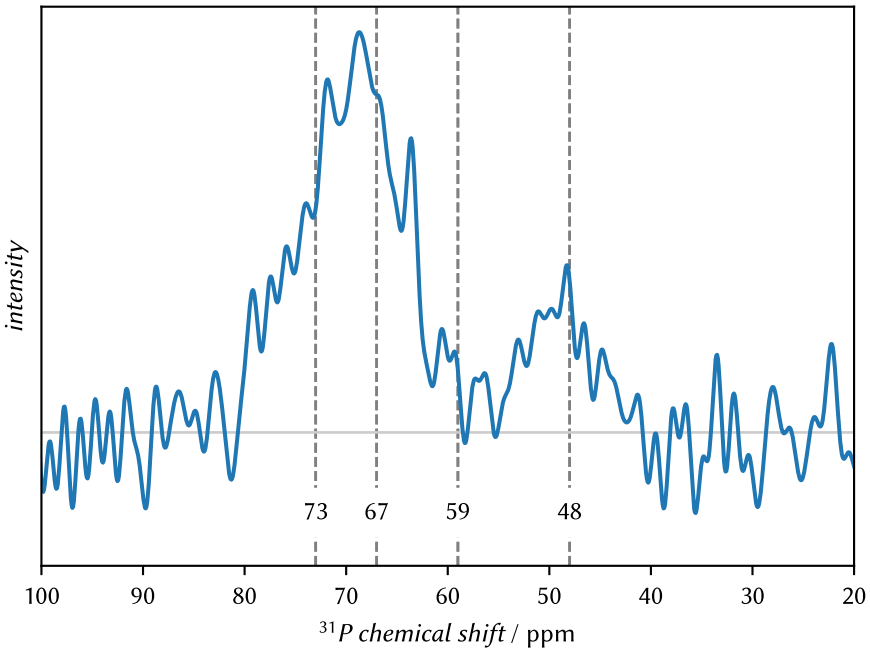

Figure B.10: Extracted slice from HETCOR spectrum of Ga-M10 (**method 1**), the signal was averaged between 10 to 12.5 ppm in the proton dimension. The vertical lines are drawn at the position of the ^{31}P chemical shifts of the deconvolved spectrum.

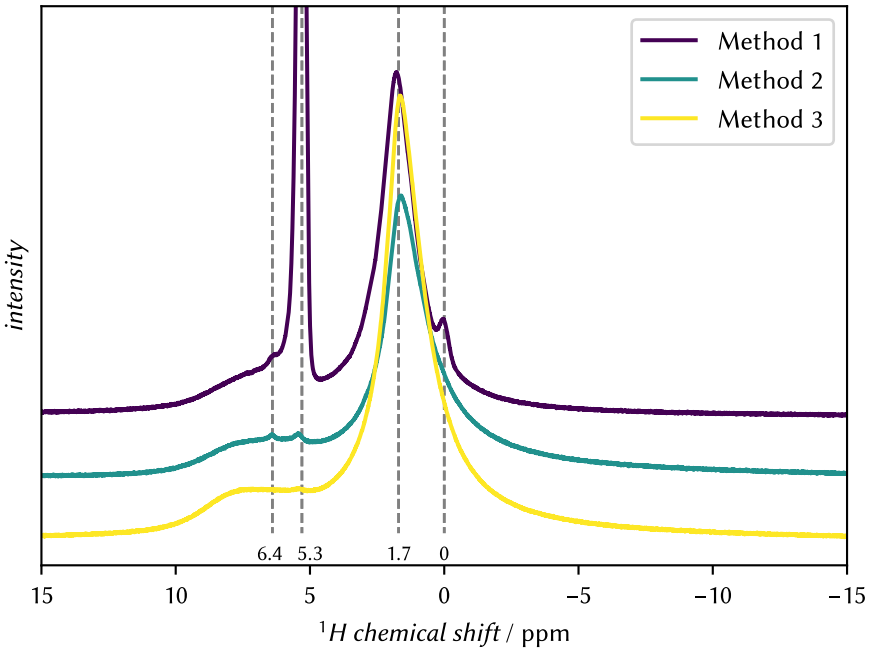

Figure B.11: ^{1}H spectra of doubly impregnated support Ga-M10. The solvent CH_2Cl_2 was removed in three different ways which are described in Section 11.6.

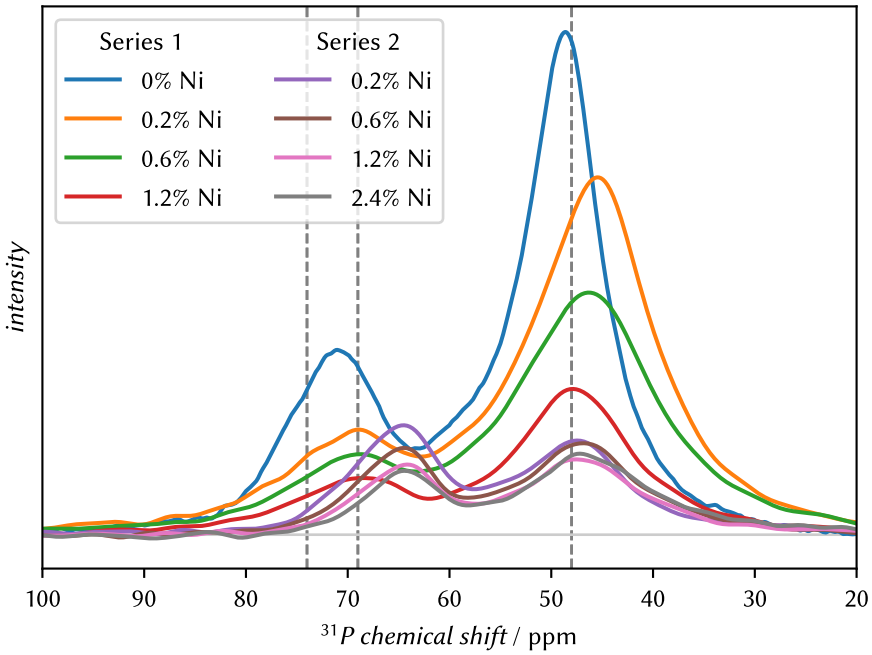

Figure B.12: ^{31}P spectra to compare the two series of Ni and TMPO impregnated supports. Both series are consistent in themselves, but the second series is significantly shifted upfield in the *B1* and *L* signal for unknown reason.

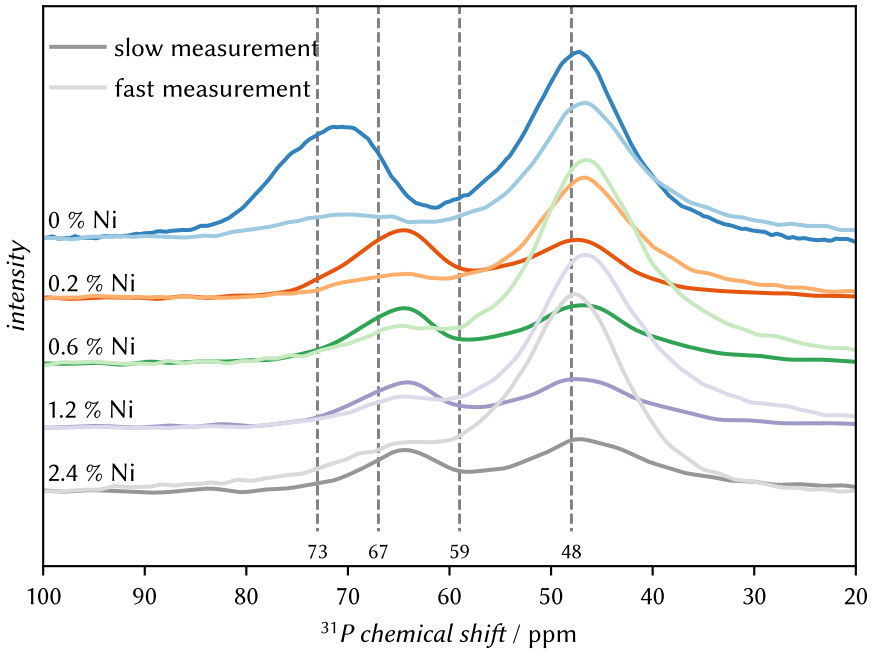

Figure B.13: Stacked plots of slow and fast measurements of Ni and TMPO impregnated samples. The spectra (except of 0 % Ni) are from the second impregnation series. Their lowfield signal (*B1* + *L*) is significantly highfield shifted in comparison to the first series, the reason for this is unclear.

C

DEUTERATION OF SUPPORTS

Support materials were deuterated in order to investigate the surface acid sites in more detail. Upon H/D exchange in mild conditions, only labile protons were exchanged by deuterium. Depending on their environment, ^{2}H is expected to be observed as a PAKE pattern that reports on its environment.
Upon ^{2}H investigations, this was not the case. It was possible to obtain spectra but instead of a PAKE pattern, a GAUSSian distribution of the spinning-sideband intensities was observed.

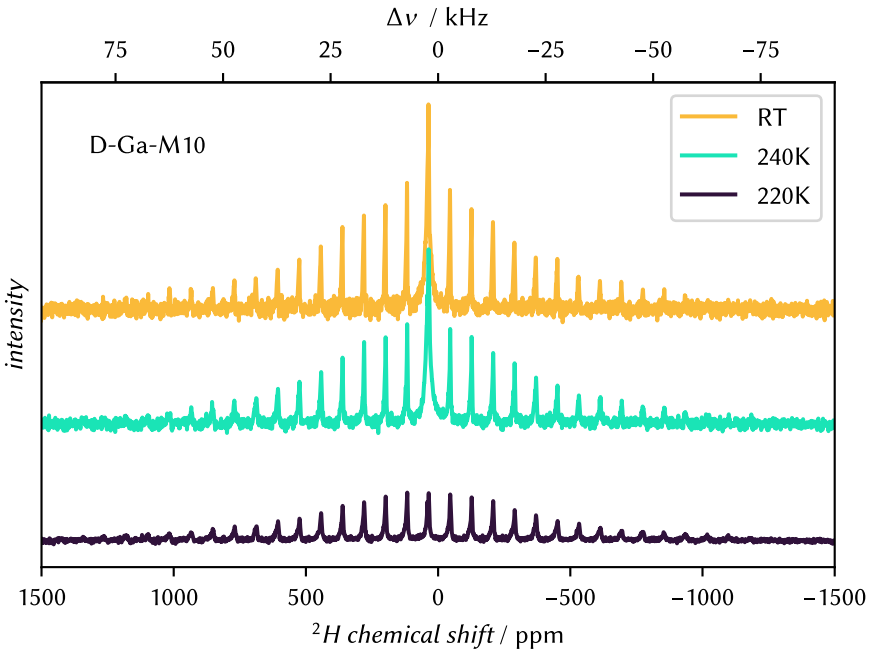

Figure C.1: Temperature dependent ^{2}H-NMR measurements of Ga-M10.

This indicates a dynamical behavior that itself has a certain distribution, overall causing the GAUSSian distribution. To this end, the reason for that is the amorphous structure of MCM-41 and that the position of acid sites is non-crystalline.

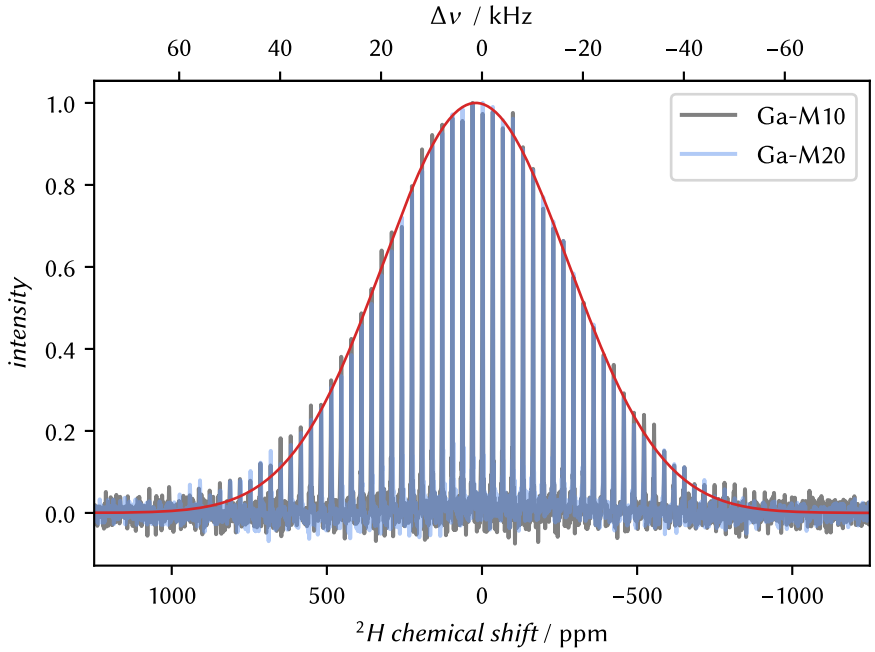

Figure C.2: ²H-NMR spectra of Ga-M10 and Ga-M20 with overlaid Gauss curve that that visualizes the Gaussian lineshape of the signal.

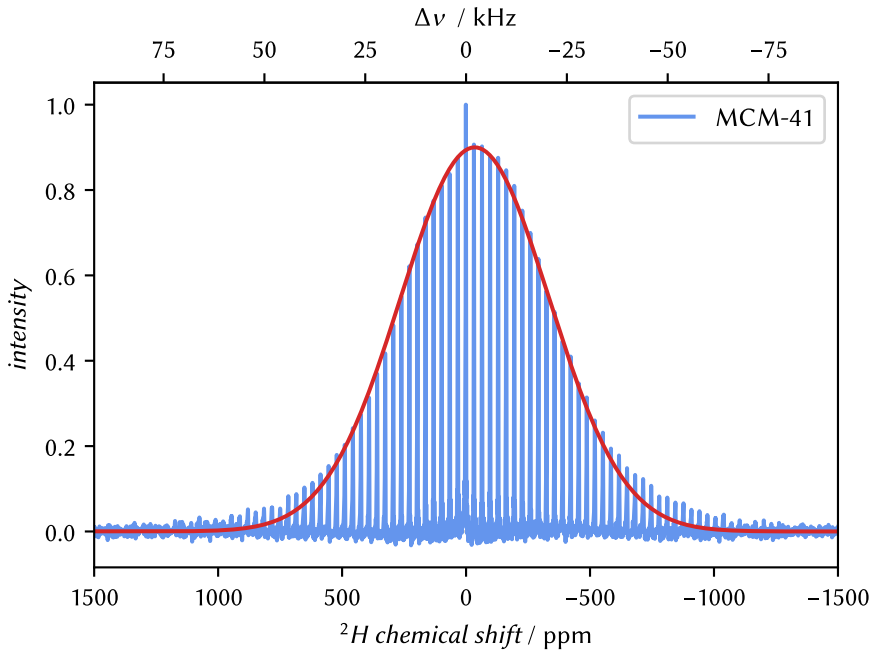

Figure C.3: ²H-NMR spectra of MCM-41 with overlaid Gauss curve that visualizes the Gaussian lineshape of the signal.

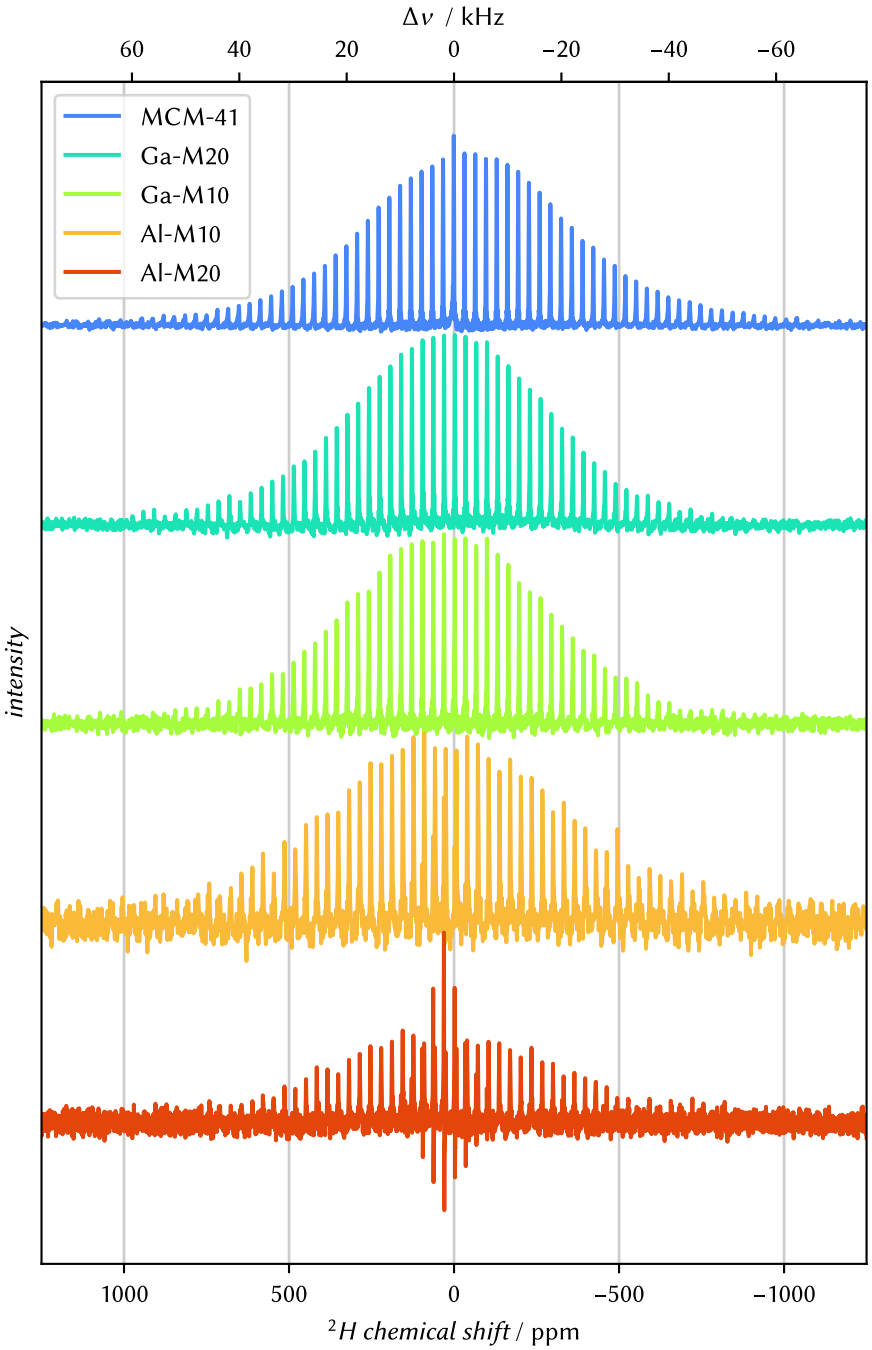

Figure C.4: ²H-NMR spectra of all deuterated supports.

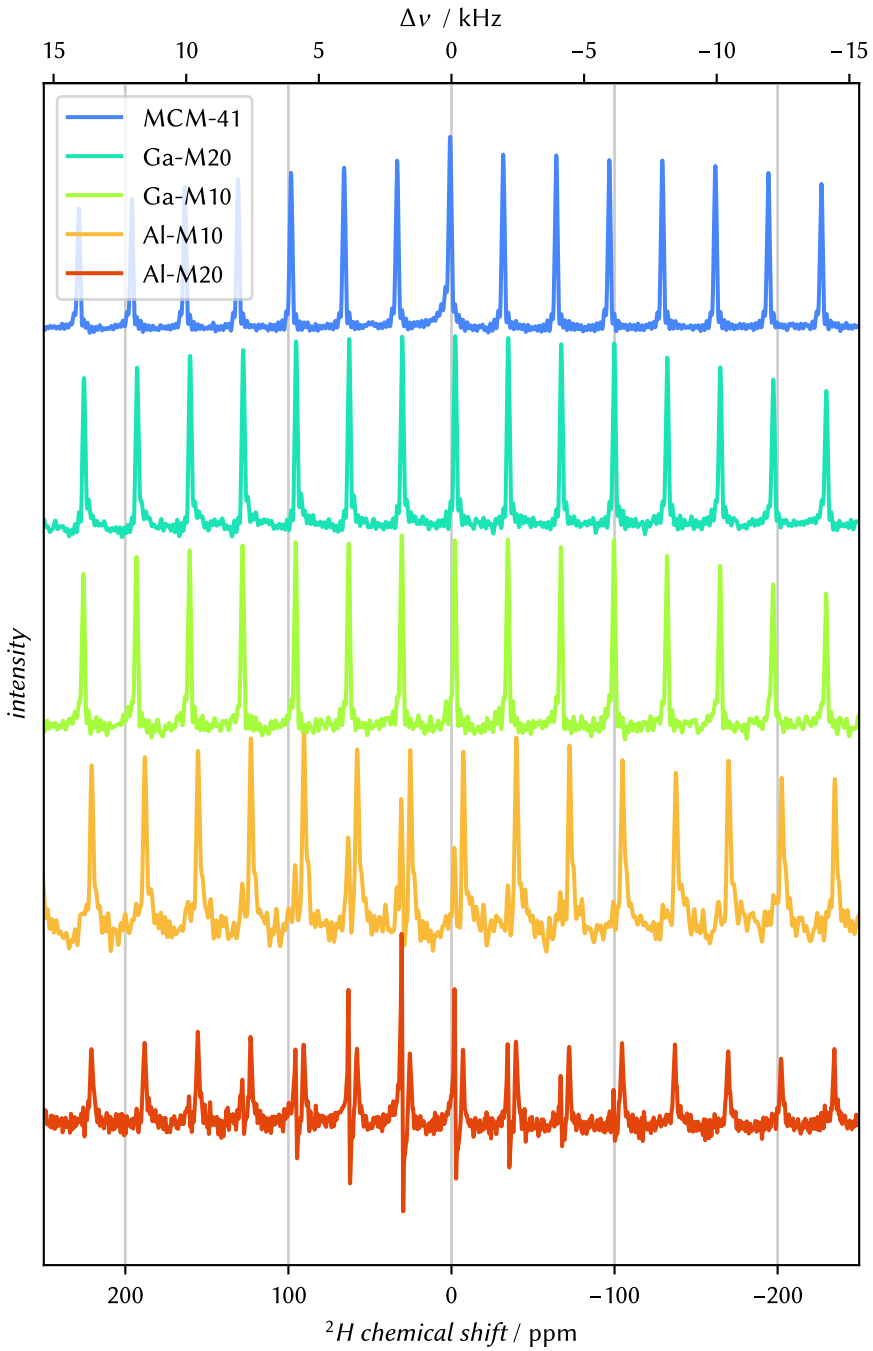

Figure C.5: ²H-NMR spectra of all deuterated supports, detailed view on the central part of the spectrum. Note the different x-axis.

D

EXTERNAL REFERENCING IN SSNMR

Contrary to liquid state (or high resolution) NMR, where the spectrum is either referenced using a designated reference compound like TMS or – less favored but often done – directly on the solvent, ssNMR is usually referenced externally with a primary or secondary standard substance. External referencing is a substitution method in which the sample of interest is exchanged by the reference sample. This procedure requires the spectrometer's magnetic field $\boldsymbol{B}_0$ to remain stable at least during the measurement of the sample and the reference. Furthermore, for an accurate comparison no changes must be applied to the hardware, i.e. no shimming and no lock being active. If the sample possesses BMS, i.e. different solvents or a concentrated or pure sample, correction needs to be performed during the referencing procedure. [265] However, this is not the case, if the sample is spun at the magic angle. [266]

Table D.1: Reference substances and chemical shifts according to the TMS scale with references for common nuclei.

Nucleus	Substance	Chemical shift /ppm	Reference
^{27}Al	$Al(H_2O)_3$	0.0	[265]
^{29}Si	Q_8M_8 [1]	11.6 & −109.0	[267, 268]
^{13}C	adamantane	37.77	[265]
^{19}F	CF_3COONH_4	−72.00	[269]
	$CFCl_3$	0.00	[265]
^{31}P	$(NH_4)_2HPO_4$	1.33	[270]
	$Na_4P_2O_7$	−1.8	

Since the classical standard substances in liquid-state NMR are liquid (TMS) or need to be dissolved in water (DSS), often solid substances are used as secondary references. The unified reference is the TMS scale which sets the zero value with its proton signals. The scales for the other nuclei are calculated using their standardized and immutable ratios of nuclear frequencies such that the scales reference to the same $\boldsymbol{B}_0$. [265, 271] One example reference is adamantane ($C_{10}H_{16}$), whose ^{13}C lowfield signal has a chemical shift of 37.77 ppm at 25 °C in the TMS scale. [265, 272] In primary references, the nucleus of interest

1 Also well suited to calibrate the Hartmann-Hahn matching.

has a chemical shift of 0 ppm, which is equivalent to the bare nucleus. Secondary standards have a chemical shift on which the spectrum is referenced. It is to note, that the chemical shift of some secondary standards (i.e. in ref [273]) deviates from the TMS-scale. Therefore, the reference system must be provided in the experimental parameters of the documentation.

E

RECIPE

Listing E.1: NMRAspecds recipe used to plot fits of all four samples in comparison. The fits have been saved before from Dmfit.

```
format:
  type: ASpecD recipe
  version: '0.3'
settings:
  default_package: nmraspecds
datasets:

# Aveiro-impregnation
- source: 194-11
  id: al-mcm10-a
  label: Al-M10 (SF, H)
- source: 190-30
  id: ga-mcm10-a
  label: Ga-M10 (SF, H)
- source: 189-15
  id: al-mcm20-a
  label: Al-M20 (SF, H)
- source: 192-12
  id: ga-mcm20-a
  label: Ga-M20 (SF, H)

tasks:
  - kind: singleplot
    type: FittingPlotter2D
    properties:
      properties:
        figure:
          dpi: 600
        axes:
          xlim: [100, 20]
          yticklabels: []
          yticks: []
      filename:
        - Al-M10-fit.pdf
        - Ga-M10-fit.pdf
        - Al-M20-fit.pdf
        - Ga-M20-fit.pdf
    result:
      - alm10
      - gam10
      - alm20
      - gam20

  - kind: compositeplot
    type: CompositePlotter
    properties:
      plotter:
        - alm10
        - alm20
        - gam10
        - gam20
      filename: aveiro-fits-400.pdf
      grid_dimensions: [2, 2]
      subplot_locations:
      - [0, 0, 1, 1]
      - [0, 1, 1, 1]
      - [1, 0, 1, 1]
      - [1, 1, 1, 1]
      parameters:
        tight_layout: True
```

This document was typeset in LaTeX using `classicthesis` developed by André Miede and Ivo Pletikosić. The fonts are Palatino by Hermann Zapf and Linux Biolinum developed by the Libertine Open Fonts Project. Figures were created using Python 3 (V. 3.10.12) with the python packages ASpecD (V. 0.12), NMRAspecds (V. 0.2) and Inkscape (V. 1.4). The English language formulation and grammar in this document have been assisted by artificial intelligence tools, specifically Claude (Anthropic) and DeepL.

One never notices what has been done;
one can only see what remains to be done.

— Marie Curie